43504

**National Library
of Canada**

**Bibliothèque nationale
du Canada**

Canadian Theses Division   Division des thèses canadiennes

Ottawa, Canada
K1A 0N4

PERMISSION TO MICROFILM — AUTORISATION DE MICROFILMER

- Please print or type — Écrire en lettres moulées ou dactylographier

Full Name of Author — Nom complet de l'auteur

OWEN EMIL NEIMAN

Date of Birth — Date de naissance	Country of Birth — Lieu de naissance
Oct 27 / 1955	CANADA

Permanent Address — Résidence fixe

10530 - 83 AVE
EDMONTON

Title of Thesis — Titre de la thèse

EFFECTS OF MAN-MADE OBSTACLES ON
PLUME DISPERSION AT A SURFACE-MINING SITE

University — Université

UNIVERSITY OF ALBERTA

Degree for which thesis was presented — Grade pour lequel cette thèse fut présentée

MASTER OF SCIENCE

Year this degree conferred — Année d'obtention de ce grade	Name of Supervisor — Nom du directeur de thèse
1979	DAVID J. WILSON

Date	Signature
Oct 15/79	Owen Neiman

NOTICE

AVIS

THE UNIVERSITY OF ALBERTA

EFFECTS OF MAN-MADE OBSTACLES ON

PLUME DISPERSION AT A

SURFACE-MINING SITE

BY

OWEN NEIMAN

A THESIS

SUBMITTED TO THE FACULTY OF GRADUATE STUDIES AND RESEARCH

IN PARTIAL FULFILMENT OF THE REQUIREMENTS FOR THE DEGREE

OF MASTER OF SCIENCE

DEPARTMENT OF MECHANICAL ENGINEERING

EDMONTON, ALBERTA

FALL, 1979

THE UNIVERSITY OF ALBERTA

FACULTY OF GRADUATE STUDIES AND RESEARCH

The undersigned certify that they have read, and
recommend to the Faculty of Graduate Studies and Research, for
acceptance, a thesis entitled "Effects of Man-Made Obstacles
on Plume Dispersion at a Surface-Mining Site"
submitted by Owen Neiman
in partial fulfilment of the requirements for the degree of
Master of Science.

....
Supervisor

....

....

Date ....July 31/79........

DEDICATION

This thesis is dedicated to the memory of

my mother, who passed away suddenly on

November 30, 1978.

ABSTRACT

A wind tunnel model was used to study stack plume dispersion
at a surface-mining site. The interaction between plumes and the
wake flows behind the stacks and large terrain obstacles (dikes)
was investigated.

Mean flow Reynolds number was about 25,000 times smaller in
the wind tunnel than in the full scale atmospheric flow, affecting
the dynamic similarity of the model. Stack wake flows were found to
model downwash effects properly despite Reynolds number mismatch, as
indicated by measured values of base pressure coefficient, $-C_{pb} \simeq 0.86$,
for cylinders at model conditions, which were close to values from
Roshko (1960) for cylinder flows at full scale Reynolds numbers.
However, model dikes were found to greatly exaggerate the size of
recirculation zones and influence of the dike wake flows on downwind
velocity and turbulence levels. This problem was corrected using a
deflector vane mounted on the model dike crests.

A combined-rise formulation was developed which predicts
both the momentum and buoyancy effect on plume rise. Momentum rise
entrainment constants, β_1, predicted from a simple model from Wilson
(unpublished) were found to yield accurate momentum rise predictions
using the combined-rise formulation. Buoyancy rise entrainment con-
stants β_2 were found to vary realistically with changing flow conditions.

The momentum flux ratio ϕ_M was found to be well correlated with
stack downwash effects, providing a means of prediction for this

phenomenon.

Dike wakes were found to increase measured ground level concentrations (GLC) from plumes, with a non-linear degree of severity with dike height. The Gaussian dispersion model was found to be adequate in predicting GLC. A correction model was proposed to account for dike effects on GLC through increased vertical plume spread σ_z in the Gaussian model.

ACKNOWLEDGEMENTS

TABLE OF CONTENTS

(ix)

LIST OF TABLES

LIST OF FIGURES

LIST OF SYMBOLS

Note: When dimensions are given, m = mass, l = length, t = time.
Equation numbers are given (in brackets) where applicable.

A	Area of top-hat plume cross-section, πr^2
C	Volume concentration of pollutant, eg. ppth
C_f	Skin friction coefficient
C_o	Volume concentration at ground level
C_{omax}	Maximum value of C_o, occurring at x_{max}
C_p	Static pressure coefficient (3-1)
C_{pb}	Base pressure coefficient for cylinders (3-2)
C_s	Volume concentration of pollutant in stack
d	Inner diameter of stack
d_o	Outer diameter of stack
F	Source buoyancy "flux", $g(\rho_a - \rho_s / \rho_a) w_s r_s^2$, $(l^4 t^{-3})$
F_M	Initial plume momentum "flux" (4-7), $(l^4 t^{-2})$
F_z	Buoyancy "flux" as a function of plume height, $(l^4 t^{-3})$
Fr	Densiometric Froude Number
g	Acceleration due to gravity, $(l t^{-2})$
GLC	Ground level concentration
h	Plume height above ground
h_s	Stack height
Δh	Plume rise, $h - h_s$
Δh_{final}	Plume rise at final rise conditions
H	Dike height (to crest)

i_u Turbulent intensity along flow direction, $\sqrt{\overline{u^2}}/U$

L_B Plume buoyancy length, F/U_s^3, (1)

L_C Reattachment length behind flow obstacles, (1)

L_M Plume momentum length, $\sqrt{F_M}/U$, (1)

$\dot{m}$ Mass flow rate of pollutant from stack, $(m\ t^{-1})$

n Velocity power law exponent, $U \propto z^n$

P Static pressure

P_{base} Static pressure at base of cylinder

P_∞ Freestream static pressure

Q Volume flow rate from stack, $(l^3\ t^{-1})$

r Characteristic plume radius $(V/v_s)^{1/2}$

r_o Initial characteristic plume radius

r_s Inner radius of stack

R Velocity ratio, w_s/U_s

Re Reynolds Number

s Plume axis direction

t Time

u Turbulent velocity component in flow (x) direction, $(l\ t^{-1})$

U Mean ambient windspeed, $(l\ t^{-1})$

U_H Mean ambient windspeed at dike crest height, $(l\ t^{-1})$

U_s Mean ambient windspeed at stack height, $(l\ t^{-1})$

U_δ Mean ambient windspeed at top of boundary layer, $(l\ t^{-1})$

v Turbulent velocity component in y direction $(l\ t^{-1})$

v_e Entrainment velocity, $(l\ t^{-1})$

v_s Characteristic plume velocity along plume axis, $(l\ t^{-1})$

V Plume volume flux divided by π [see Briggs (1975)], $(l^3 t^{-1})$

w	Turbulent velocity component in z direction, $(l\ t^{-1})$
w_r	Local stack exit velocity at a given perimeter, $(l\ t^{-1})$
w_s	Average stack exit velocity, $Q/\pi r_s^2$, $(l\ t^{-1})$
$\overline{w}$	Characteristic vertical velocity of plume [see Briggs (1975)], (
$\dot{x}$	Downwind direction (origin at stack base center)
x_d	Distance downwind of dike crest normalized by H
x_{final}	Downwind distance from stack where plume first achieves final ri
x_{max}	Downwind distance from stack where GLC is a maximum
y	Crosswind direction (origin at stack base center)
z	Vertical direction (origin at stack base center)
z_o	Roughness height of boundary layer

GREEK SYMBOLS

α	Kinetic energy correction factor (2-1)
β_1	Momentum rise entrainment constant
β_2	Buoyancy rise entrainment constant
γ	Dike disturbance parameter for plume height, h(dike)/h
Λ_x	Integral scale of turbulence, (1)
δ	Boundary layer thickness, (1)
ε	Dike disturbance parameter for lateral spread, σ_y/σ_y(dike)
η	Dike disturbance parameter for vertical spread σ_z/σ_z(dike)
η_{low}	Minimum value of η in dike correction model (6-10)
θ	Momentum thickness of boundary layer <u>or</u> angular position on cylir
ν	Kinematic viscosity, $(l^2 t^{-1})$
ρ	Mass density, $(m\,l^{-3})$

(xvii)

ρ_a Mass density of ambient atmosphere, $(m\ l^{-3})$

ρ_s Mass density of stack gas, $(m\ l^{-3})$

σ Plume spread, (1)

σ_y Lateral plume spread, (1)

σ_z Vertical plume spread, (1)

σ_z(lower)   Vertical plume spread based on fit to lower half of concentration profile, (1)

ϕ_B Buoyancy "flux" modelling parameter, $L_B/4x$

ϕ_M Momentum "flux" parameter (4-16)

χ Mass concentration, $(m\ l^{-3})$

χ_o Mass concentration at ground level, $(m\ l^{-3})$

χ_s Mass concentration of pollutant in stack gas, $(m\ l^{-3})$

ψ Concentration parameter $(\pi\sigma_y\sigma_z C_o)/(QC_s)$, $(t\ l^{-1})$

CHAPTER I

INTRODUCTION

Plume dispersion from tall industrial stacks has been studied
in detail in recent years, largely due to the increasing stringency
of pollution control legislation and the growing concern for all
industrial projects to be accountable for their impact on the environ-
ment. The designer of a plant must be able to predict the maximum
levels of pollutant concentrations that are likely to occur at ground
level or at other points of interest.

In this study, two special problems encountered in the pre-
diction of pollutant concentrations from stacks are investigated.
Both deal with the interaction of wakes behind man-made flow obstacles
with stack plumes. The first wake effect, common to all stacks, is
the interaction of the plume gas with the wake generated by the stack
body, acting as a flow obstacle in the atmospheric boundary layer.
This small wake flow can have a profound effect on the dynamics of the
plume motion because of its close proximity to the plume in the
critical early stages of rise. Under certain conditions, the low
pressure in the stack wake can pull the plume down from its normal
rise trajectory and cause abnormally severe pollution effects. This
phenomenon is called stack downwash and has been observed by many in-
vestigators such as Slawson (1978) and Fay, Escudier, and Hoult (1969).
Briggs (1969) gives a history of the study of stack downwash, which
dates back to the 1940's. A simple criteria from that era for avoiding

1

downwash was to ensure that $R > 1.5$, where $R = w_s/U_s$ is the ratio of the stack efflux velocity to the windspeed at stack height. A more general criteria is developed in this study which uses the momentum flux ratio, $\phi_M = \alpha \rho_s w_s^2 / \rho_a U_s^2$.

It is necessary to understand how stack downwash affects plume rise before investigating the effects of other plume disturbances, because two or more plume-wake flow interactions are often occuring simultaneously, and the effects of one may obscure the other. The combined effects of different plume-disturbing factors can usually only be determined by experiment.

The second wake flow examined in this study is of specific application to the surface-mining industry, but also is of interest in determining the influence of terrain obstacles on plumes in general. On these mining sites, there often exist large tailings ponds surrounded by man-made dikes, which may become very tall (perhaps 50-100m) over extended periods of mining. A dike of this size can easily be the dominant topographical feature in the plant site area. Thus, the wake flows created by wind blowing over these dikes may significantly affect plume behaviour. Investigations of dike effects are of added interest, compared to studying plume interactions with naturally-occurring terrain obstacles, because the size and location of the dikes are subject to some control by the designer.

Dikes affect stack plumes mainly through the increased flow turbulence in their wakes. The rate at which a plume spreads is governed by the amount of turbulent mixing occurring in the flow and this is increased by ambient flow turbulence. If plumes spread more due to dike wakes, it is likely that higher ground level concentrations

will occur, and this effect would be of importance to stack design.

Dikes can also be influential in deflecting ambient streamlines in the approach flow. In this way, plumes can be shifted bodily from their normal trajectories by dike-induced large scale motions in the atmosphere, altering pollution effects. It is also possible that a stack plume, trapped in the recirculation zone immediately behind a dike, could be influenced by the increased mixing in this area.

Some simple analysis provides a hint of what sort of effects dikes would have on measured concentrations. The equation

$$\left[\frac{C_o}{C_s}\right]_{max} = \frac{2Q}{\pi e h^2 U}\left(\frac{\sigma_z}{\sigma_y}\right)$$

is an estimate from the Gaussian plume model for the maximum value of ground level concentration, C_o, normalized by the stack concentration, C_s. This depends on the emission rate Q, the windspeed U, the plume height h, and the plume spreads σ_y and σ_z. The maximum concentration depends on the ratio of σ_z to σ_y, and extra spread induced by dike disturbances should act about the same on σ_y and σ_z, causing their ratio to change only slightly. Thus, there should be little effect on the maximum gound level concentration, $C_{o_{max}}$. This will later be shown from measurements of ground level concentrations. However, the position, x_{max}, at which the maximum concentration occurs, is very sensitive to plume disturbances as will also be seen.

The present study employed physical modelling of these plume-wake flow interactions in a wind tunnel. The question, "Why a wind tunnel model?" can be answered in part by examining the disadvantages

of the major alternative methods for conducting such an investigation.

Analytical methods for solving turbulent flow problems such as this one are not practical because of the complexity of turbulent flow in general. Present computers are orders of magnitude too small to dynamically analyse an entire turbulent flow including all eddy sizes from the turbulent microstructure to large scale atmosphere motions. Simplifications can sometimes be used to produce solutions that describe the gross motions in a turbulent flow, such as assuming an entrainment velocity or eddy viscosity model, but these solutions are usually semi-empirical in nature. Furthermore, the geometric complexity of real terrain features, such as buildings on a plant site or even a dike, tends to discourage attempts to obtain analytical solutions.

Another alternative for solving the problems in the present study is direct full scale measurement. This method has the obvious advantage of realism, but also many other large disadvantages. Full scale measurements, as compared to model measurements, are generally much more expensive and difficult to perform, because of the large test areas involved. Collecting full scale data is also more time-consuming, because physical processes such as diffusion are much slower in the atmosphere than they are in most wind tunnel models, and longer sampling times are required. Also, in full scale studies, the investigator must often wait for the proper atmospheric conditions or other test configurations to be present. This is not a problem in wind tunnel studies.

In the atmosphere, it is often very difficult to test the simple uniform flow cases that are desired for comparison to analytical models.

For example, the conditions of constant wind direction with time and height or uniform neutrally stable atmospheric stability are of great interest as baseline cases in the analysis of plume dispersion. However, these rarely occur in nature for sufficiently long periods of time to allow for these conditions to be properly tested. In a wind tunnel, flow conditions can be closely controlled for as long as necessary, and it is usually the simplest cases that are the most easily modelled. This latter feature can be a disadvantage also, because sometimes it is desired to model more complex flow conditions such as positive atmospheric stability.

Wind tunnel modelling of plumes has its own unique problems, which are mostly concerned with ensuring an accurate simulation of full scale processes despite certain modelling discrepancies. At least as much time is usually spent in developing and verifying the model as is spent in obtaining the desired measurements. In this study, problems were encountered with Reynolds number effects on the stack and dike wake flows, because the tunnel was operated at much lower Reynolds number than the full scale atmospheric flow. Wake flows are generally Reynolds number dependent, and this required a careful investigation of the flow past model stacks and dikes, so that their effect on plume dispersion would be accurately simulated.

The detailed objectives of the present study were:

(a) to investigate Reynolds number effects on flow past stacks and dikes in a wind tunnel and ensure a correct model of these flows

(b) to determine how stack downwash affects plume rise, and to develop a general rise model which includes these effects

(c) to determine how dikes affect plumes through measured ground level concentrations.

CHAPTER II

THE WIND TUNNEL MODEL

Introduction

In this chapter, a description is given of the wind tunnel model and experimental technique used in this study. An important feature of the model, its inability to match mean flow Reynolds number to full scale, is also discussed.

Modelling a Buoyant Stack Plume

A hot gas emitted from a chimney has the characteristics of both a jet and a buoyant plume, interacting with a turbulent cross flow. Modelling this very complicated flow requires first the accurate simulation of the important turbulent and mean flow velocity characteristics of the atmospheric boundary layer in which the stack is immersed. Once this is done, the approach flow to the stack may be characterized by one scaling velocity, which is usually the wind speed at stack height U_s.

Many different methods exist for determining the correct model values of U_s and the stack gas initial conditions to accurately model a given full scale stack. One of the major differences among these methods is the way in which the plume buoyancy is characterized. Ludwig and Skinner (1976) and the present study employ the flux modelling method, where the flux of buoyancy force emitted from the stack, $\left[g \ (\rho_a - \rho_s) w_s \ \pi r^2 \right]$, is considered to be the relevant parameter for

describing continuous buoyant plumes. Other modellers such as Isyumov,
Jandali, and Davenport (1976) have used the densiometric Froude number,

$$Fr = \frac{U_s}{\left[g \frac{(\rho_a - \rho_s)}{\rho_a} d \right]^{1/2}}$$

to characterize plume buoyancy. The Froude number actually correctly
models buoyancy effects for a discrete parcel of stack gas.

Recent studies by Winkel (1979) have shown that the flux
modelling method accurately models plume trajectories for plumes where
both momentum and buoyancy effects are important, over a wide range
of plume density ratios ρ_s/ρ_a. In the present study, density ratios
were not varied, and the flux modelling method used is summarized
below.

The following three parameters are equated between model and
full scale (prototype):

(1) The buoyancy flux parameter,

$$\phi_B = \frac{g(\rho_a - \rho_s)d^2 w_s}{\rho_a U_s^3 x}$$

(2) The momentum flux parameter,

$$\phi_M = \frac{\alpha \rho_s w_s^2}{\rho_a U_s^2}$$

(3) The density ratio between stack gas and the atmosphere,
ρ_s/ρ_a . Simulation of full scale thermally induced den-
sity ratio was obtained using molecular weight-induced
density ratio at constant temperature.

In addition, stack-exit velocity profile shapes are modelled as closely as possible to full scale shapes, characterized by their kinetic energy correction factors,

$$\alpha = \frac{2}{r^2} \int_r \left[\frac{w_r}{w_s} \right]^3 r\,dr \qquad (2\text{-}1)$$

where α is the ratio of the mean kinetic energy flux to the kinetic energy flux found using the profile mean velocity, w_s. In (2-1), w_r is the local stack gas velocity at a given perimeter.

In the present modelling method, all model lengths scale by the same factor, which is the size reduction ratio for the model.

Combining all the above criteria, the modelling relations for windspeed U_s and stack gas average velocity w_s become:

$$\frac{U_{SP}}{U_{SM}} = \left[\frac{d_P}{d_M} \right]^{1/2} \left[\frac{\alpha_M}{\alpha_P} \right]^{1/4}$$

$$\qquad\qquad\qquad\qquad\qquad\qquad (2\text{-}2)$$

$$\frac{W_{SP}}{W_{SM}} = \left[\frac{d_P}{d_M} \right]^{1/2} \left[\frac{\alpha_M}{\alpha_P} \right]^{3/4}$$

where the subscripts "M" and "P" refer to the model and prototype values, respectively.

Present Wind Tunnel Model

The present study was conducted in the Low Speed Wind Tunnel facility shown in Figure 2-1, located in the Department of Mechanical Engineering, University of Alberta. All experiments took place in the lower test section in the configuration shown in Figure 2-2. The test

section was 2.44 m wide by 1.22 m high by 11m long.

The model plant site, shown in the lower photograph of Figure 2-3, was an 800:1 scale reduction of a typical oil sands strip mining site, with flat terrain features except for tailings pond dikes tested.

Two plume models, denoted as A and B, were tested, with stack conditions for each as described in Table 2-1. Plume model A used an open stack tube with laminar exit flow (α = 2), while model B used a stack tube with a porous plug installed near the exit, which was developed by Winkel (1979). It produced a turbulent stack flow (α =1.2 with measured turbulent intensities of about i_u = 0.2. Compared to full scale stack flows, which are generally turbulent with flat velocity profiles (α = 1.03), plume model B was a more accurate model.

Reynolds Number Mismatch

In plume modelling with (2-2), it is not implied that Reynolds number, Re_d = Ud/ν , is kept constant between model and prototype; in fact, large mismatches in Reynolds number often occur. These are inherently present due to the size reduction of the model, but will be even greater if velocities in the model are lower than full scale velocities. For example, for plume model B,

$$\frac{Re_{dP}}{Re_{dM}} = \frac{U_P}{U_M} \cdot \frac{d_P}{d_M} \cdot \frac{\nu_M}{\nu_P}$$

$$= (29.80)(800)(1)$$

$$= 2.38 \times 10^4$$

so that the model Reynolds number was more than 20,000 times smaller than

TABLE 2-1: STACK CONDITIONS FOR MODEL AND FULL SCALE PLUMES

Parameter	Model A	Model B	Full Scale Equivalent		
				A*	B*
Stack Height, h_s	22.86 cm	22.86 cm	183m		
Inside Diameter, d	0.99 cm	0.99 cm	7.92 m		
Stack Gas Density Ratio, ρ_s/ρ_a	0.554	0.554	0.554		
Kinetic Energy Factor, α	2.0	1.27	1.03		
Stack Gas Condition	laminar	turbulent	turbulent		
Wind Speeds at Stack Height, U_s (m/s)	0.5 / 1.0	0.45 / 0.90		16.7 / 33.4	13.4 / 26.8
Stack Exit Velocity, w_s (m/s)	1.006	0.8604		46.8	28.5

* Full scale equivalent from (2-2) for models A and B.

the full scale equivalent. For plume model A, the ratio of Reynolds number was 2.67×10^4.

In physical modelling of fluid flows, a mismatch in Reynolds number means that the model flow will not be dynamically similar to the prototype. This would certainly apply to the present study considering the large (fourth order) mismatches calculated above. However, the modeller can take steps to ensure that an accurate simulation is obtained in spite of Reynolds number mismatch. For the gross dynamics of the plume motion, this was already accomplished by the choice of the distorted model velocity scales using (2-2). For flows around the plant site obstacles and terrain features which could significantly affect the intended measurements in the present study, a careful investigation of Reynolds number effects was required, as given in Chapter III for stack cylinders and in Chapter V for dikes.

Modelling the Atmospheric Boundary Layer

Reynolds number mismatch also had a significant effect on the method used to simulate the atmospheric boundary layer into which plumes were emitted.

The boundary layer was artificially created by the use of a passive system, where the turbulent flow gradually developed as it flowed past a series of fixed obstructions. The system used was of the type first developed by Counihan (1969) and consisted of the following three sets of turbulence generating elements:
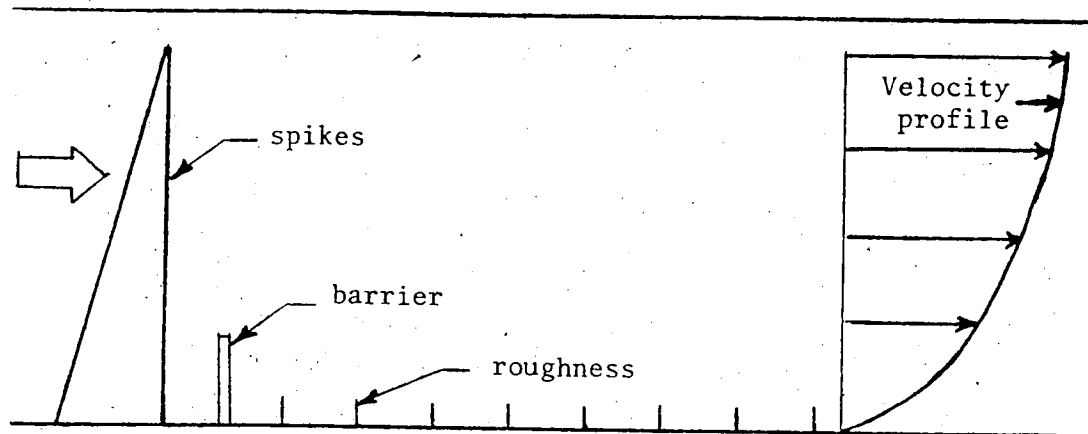
(1)   A row of seven 1 m high tapered spikes extending to
near the top of the tunnel section. These produced a
source of vertical-axis vortex motions and also a means
of adjusting lateral uniformity of velocity across the
tunnel by varying the spike spacing and angle of attack.

(2)   A low (10 cm) barrier wall mounted downstream of the
spikes and extending across the width of the tunnel.
This provided a source of horizontal-axis vortex motions
and a slowing of velocity near the floor surface to
obtain the type of power law mean velocity profile shown
above.

(3)   A 10 m length of tunnel floor section covered with
roughness elements, 3 cm and 6 cm high. These were
randomly distributed, but in a uniform density on each
roughness panel, which was 120 cm square. This roughness
provided further turbulence generation near the "ground",
and allowed the developing boundary layer to become later-
ally and longitudinally uniform.

Reynolds number mismatch in the model affected the design of the turbulence generation system in two ways:

First, the elements were made sharp-edged. This meant that flow separation points on the elements were fixed at the edges, causing their wake flows to be very insensitive to Reynolds number. Thus, the model boundary layer could maintain its characteristics over the range of model windspeeds tested.

Secondly, the elements were built very large (24 and 48 m high in 800:1 scale) in comparison to the equivalent full scale terrain roughness of a forest. This exaggerated flow disturbance was needed because the boundary layer was to be created with similar turbulent intensity as in full scale, but at four orders of magnitude less Reynolds number. The size comparison can be seen in Figure 2-3 where the size of the investigator is much larger in comparison to the 800:1 plant model shown in the lower photograph, than to the spikes, barrier and roughness shown in the upper photograph.

Turbulence and Mean Velocity Measurement

Measurements of mean velocity and turbulence were taken with linearized constant temperature hot-wire and hot-film anemometers, as shown in Figure 2-4. A DISA Type 55D01 hot-wire anemometer was used in the development of the boundary layer, and a Thermo-Systems Inc. (TSI) Model 1050 hot-film anemometer was used for all other work. Single-wire probes were used to obtain mean windspeed U and turbulent intensity $i_u = \sqrt{\overline{u^2}} / U$, while x-wire probes were used to obtain velocity components in the three coordinate directions.

During the trial and error adjustments to produce the simulated

boundary layer, surface roughness elements were present along the entire 10 m length of the test section; later, the plant site model replaced the last 5 m of roughness elements, as shown in Figure 2-2.

Vertical profiles of mean and turbulent velocities were taken at the stack location, and are plotted in Figure 2-5. Also, a comparison was made by Wilson (unpublished) of characteristic boundary layer velocity parameters between the measurements and full scale data of Counihan (1975), as given in Table 2-2. The full scale condition in Table 2-2 is representative of a neutrally stable atmospheric boundary layer over wooded terrain, and the model boundary layer is seen to be a close match to this condition.

Lateral and longitudinal uniformity of the model boundary layer were also tested and found to be very good. Mean velocity was laterally uniform to ± 6% of the tunnel centerline value over about the central 80% of the tunnel width, while turbulent intensity i_u was laterally uniform to ± 10% over the central 50% of the width. Turbulence intensity was longitudinally uniform to ± 10% of the average value along a 4 m length of test section beginning near the farthest upwind point of the plant site location. This indicated that the boundary layer was already in equilibrium before reaching the test section where dispersion measurements were later carried out.

Concentration Measurement

The stack gases in the model plumes were composed of helium-air mixtures. Helium served as both the source of buoyancy and as the tracer gas to model contaminant concentrations. Conditions between the model stack and tunnel were isothermal and isobaric, therefore measured

TABLE 2-2: COMPARISON OF WIND TUNNEL BOUNDARY LAYER WITH FULL
SCALE ATMOSPHERIC DATA OF COUNIHAN (1975)
(from Wilson [unpublished])

Parameter	Wind Tunnel 800:1 Scale	Full Scale Neutral Stability with same Z_0
Roughness height, Z_0	0.4m	Fixed at 0.4m
Mean velocity power, n	0.18 (Z < 160m) 0.30 (Z > 160m)	0.20 $\pm$ 0.03
Boundary layer thickness, δ	650 - 750m	600m (approx.)
$\left[\dfrac{\overline{u^2}}{\overline{uw}}\right]^{0.5}$ @ 30m	1.94	1.9
$\left[\dfrac{\overline{v^2}}{\overline{u^2}}\right]^{0.5}$ @ 30m	0.53	0.75 $\pm$ 0.15
$\left[\dfrac{\overline{w^2}}{\overline{u^2}}\right]^{0.5}$ @ 30m	0.41	0.50 $\pm$ 0.1
$\dfrac{C_f}{2} = \dfrac{\overline{uw}}{U_\delta^2}$ @ 30m	0.00236	0.00251 $\pm$ 0.0005
$\dfrac{\sqrt{\overline{u^2}}}{U}$ @ 30m	0.17	0.20 $\pm$ 0.03
Integral Scale, Λ_x	150m @ Z = 30m 180m @ Z = 160m	130m $\pm$ 50 200m $\pm$ 50
$\dfrac{\overline{uw}}{\overline{u^2} + \overline{v^2} + \overline{w^2}}$ @ 100m	0.17	0.14* $\pm$ 0.01

* Data from Hinze (1975) p. 643, p. 729.

volume concentration ratios C/C_s could be interpreted as mass concentration ratios χ/χ_s. This is not true for full scale hot plumes.

The procedure used to measure helium concentrations, shown schematically in Figure 2-6, was to aspirate a sample from any desired point within the plume and feed it to a heated-element four arm thermal conductivity bridge of the same type used in commercial gas-chromatograph The bridge was calibrated for helium volume concentrations by taking samples from helium-air mixture streams of measured volumetric proportions, using rotameters. The response was linear at 0.45 millivolts per ppth of helium.

Another sample, called the "reference", was taken simultaneously with the plume sample from a stationary position upwind of the plant site model, to account for background levels of helium in the recirculating tunnel. The voltage output (imbalance) of the bridge instantaneously measured the net plume concentration.

Using the HP5326B voltage to frequency converter counting DVM (with external clock timer) shown in Figure 2-6, four consecutive 100-second time averaged readings of net concentration were taken at each measurement location. The lower photograph in Figure 2-7 shows the concentration detector equipment in operation, with the traversing mechanism mounted in the tunnel to move the concentration sample probe in a straight line for profile measurements.

An example of a measured vertical concentration profile downwind of the stack is given in Figure 2-8, where the upper plot shows the scatter of the 100-second samples and the lower plot shows the cumulative 400-second average readings.

Sampling Time

Considering that a plume travels downwind essentially at the mean windspeed U, the elapsed time t for it to reach a given downwind position x is about x/U. The comparison of such a time scale between model and full scale conditions gives an estimated comparison of how fast physical processes are taking place between the two conditions. Thus,

$$\frac{t_P}{t_M} = \frac{x_P}{U_P} \frac{U_M}{x_M}$$

In the present model, $(x_P/x_M) = (d_P/d_M)$ and U_P/U_M may be found from (2-2), giving

$$\frac{t_P}{t_M} = \left[\frac{\alpha_P}{\alpha_M}\right]^{1/4} \left[\frac{d_P}{d_M}\right]^{1/2} \qquad (2-3)$$

Using (2-3), the cumulative 400-second averaged readings of concentration, such as shown in Figure 2-8, are seen to correspond to estimated full scale sampling times of 2.7 hours for plume model A, and 3.0 hours for plume model B. These estimates are probably too high, if anything, because although measured full scale plume spreads increase with the amount of sampling time due to wind direction variation with time, measured wind tunnel plume spreads, which are not subject to changes in weather, tend to become independent of sampling time after a certain period of sampling, and (2-3) is no longer applicable.
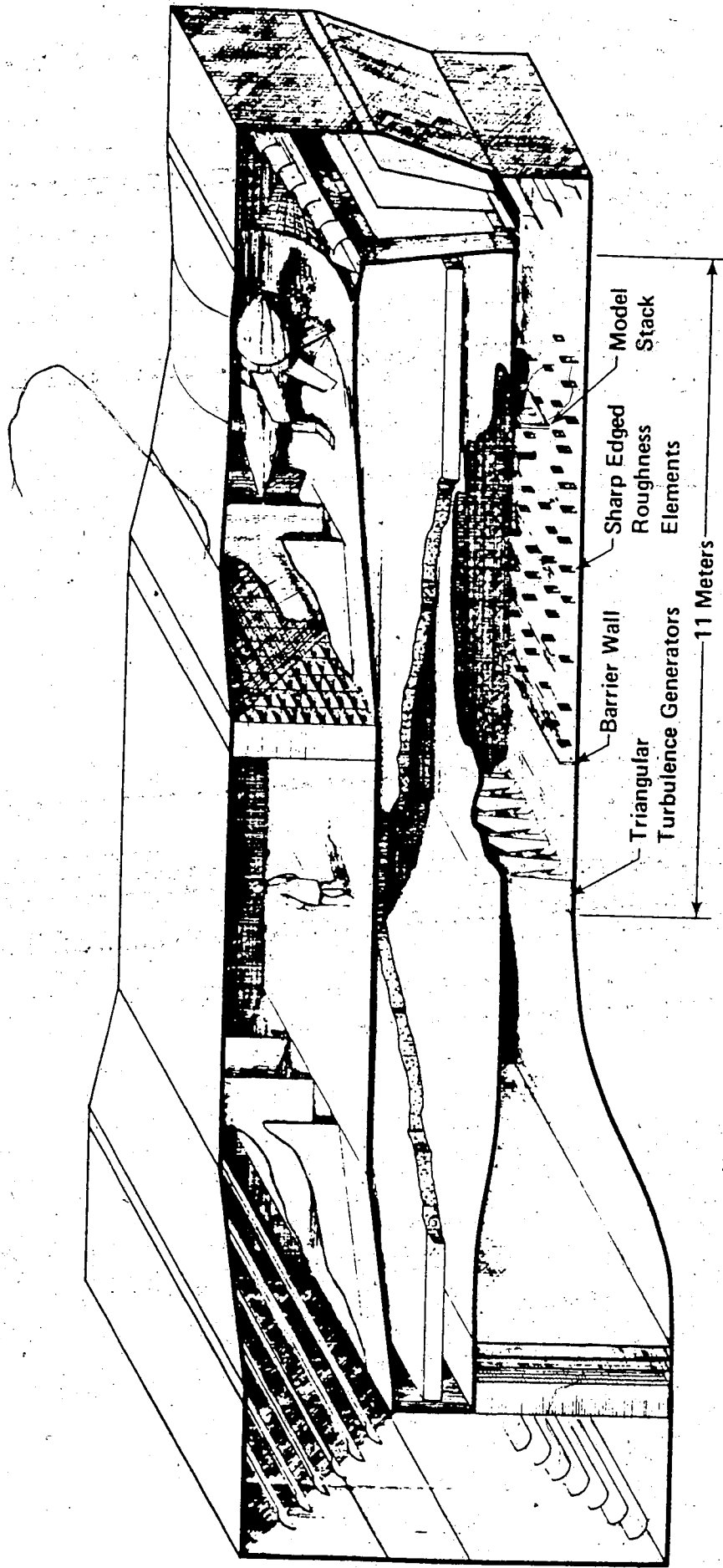
FIGURE 2-1: LOW SPEED WIND TUNNEL FACILITY AT THE
UNIVERSITY OF ALBERTA

Model Stack

Sharp Edged
Roughness
Elements

Barrier Wall

Triangular
Turbulence Generators

11 Meters
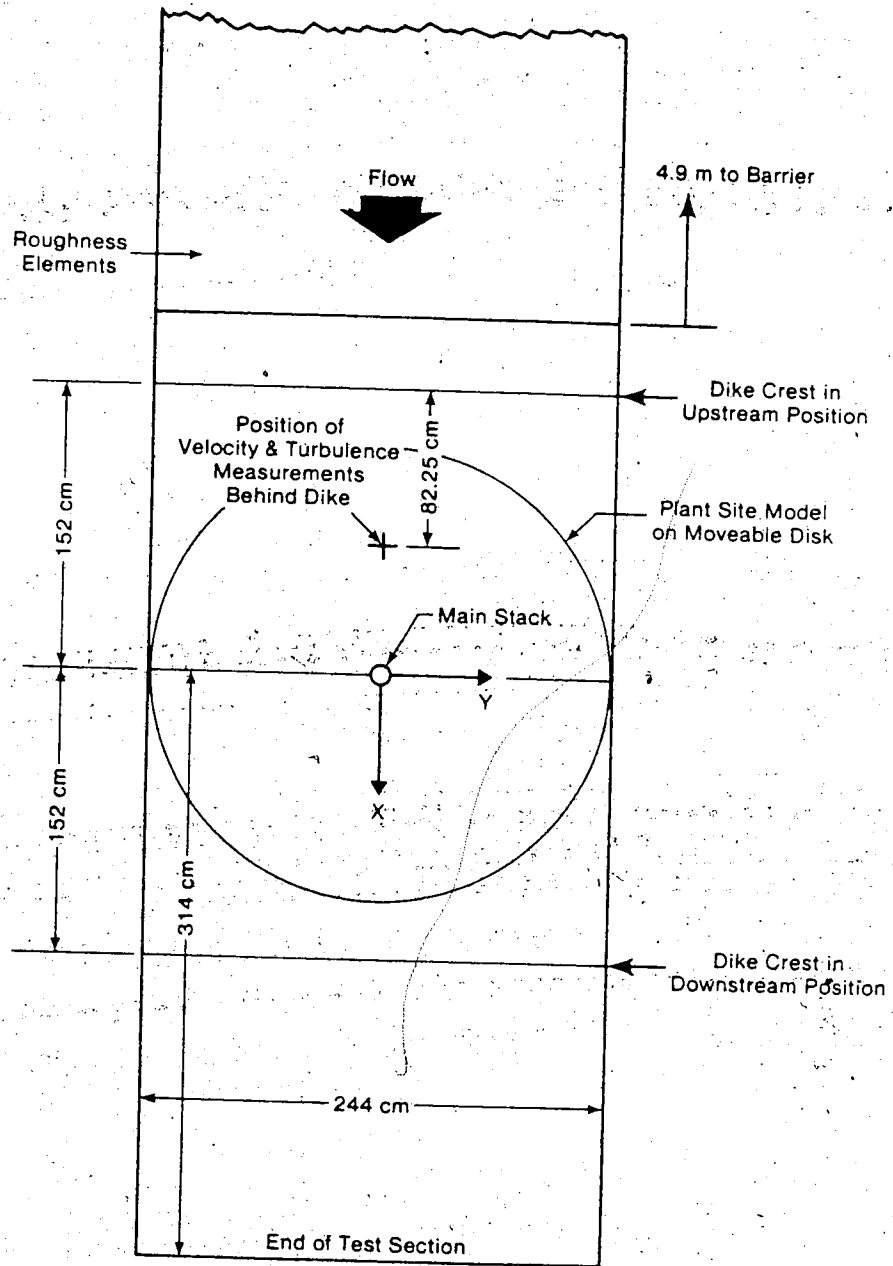
FIGURE 2-2: TEST SECTION LAYOUT AND DIMENSIONS
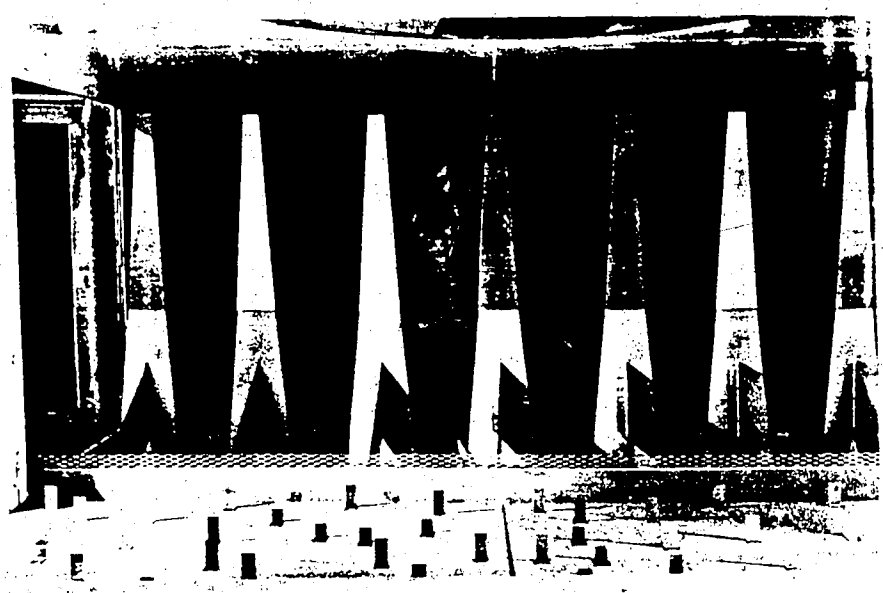
Turbulence generating spikes, barrier, and floor roughness

Adjusting the Kurz anemometer for windspeed at stack height

FIGURE 2-3: TURBULENCE GENERATION SYSTEM AND PLANT MODEL
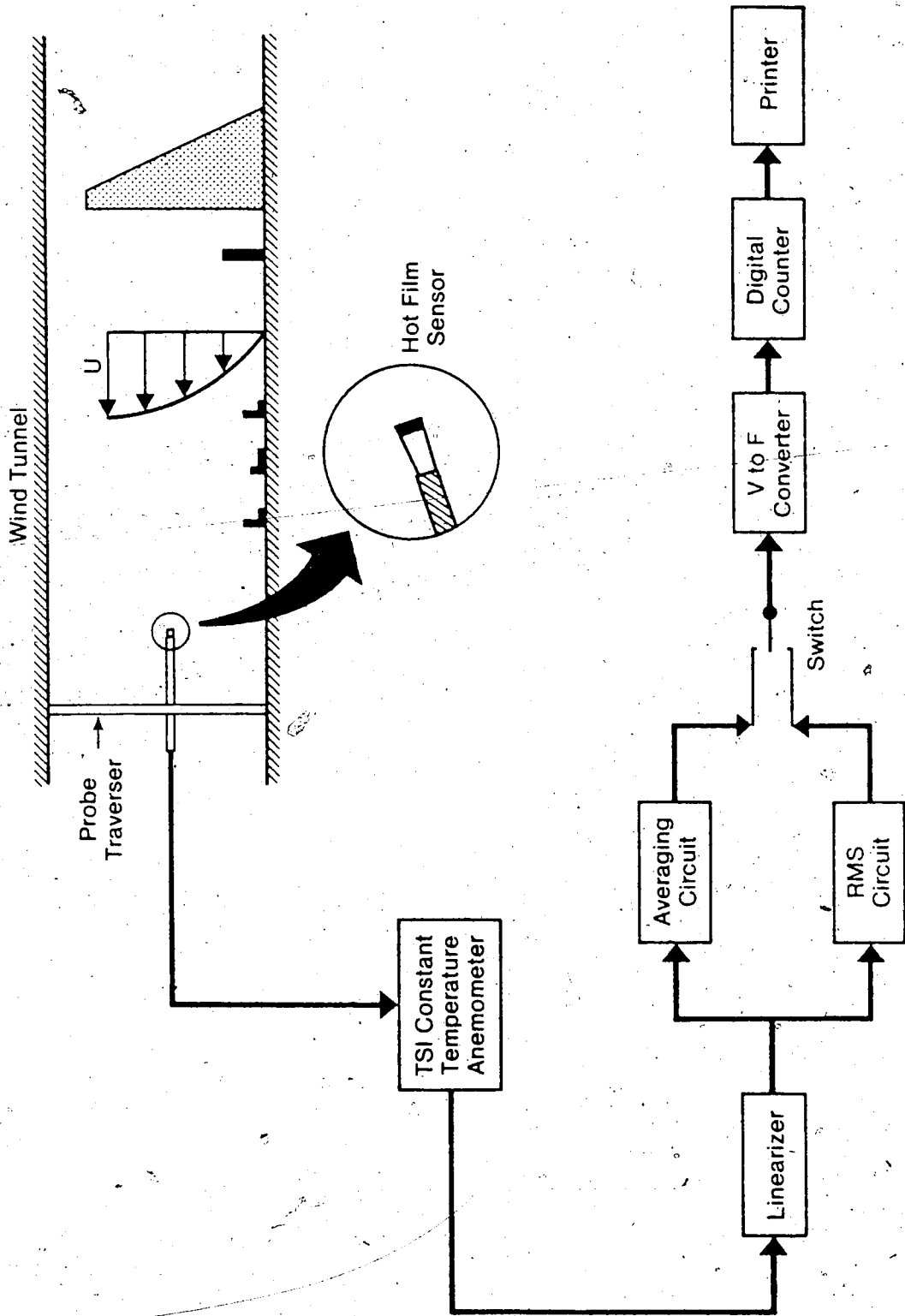
FIGURE 2-4: MEASUREMENT OF TURBULENCE AND MEAN VELOCITY

Reynolds Stress, $-\overline{u'w'}$, m^2/sec^2
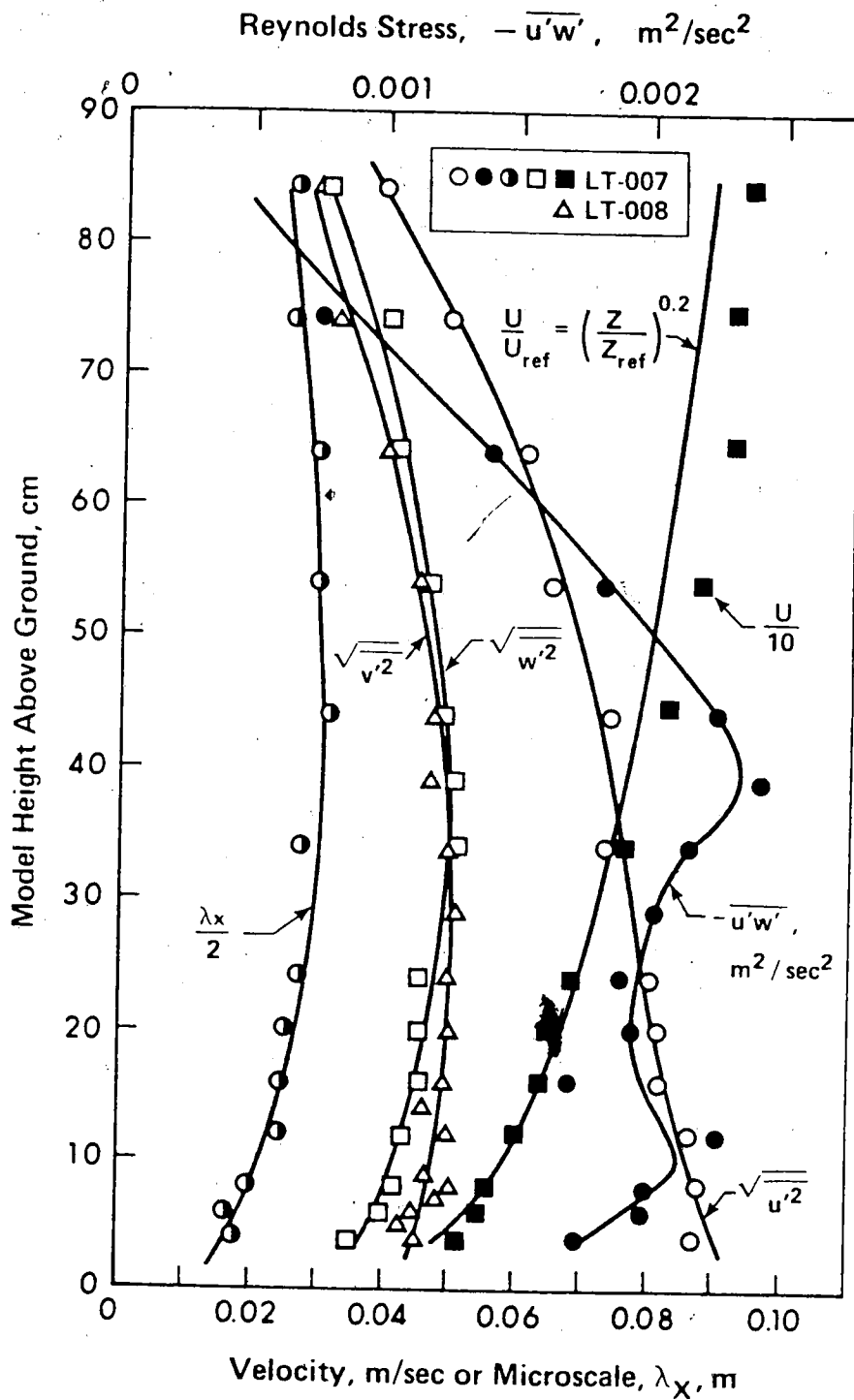
FIGURE 2-5: TURBULENT AND MEAN VELOCITY CHARACTERISTICS
OF THE SIMULATED BOUNDARY LAYER
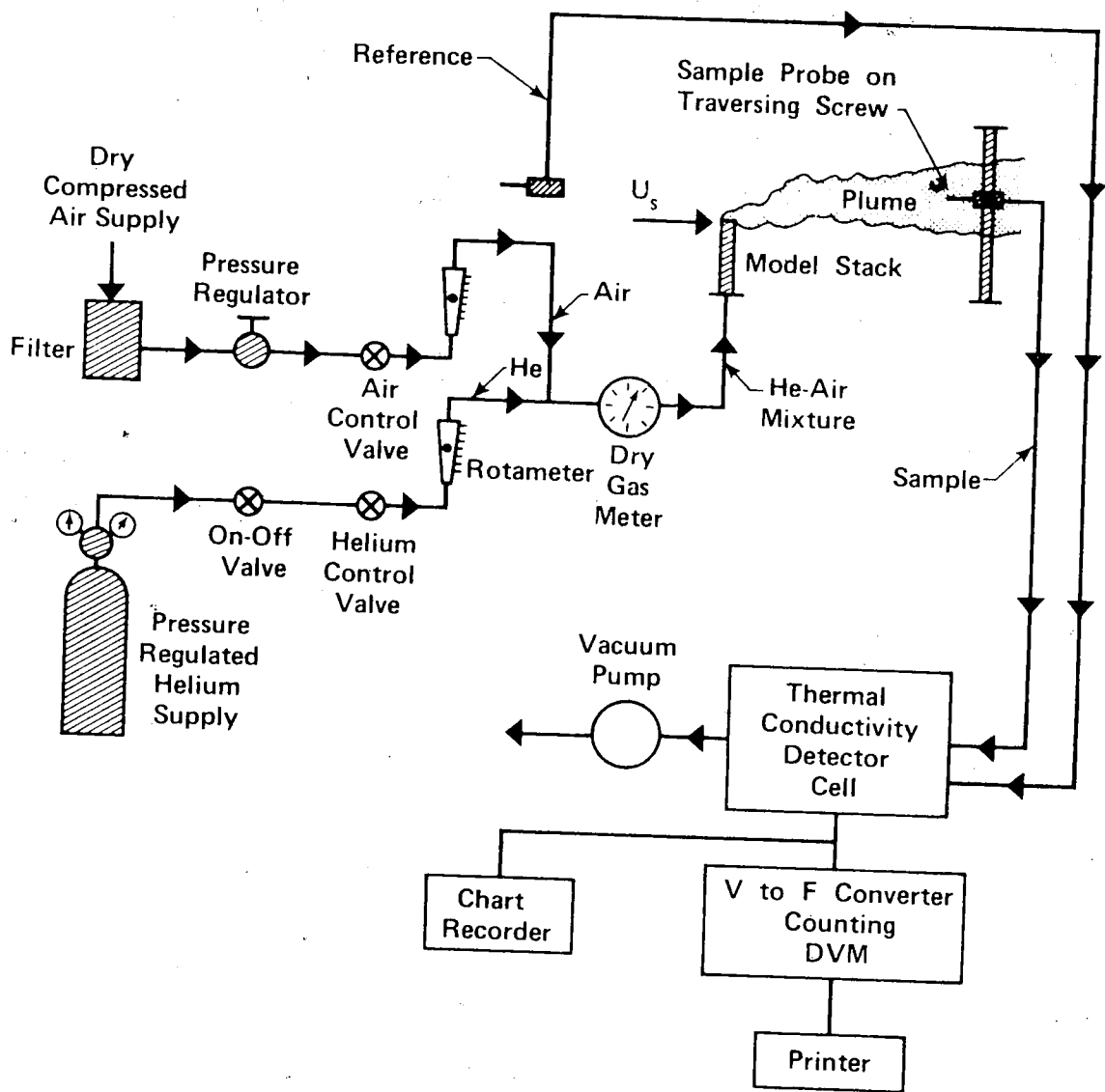
FIGURE 2-6: MEASUREMENT OF PLUME CONCENTATION IN
THE WIND TUNNEL
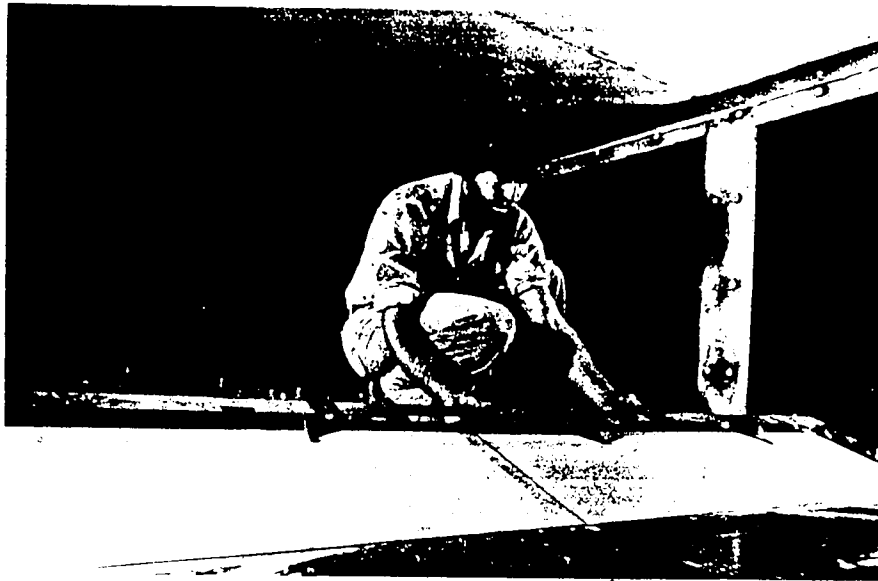
Placing the deflector vane on the dike crest

Measuring a vertical profile

FIGURE 2-7: DIKE MODEL AND EQUIPMENT SET-UP
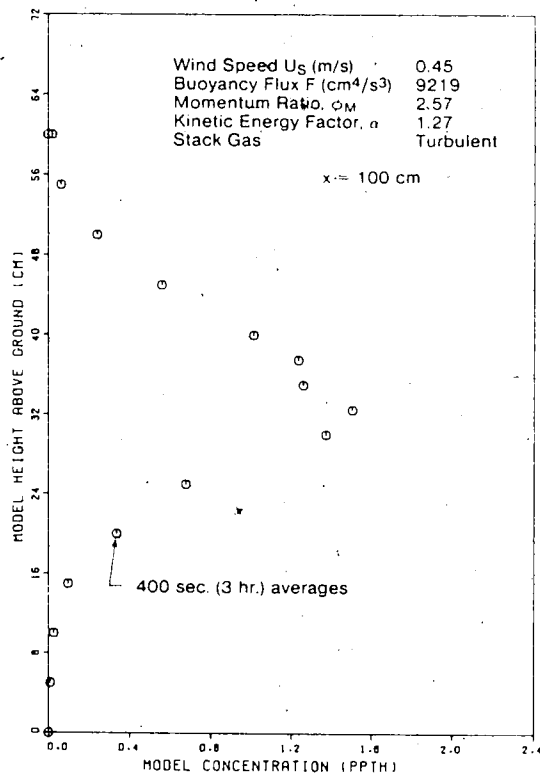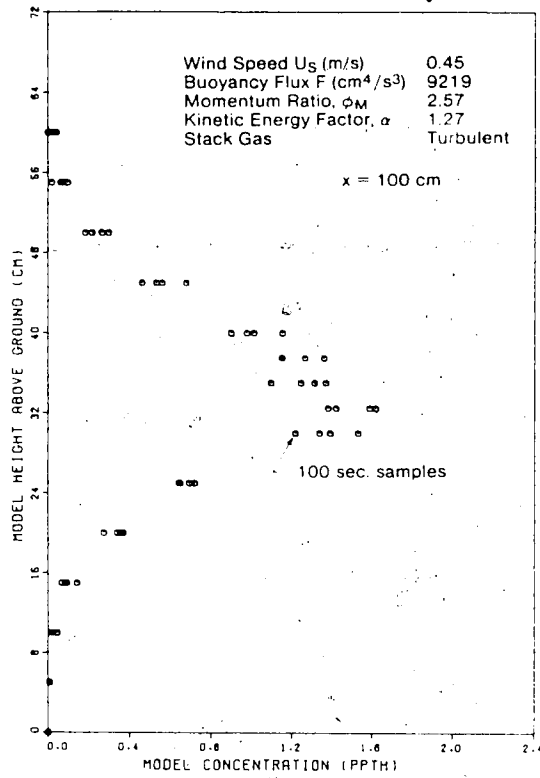
FIGURE 2-8: VERTICAL CONCENTATION PROFILE DOWNWIND OF THE
STACK (x=100 cm) FOR PLUME MODEL B

CHAPTER III

FLOW PAST CYLINDRICAL STACKS

Introduction

In this chapter, the Reynolds number sensitivity of flow around cylinders is examined, and applied to the modelling of wakes behind cylindrical stacks. Because of the mismatch in mean flow Reynolds number in the present model (see Chapter II), different flow characteristics are expected for model and full scale stack wakes. These differences may be reflected in a poor simulation of the stack wake effect on plume dynamics.

Cylinder Pressure Coefficient

The static pressure coefficient,

$$C_p = \frac{P - P_\infty}{\frac{1}{2}\rho_\infty U_\infty^2} \qquad (3\text{-}1)$$
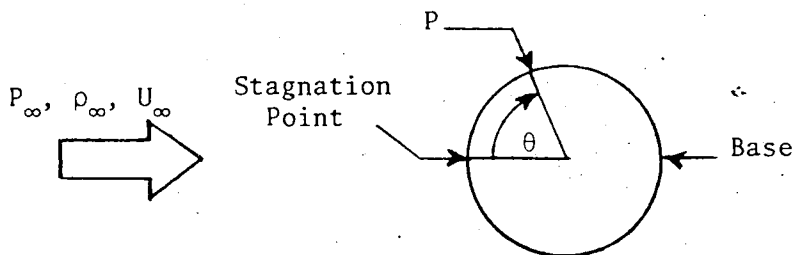
measures the normalized pressure at any point in a flow and is often used in pressure drag calculations for flow obstacles. When applied to the base ($\theta = 180°$) of a cylinder, the cylinder base pressure coefficient

C_{Pb}, is obtained, where

$$C_{Pb} = \frac{P_{base} - P_{\infty}}{\frac{1}{2}\rho_{\infty} U_{\infty}^{2}} \qquad (3-2)$$

Because the local pressure defect, $(P - P_{\infty})$, is fairly constant at all angular positions on the cylinder past the point of flow separation, C_{Pb} effectively measures the magnitude of the pressure defect for the entire initial wake region, and is a comparative wake suction parameter for model and full scale conditions. Correct modelling of stack wake effects on plume dynamics in a wind tunnel should then depend on matching C_{Pb} to full scale, although this is only a simple criteria which neglects other possibly important effects such as wake size and turbulence levels. Values of C_{Pb} are either available from previous studies or are readily measurable, adding to the usefulness of this parameter.

Infinite and Finite Cylinders

A stack is a finite cylinder, and therefore some attention should be paid to the top end effect on C_{Pb}, especially because the region of the stack wake flow near the top of the stack is in closest proximity to the plume and will exert the greatest influence on its dynamics. However, data for infinite cylinders was used exclusively in this study and assumed to apply to the top portions of stacks, thus neglecting the end effect. This choice is supported by the following arguments:

The end effect of a stack top is likely much less severe than that caused by a flat cylinder end, due to the vertical jet of stack gas acting as a cylindrical flow obstacle in continuation with the stack. This hypothesis is strongly supported by the work of Moussa,

Trischka, and Eskinazi (1977) who conducted detailed flow-field mappings of jets emitted from cylindrical pipes in a crossflow. As shown in Figure 3-1, they found that "the leading surface of a jet, acting as a barrier to the crossflow, is quantitatively very close to that of a rigid cylinder. Shed vortices are continuous with the pipe, and are characteristic of the pipe."

Although Moussa's tests involved high-velocity jets with no downwash, all stack plumes would be expected to exhibit some of the above behaviour because even severely downwashed plumes tested in the present study were found to possess initial vertical rise of at least one diameter above the stack exit.

It therefore seems likely that flow near the top of a stack is very similar to flow past an infinite cylinder and that C_{Pb} values are probably also very close. Even if absolute values of C_{Pb} are not exactly the same for infinite cylinders as for stack tops, a relative comparison between values at high full scale Reynolds numbers and values at low model Reynolds numbers in each case would likely be very similar because the flows themselves are very similar. Thus, conclusions regarding Reynolds number effects on infinite cylinders would be expected to apply to stacks also.

Cylinder Flow at Varying Reynolds Number

Variations in cylinder base pressure coefficient with Reynolds number, $Re_{d_o} = Ud_o/\nu$ are closely tied to flow transitions that take place at various values of Re_{d_o}. It is therefore helpful to outline the flow regimes that occur as Reynolds number increases from zero to full scale values for cylinders.

The first major flow regime is the subcritical regime, which exists for all Reynolds numbers up to the so-called "lower transition" point, occurring in the region $2 \times 10^5 < Re_{d_o} < 5 \times 10^5$. In the sub-critical regime, the flow separates from the cylinder while the developing boundary layer is still laminar. This happens at about $\theta = 80°$, causing a wake flow wider than the cylinder diameter.

According to the data compiled by Griffin (1977), shown in Figure 3-2 as dashed lines, values of base pressure coefficient may be taken as approximately $-C_{pb} = 0.9$ below $Re_{d_o} = 10^3$ and $-C_{pb} = 0.8$ above $Re_{d_o} = 10^3$. Data compiled by Sachs (1972) shows that $-C_{pb}$ increases to a maximum value of about $-C_{pb} = 1.2$ at the lower transition point.

In Figure 3-3, plots of pressure coefficient, C_p, against angular position, θ, are given for various flow regimes, as compiled by Roshko (1960). The subcritical regime is represented by the curve from Fage and Falkner (1931) at $Re_{d_o} = 1.1 \times 10^5$. The long flat section beyond the separation point at $\theta = 80°$ shows the nearly constant value of static pressure throughout all the rear surface area of the cylinder beneath the separated flow. Values of $-C_{pb}$ are large in the subcritical regime because the C_p curve flattens out due to separation before it has a chance to return to smaller values, as it did in the other curves in Figure 3-3.

The second major flow regime for cylinders is the supercritical regime, and extends from the lower transition point near $Re_{d_o} \approx 10^5$ to an upper transition point, which occurs within the region $10^6 < Re_{d_o} < 3.5 \times 10^6$, according to Roshko (1960). In this supercritical regime, the cylinder boundary layer undergoes a transition from laminar to turbulent flow prior to separation, allowing for a later separation

point at about $\theta = 120°$. Also, $-C_{Pb}$ drops steeply to a low value of

about $-C_{Pb} = 0.2$, as shown by Flachsbart's (1929) data in Figure 3-2.

The exact magnitude and location of this drop are sensitive to approach

flow turbulence, so that Flachsbart's curve can only be regarded as

typical of the supercritical regime.

In Figure 3-3, the data from Flachsbart (1929) at $Re_{d_o} = 6.7 \times 10^5$

represents the supercritical regime. The small flat in the curve near

$\theta = 105°$ is probably evidence of a laminar separation "bubble" [Roshko

(1960)], in which static pressure would be expected to remain constant.

Bursnall and Loftin (1951) have shown that in the supercritical regime

for cylinders, a localized laminar separation bubble occurs before the

turbulent transition, reattachment, and subsequent turbulent separation

of the flow from the cylinder. Roshko (1960) has observed that the

apparent disappearance of this bubble may be linked to the upper transi-

tion at about $Re_{d_o} = 10^6$.

The third flow regime is the transcritical regime, and exists

at Reynolds numbers above the upper transition point. In this regime,

the turbulent separation point is observed by Roshko (1960) to move

forward on the cylinder to about $\theta = 90°$. This return to an earlier

separation and larger wake flow, as in the subcritical regime, is matched

by a return in pressure coefficient values to subcritical-like values,

as seen by Roshko's data in Figures 3-2 and 3-3. Roshko (1960) also

suggested that no further transitions are likely to take place at higher

Reynolds numbers, because the point of boundary layer transition to

turbulence can now only move very gradually forward on the cylinder.

Implications of Reynolds Number Mismatch

Because typical model Reynolds numbers for the present study were in the region $3 \times 10^2 < U_s d_o / \nu < 8 \times 10^2$, while the corresponding full scale Reynolds numbers were in the region $8 \times 10^6 < U_s d_o / \nu < 2 \times 10^7$, it is apparent from Figure 3-2 that model C_{Pb} values should be very close to the full scale values at about $-C_{Pb} = 0.86$.

To further test this hypothesis, a study was conducted in the wind tunnel with a long cylinder immersed in the turbulent model boundary layer described in Chapter II. As shown in Figure 3-4, the cylinder was hollow, with the same outside diameter, $d_o = 1.275$ cm, as the model stack. However, unlike stacks, it extended over the entire test section height, to eliminate end effects. Pressure taps were drilled along the cylinder base at four different heights, as shown in Figure 3-4. Only one was left open during a specific test; the rest were sealed with tape.

To obtain C_{Pb}, it was necessary to measure the very small difference between the cylinder base pressure and the approach flow static pressure, which difference was approximately 0.005 cm of H_2O at $U = 1$ m/sec. A Validyne Model DP45 differential pressure transducer was used, with one input connected to the inside of cylinder tube, which was uniformly at the outside cylinder base pressure, and the other input connected to a static pressure tube mounted in the approach flow at the same height as the base pressure tap being used. The transducer thus directly measured the pressure defect, $P_{base} - P_\infty$.

The approach velocity, U_∞, was measured with either a pitot-static tube (> 2 m/sec) or a Kurz Model 435 hot film anemometer (0 - 2 m/sec), positioned at the same height as the pressure tap being used, so

that the local velocity with height was obtained. This local velocity was clearly the correct velocity to use, as seen in Figure 3-2, where the measured values of C_{pb} vary smoothly with Reynolds number. The smooth curve through the data gives a more accurate prediction than the suggested approximate values by Griffin (1977). Turbulence variation with height in the approach flow did not significantly affect C_{pb}.

Because of the fortuitous match in base pressure-coefficient values between cylinder flows at model and full scale Reynolds numbers, model stack wakes are expected to exert the same influence as their full scale counterparts on plume rise, despite the large Reynolds number mismatch.
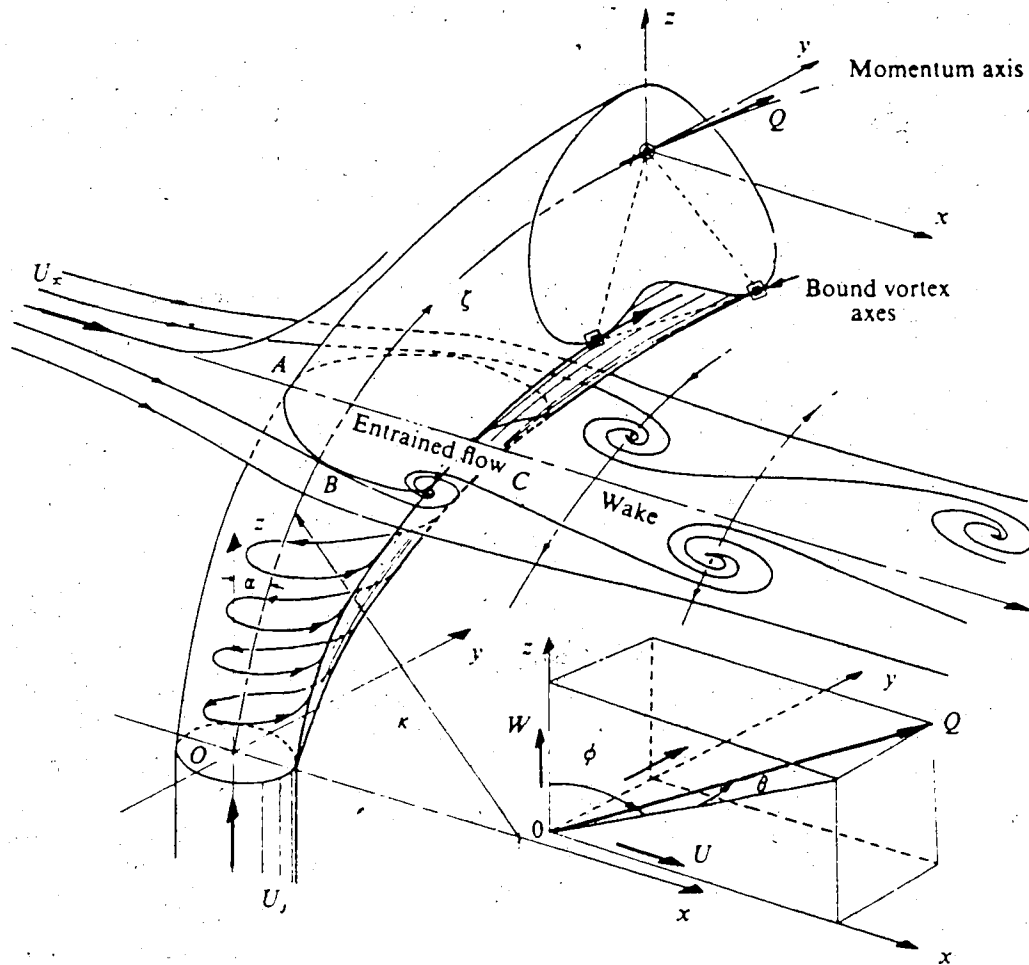
FIGURE 3-1: VORTEX SHEDDING FROM A JET [FROM MOUSSA, TRISCHKA, AND ESKINAZI (1977)]

Flachsbart (1929)

Roshko (1960)

Sachs (1972)

Griffin (1977)

$-Cp_b = \dfrac{P_\infty - P_{base}}{\frac{1}{2}\rho U^2}$

z (cm)
△ 15.2
○ 22.9
□ 53.3
▽ 98.7

$Re_{d_o} = \dfrac{U d_o}{\nu}$ Local Reynolds Number

$-Cp_b$ Base-Pressure Coefficient

1.2 1.0 0.8 0.6 0.4 0.2

10^1 10^2 10^3 10^4 10^5 10^6 10^7 10^8
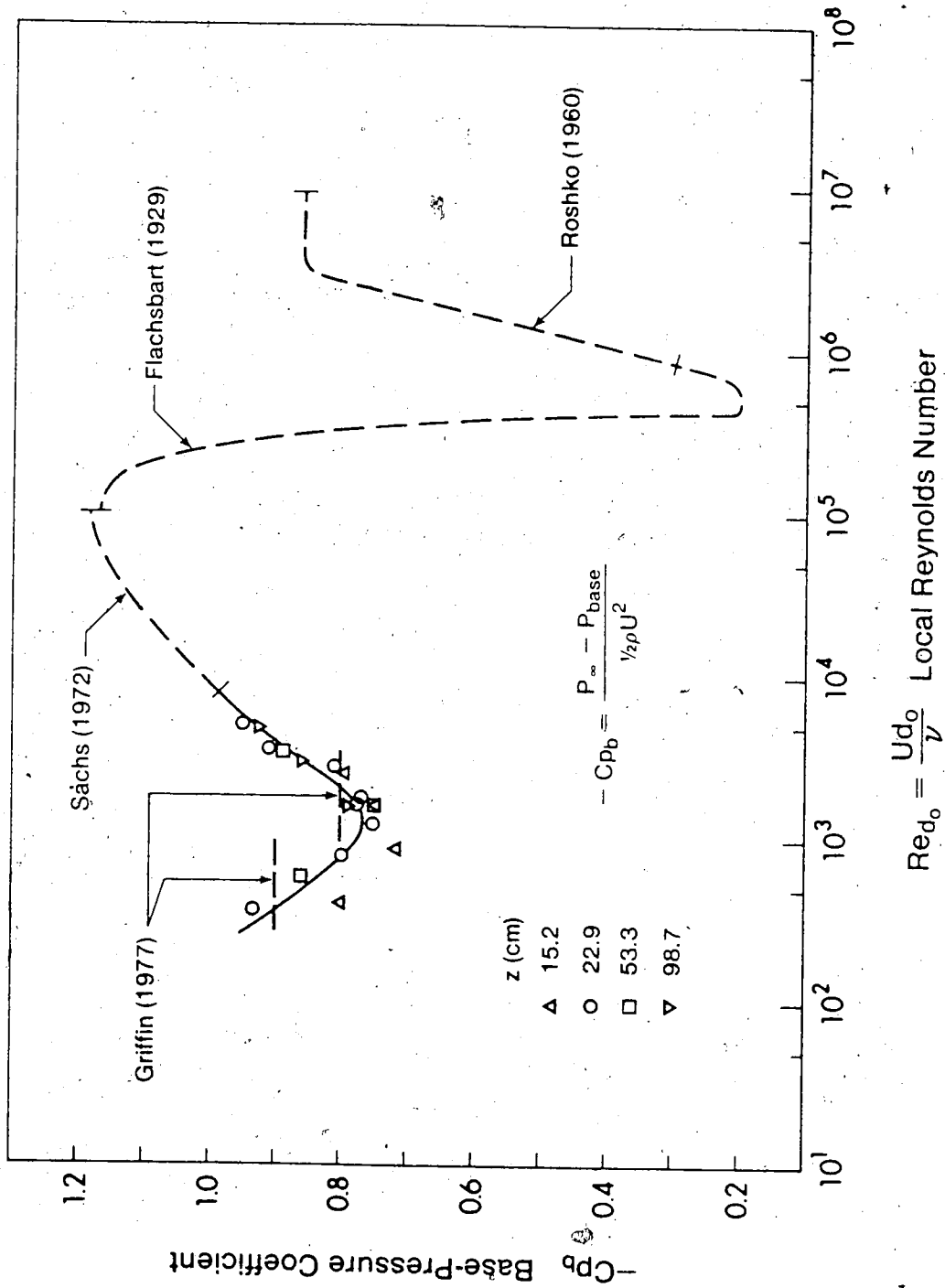
FIGURE 3-2: BASE PRESSURE COEFFICIENTS FOR INFINITE
CIRCULAR CYLINDERS
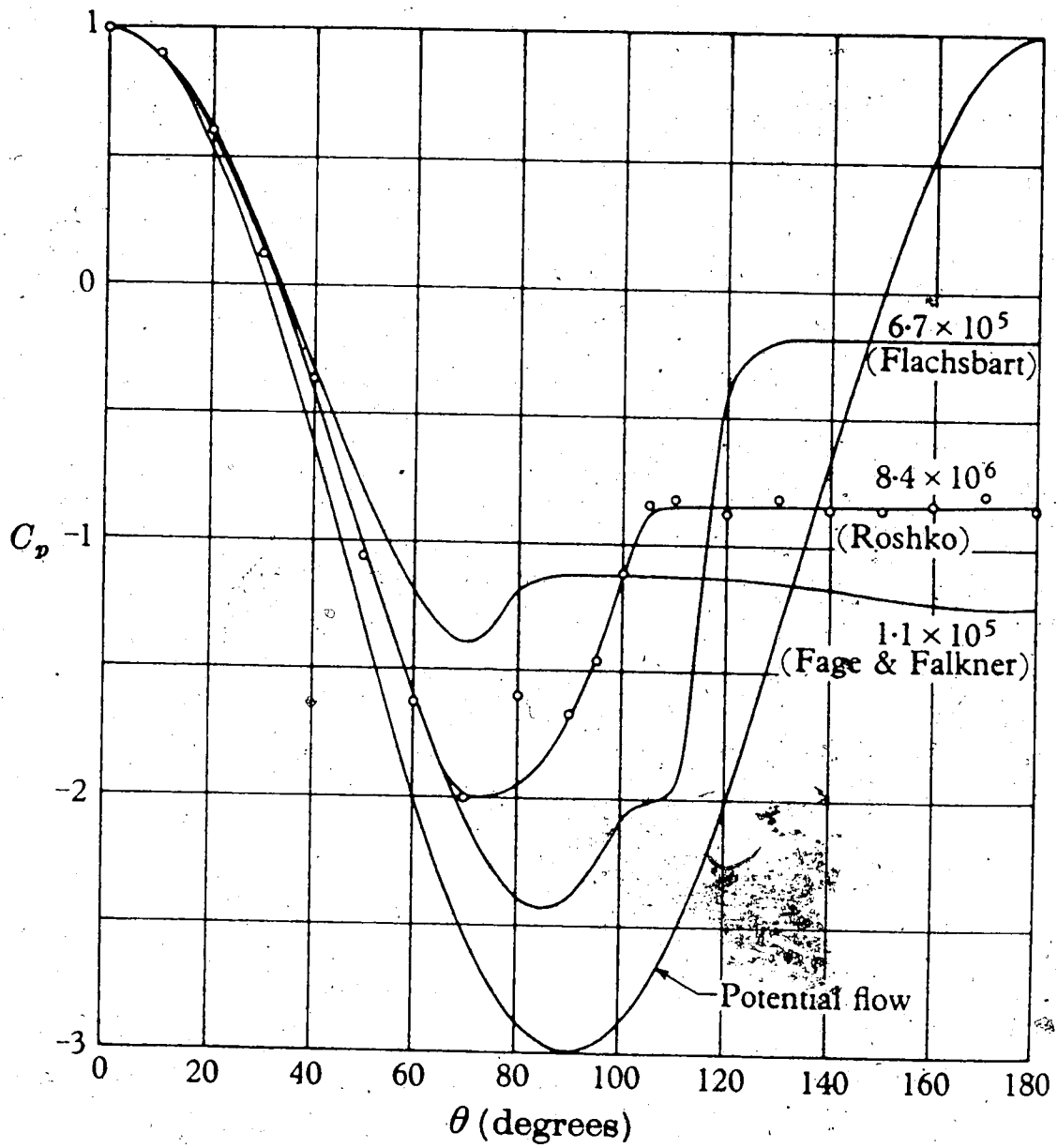
FIGURE 3-3:   PRESSURE COEFFICIENT PROFILES AROUND CIRCULAR
CYLINDERS [FROM ROSHKO (1960)]
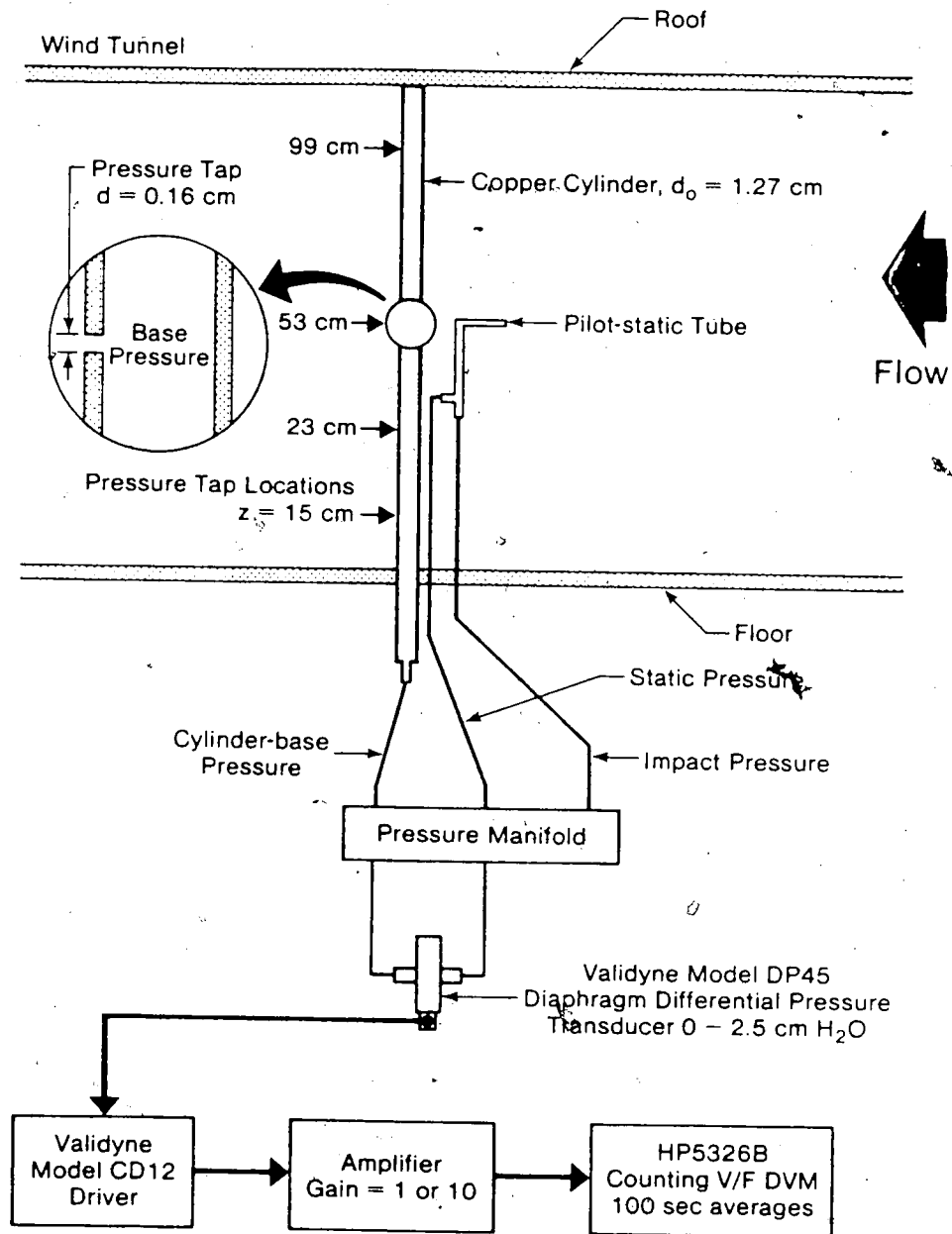
FIGURE 3-4: MEASUREMENT OF CYLINDER BASE PRESSURE COEFFICIENT

CHAPTER IV

PLUME RISE AND STACK DOWNWASH

Introduction

In this chapter, the stack wake effect on plume rise is investigated. Most authors, in the study of plume rise, have tended to either ignore downwash completely, or have simply quantified the downwash effect on plume rise without providing the means for prediction of this phenomenon. Before understanding downwash, one must first understand how plumes rise without downwash, and much of this chapter is devoted to this topic.

Buoyant Plume Rise in a Neutrally Stable Atmosphere

From full scale observations, Csanady (1961) has divided the plume trajectory from a stack into a number of phases: an intial vertical "jet" phase, where momentum effects dominate the rise, a bent-over "thermal" phase, where plume buoyancy dominates the rise, a "break-up" phase, where large atmospheric eddies separate the plume into fairly discrete puffs, and a "disperse" phase, where smaller-scale atmospheric turbulence dominates the motions of the dispersed parcels of stack gas.

Although the distinction between the first two phases is useful in determining how plume momentum and buoyancy effects are different, it is evident that the initial jet gradually and continuously transforms to a bent-over thermal. Therefore, one continuous formulation was sought to describe plume rise from stack exit to the termination

38

of buoyant plume behaviour.

Briggs (1975) has derived sets of governing differential equations for the vertical and bent-over phases of rise for a continuous plume, from relationships for the conservation of mass, buoyancy, and momentum. In the case of neutral atmospheric stability (no change in ambient potential temperature with height), which is the case modelled by a uniform-temperature wind tunnel, these equations simplify greatly, as described below.

For both vertical and bent-over plumes in neutral stability, conservation of buoyancy requires that the buoyancy flux as a function of height, F_z, is constant and equal to the source buoyancy flux, $F = g([\rho_a - \rho_s]/\rho_a)w_s r_s^2$. The potential temperatures of both the plume gas and the ambient air are constant, due to the assumption of adiabatic motion for the former, and the condition of neutral stability for the latter. Therefore, the total (integrated) amount of buoyancy force exerted on the plume must be constant with height. Adiabatic plumes do not include those with condensation or evaporation taking place, or with large radiative or chemically-induced heat transfers.

Conservation of momentum, combined with the above result from conservation of buoyancy, yields the same equation for both vertical and bent-over plumes:

$$\frac{d(\overline{w}V)}{dz} = \frac{F}{\overline{w}} \tag{4-1}$$

In (4-1), $\overline{w}$ is the characteristic vertical velocity of the plume and V is the plume volume flux divided by π (see Briggs (1975) for exact definitions of the integrals for the vertical and bent-over cases).

Equation (4-1) was derived by applying the Navier-Stokes equations to a plume element assuming only pressure and gravity forces. The viscous force term was neglected, bypassing the impossible task of directly computing viscous effects in the turbulent microstructure for the entire flow. In order to account for this omission, a bulk assumption for the effect of turbulent mixing in entraining ambient air into the plume was later made in the mass conservation equations. This is presently the only practical way to account for viscosity and provide a closed set of equations. However, it limits the analysis to prediction of only the gross plume motion (centerline rise).

The equations which arise from conservation of mass take different forms for vertical and bent-over plumes, but have similar character, as shown below.

Vertical Plumes: $\qquad \dfrac{dV}{dz} = 2\beta_1 (\overline{w}\, V)^{1/2}$ $\qquad\qquad$ (4-2)

Bent-over Plumes: $\qquad \dfrac{dV}{dz} = 2\beta_2 (UV)^{1/2}$ $\qquad\qquad$ (4-3)

In the above equations, $\overline{w}$ and U play similar roles in that they are the characteristic plume velocity along the plume axis in each case. The parameters β_1 and β_2 are the Taylor entrainment constants, [Taylor (1945)] which are related to the bulk assumption for entrainment, described below.

Consider a small portion of a circular plume in an arbitrary axis direction, s, as shown below.
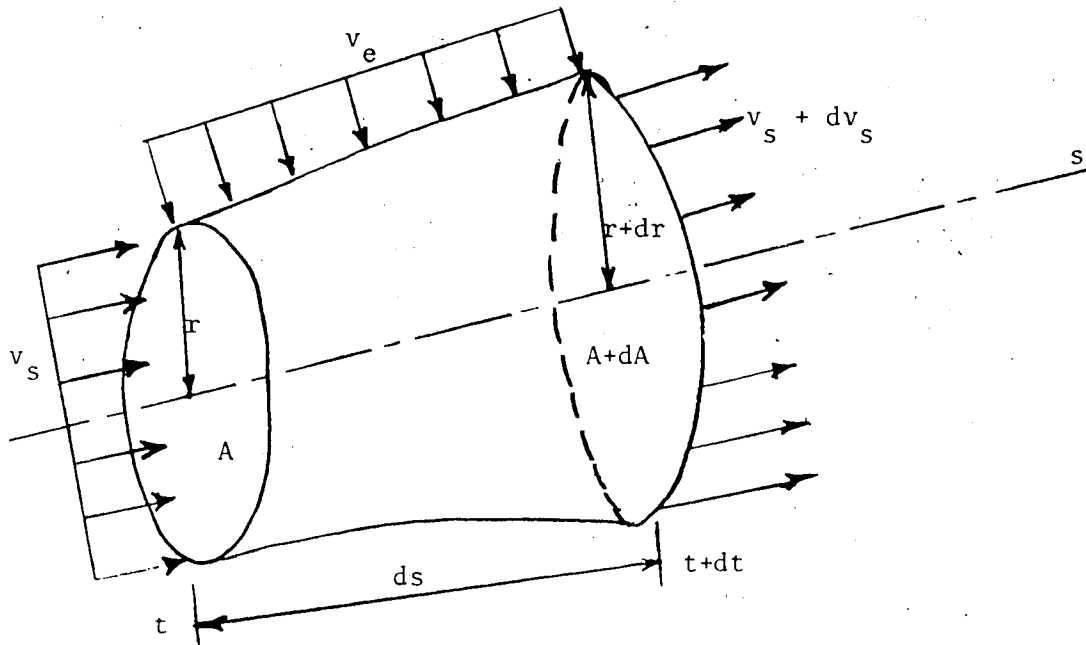
The plume is imagined to have a uniform velocity v_s within a characteristic plume radius, $r = \sqrt{V/v_s}$. This is the so-called "top-hat" plume model.

Entrainment of air into the plume is assumed to occur through the sides at the uniform velocity v_e. By the Boussinesq approximation, where the plume density is taken as equal to the atmospheric density in all terms except those describing buoyancy, mass conservation for the plume element may be evaluated using volume fluxes:

$$\iint_A v_s ds \; + \; v_e 2\pi r ds \; = \; \iint_{A \, + \, dA} (v_s + dv_s) ds$$

With the definition for volume "flux" parameter, $V = (1/\pi)\iint v_s ds$, and in the limit as $ds \to 0$,

$$\frac{dV}{ds} = 2rv_e \qquad\qquad (4\text{-}4)$$

Alternately, (4-4) can be expressed in terms of plume radius, as

$$\frac{dr}{dt} = v_e - \frac{r}{2} \frac{dv_s}{ds} \qquad (4-5)$$

The Taylor entrainment assumption enters through the choice for v_e, using $v_e = \beta_1 \overline{w}$ for vertical plumes and $v_e = \beta_2 \overline{w}$ for bent-over plumes. Substituting these expressions into (4-5), the following expressions are obtained:

Non-Buoyant Vertical Jets: $\qquad \frac{dr}{dz} = 2\beta_1$

Buoyant Bent-Over Plumes: $\qquad \frac{dr}{dz} = \beta_2$

The hypothesis that plume radius grows linearly with height has been experimentally confirmed for full scale buoyant plumes by Briggs (1969) and Bringfelt (1969) using photographically measured plume radii.

Equations (4-2) and (4-3) are obtained by the substitution of the Taylor assumptions for v_e into (4-4).

Combined Rise Formulation for Momentum and Buoyant Rise

Because the conservation equations for momentum and buoyancy have been reduced to one equation, (4-1), for both vertical and bent-over plumes, it was postulated that one continuous plume rise solution could be obtained which would account for both momentum and buoyancy effects. Transforming (4-1) into the time domain with $dt = dz/\overline{w}$, the following is obtained:

$$\frac{d(\overline{w}V)}{dt} = F$$

After integration, the solution is

$$\overline{w} V = Ft + F_M \qquad (4\text{-}6)$$

The constant, F_M, is the value of the momentum flux, $\overline{w}V$, at the
source (t=0). In this analysis, there is no density included in the
momentum flux terms because all plume densities are normalized by ρ_a,
which is the assumed constant density for the flow by the Boussinesq
approximation. Thus, density in the initial stack momentum flux must
also be normalized, so that F_M becomes

$$F_M = \alpha \frac{\rho_s}{\rho_a} w_s^2 r_s^2 \qquad (4\text{-}7)$$

The kinetic energy factor, α, from (2-1), is needed to obtain the
correct total momentum flux when using the average stack gas velocity,
w_s.

A dilemma now appears in that there are two possible entrainment
assumptions in (4-2) and (4-3) to combine with (4-6). Choosing for now
the model for bent-over rise, the plume radius follows $dr/dz = \beta_2$ and thus,
$r = \beta_2 \Delta h + r_o$, where Δh is the plume rise above the stack exit and
r_o is the initial plume radius. From the definition for plume radius,
the volume flux is simply $V = Ur^2$, and the vertical plume velocity is
$\overline{w} = dz/dt$. Combining all of this, the following is obtained:

$$\overline{w} V = U (\beta_2 \Delta h + r_o)^2 \frac{d\Delta h}{dt} \qquad (4\text{-}8)$$

Equating $\overline{w}V$ from (4-8) and (4-6),

$$Ft + F_M = U (\beta_2 \Delta h + r_o)^2 \frac{d\Delta h}{dt} \qquad (4\text{-}9)$$

Assuming initial plume radius $r_o = 0$, (4-9) may be directly integrated to obtain

$$\Delta h^3 = \frac{3F_M}{\beta_2^2 U} t + \frac{3F}{2\beta_2^2 U} t^2 \qquad (4\text{-}10)$$

Examining (4-10), it is seen that the first term has precisely the same form as the "1/3 law" for bent-over jets, which has been shown by Patrick (1967) to be accurate in predicting the rise of jets in a cross-flow. Also, the second term has precisely the same form as the "2/3 law" for buoyant plumes, which has been shown by Briggs (1970) to be applicable to the rise of bent-over buoyant plumes. Thus, (4-10) is very informative: it shows that momentum rise and buoyant rise should add as the sum of cubes in a combined formulation. It seems logical then to solve the dilemma of choosing between the two possible entrainment assumptions by modifying (4-10) to include β_1 in the momentum rise term, and to retain β_2 in the buoyancy rise term. With this modification, and transforming the equation back to x dependence using x = Ut, the combined rise formulation is obtained:

$$\Delta h^3 = \frac{3F_M}{\beta_1^2 U^2} x + \frac{3F}{2\beta_2^2 U^3} x^2 \qquad (4\text{-}11)$$

which is valid only for a uniform velocity U with height. Equation (4-11) is no longer a true solution of the differential equations, but a combination of the 1/3 and 2/3 laws for plume rise.

A finite initial plume radius, r_o, can be included in the combined rise formulation by retaining r_o when integrating (4-9). The

result is

$$\Delta h = \left[\left(\frac{3F_M}{\beta_1^2 U^2} x + \frac{3F}{2\beta_2^2 U^3} x^2 \right) + \left(\frac{r_o}{\beta_2} \right)^3 \right]^{1/3} - \left(\frac{r_o}{\beta_2} \right) \qquad (4\text{-}12)$$

Slawson (1978) derived a similar result including r_o for plume rise in stable atmospheres. Equation (4-12) was not found to be useful in this study because the correction term, r_o/β_2, became unreasonably large near the stack, using $r_o = r_s$. Therefore, the use of r_o and (4-12) was abandoned.

Equation (4-11) may be simplified by the definition of length scales for buoyant and momentum rise. Winkel (1979) has identified a momentum length, L_M, where

$$L_M = \frac{\sqrt{F_M}}{U_s}$$

Many investigators have used a buoyancy length, L_B, where

$$L_B = \frac{F}{U_s^3}$$

With these, (4-11) becomes

$$\Delta h^3 = \frac{3x}{\beta_1^2} L_M^2 + \frac{3x^2}{2\beta_2^2} L_B$$

Measurement of Plume Rise

Plume rise values, $\Delta h = h - h_s$, were measured for plume model B in the turbulent shear flow at windspeeds $U_s = 0.45$ and 0.90 m/s.

Vertical concentration profiles, like the one shown in Figure 2-8,
were taken at a number of downwind positions from the stack, from
x = 1 cm (8 m full scale) to x = 270 cm (2.16 km full scale), using the
methods described in Chapter II. The measured profiles were fitted with
ground-reflected Gaussian distributions (see Chapter VI and Figure 6-2)
and the plume height h was defined as the distance from ground level
to the centerline of the unreflected Gaussian source profile which
would generate the measured reflected profiles, as shown below. In
all cases in this study, the plume height defined in this way was
identical to the height of the point of maximum concentration on the
measured profiles.
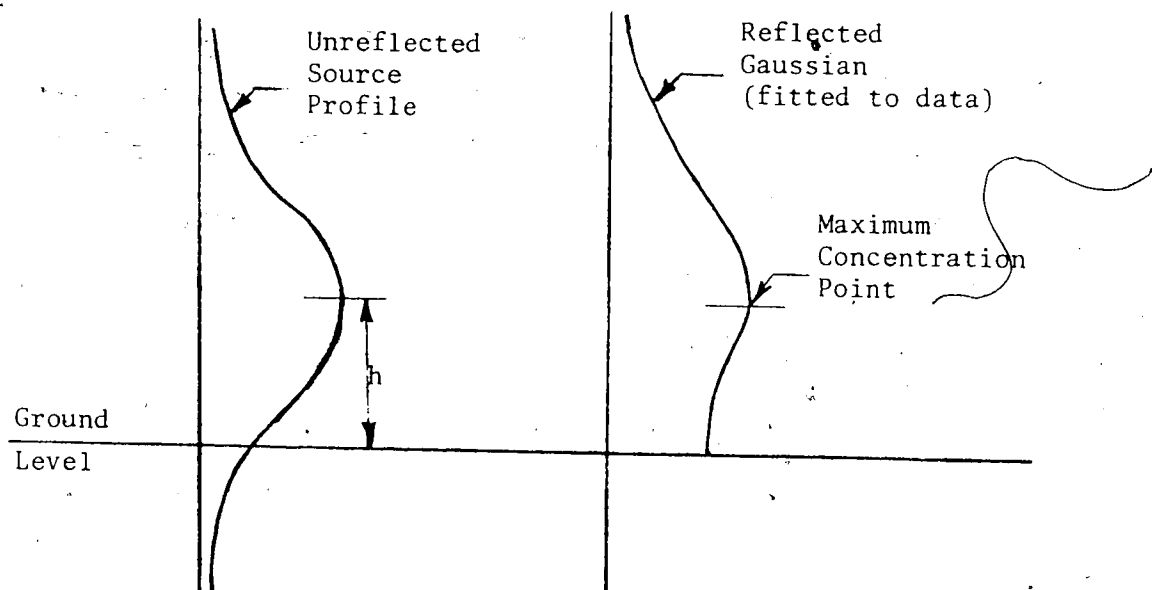
Measured plume heights for model B are plotted in Figure 4-1.

Plume trajectories were also measured by Winkel (1979) for
three variations on model B, denoted as models B1, B2, and B3.
These plumes were tested with one windspeed, U_s = 0.45 m/s, and had

the same stack gas average velocity w_s, density ratio ρ_s/ρ_a, stack diameter d, and stack location as for plume model B.   The conditions that were varied are outlined below:

(1) Model B1 - The stack plug was removed, causing a laminar, parabolic stack velocity profile with $\alpha = 2.0$ ($\alpha = 1.27$ for model B).

(2) Model B2 - The turbulence generation system and plant site model were removed from the tunnel, causing a uniform laminar crossflow to approach the stack. The stack height was raised to $h_s = 45$ cm ($h_s = 22.86$ cm for model B) to avoid the shallow boundary layer on the tunnel floor.

(3) Model B3 - The turbulence generation system and plant site model were removed from the tunnel and replaced with a grid of wooden slats, positioned 2.4 m upwind of the stack. From measurements by Winkel (1979) using the TSI hot-film anemometer system described in Chapter II, the grid was found to produce a downwind velocity field with uniform mean velocity. Turbulent intensity, i_u, was vertically and laterally uniform at any downwind position from the stack, but decayed longitudinally from about $i_u = 0.12$ at the stack location to about $i_u = 0.05$ at x = 300 cm. The stack height was 45 cm.

A further study, denoted as the laminar cross-flow study, was done using three different laminar plumes ($\alpha = 2$) tested in a laminar cross-flow (bare tunnel). The inside stack diameter d was 1.08 cm and the stack density ratio was $\rho_s/\rho_a = 0.425$. In this study, the measured vertical concentration profiles were fitted with hand-

sketched smooth curves to define the maximum concentration height, h. These measurements are shown in Figure 4-2.

Momentum Rise Entrainment Constant β_1

Using data from various investigations, Briggs (1975) has shown that the rise of moment: jₑₜs can be accurately predicted with the 1/3 law when

$$\beta_1 = \frac{1}{3} + \frac{U_s}{w_s} \tag{4-13}$$

This semi-empirical relation is physically reasonable in that jets in a quiescent atmosphere ($U_s = 0$) should still have a small amount of entrainment due to self-generated mixing, and entrainment should increase with U_s/w_s as higher windspeeds cause increased disturbance to the jet and force it closer to the stack wake.

Wilson (unpublished) has suggested a more general β_1 model which is similar in form to (4-13), retaining the same arguments of physical realism, but accounting for dependence of quiescent atmosphere jets on ρ_s/ρ_a from the work of Ricou and Spalding (1961). Also, the ratio U_s/w_s was replaced with $\phi_M = \rho_s w_s^2/\rho_a U_s^2$ which was considered more relevant to plume rise in general. Wilson's model is

$$\beta_1 = 0.33 \left(\frac{\rho_s}{\rho_a}\right)^{1/2} + \phi_M^{-1/2} \tag{4-14}$$

In the present study, which included tests with variable α and ϕ_M, (4-14) was found to yield very accurate rise predictions for the momentum rise phase when used with (4-11). An example of this is

shown in Figure 4-3, where measured plume rise data for plume model B at U_s = 0.45 m/s is compared to the prediction using (4-11), shown as a dashed line. In the coordinates used, the momentum rise portion of (4-11) is a straight line with 1/3 slope and the buoyant rise portion of (4-11) is a 2/3 slope line, as shown. For this particular case, momentum rise is seen to be the dominant form of rise at downwind distances less than about x/L_B = 500. Good agreement between the data and the prediction in this region is observed, using β_1 = 0.87 from (4-14).

The apparent underprediction for the data point near x/L_B = 10 (x = 1 cm) is not significant, because the absolute error of the prediction was only about 0.25 cm in Δh, which was about the resolution of rise calculations.

Buoyancy Rise Entrainment Constant β_2

Difficulties were encountered in defining values of β_2 to be used in the combined rise formulation, because of the lack of a simple comprehensive model, equivalent to (4-14) for jets, which would predict β_2 from stack and atmospheric conditions.

The approach commonly taken in recent literature has been to assign a constant value to β_2. For example, in a study using data from ten sets of buoyant rise observations, Briggs (1972) found an overall best-fit value of β_2 = 0.6, using the 2/3 law. However, best-fit values for the individual studies ranged from β_2 = 0.3 to β_2 = 0.9. Similar wide variations in β_2 were observed in the present study when matching measured rise with the combined rise formulation. Measured values ranged from β_2 = 0.47 to β_2 = 1.4.

The author wished to avoid using β_2 as a mere curve-fitting parameter, because it has physical significance in describing the rate at which a buoyant plume entrains air and grows with height, by $\beta_2 = dr/dz$. Therefore, any variations in β_2 should be explained by physical arguments regarding entrainment. For example, the extra flow turbulence generated by a stack wake would be expected to increase entrainment and β_2. Later, it will be shown that plume rise under moderate levels of downwash can be predicted using adjusted β_2 values.

Entrainment would also be expected to be sensitive to wind shear and turbulence conditions in the atmosphere, because these are related to turbulent mixing. Also, initial stack flow conditions may be important to entrainment. To investigate this effect, measured β_2 values from plume model B, the laminar cross-flow study, and models B1, B2, and B3 from Winkel (1979) are given in Table 4-1, along with stack and approach flow conditions. None of the plumes examined here were significantly affected by stack downwash, so that this effect would not obscure the comparisons.

From Table 4-1, the effects of each of the flow conditions on β_2 could be seen:

(1) Approach Flow Shear - The significantly higher values of β_2 for models B and B1 than all other values in Table 4-1 indi- cate that approach flow shear is the largest single factor in determining β_2. This could be due to two factors: velocity shear gradients enhancing entrainment by moving upper and lower plume layers past each other, or higher mean velocities in the upper regions depressing plume rise in a way not accounted for in (4-11), which used the windspeed at

TABLE 4-1: THE EFFECT OF APPROACH FLOW AND STACK FLOW CONDITIONS ON BUOYANT RISE ENTRAINMENT CONSTANT β_2

Plume Model	β_2	α	Stack Turbulence	Approach Flow Shear	Approach Flow Turbulence
B $(U_s=0.45m/s)$	1.4	1.27	Yes	Yes	Yes
B1*	1.3	2	No	Yes	Yes
B2*	0.87	1.27	Yes	No	No
B3*	0.87	1.27	Yes	No	Yes
Laminar Cross-flow Study $(U_s=0.5$ and 0.1 m/s$)$	0.47	2	No	No	No

*Data and β_2 calculation from Winkel (1979)

stack height, U_s, for all calculations.

(2) <u>Approach Flow Turbulence</u> - By comparing the results for models
B2 and B3 it is seen that approach flow turbulence alone does
not appear to significantly affect β_2. Entrainment is partly
due to buoyancy-induced self-generated turbulence, and partly
due to atmospheric turbulence, and it appears that the latter
is not significant while the plume is still rising.

(3) <u>Stack Flow Conditions</u> - By comparing the results between
models B and B1, or B2 and the laminar cross-flow study, it
is evident that plumes with turbulent stack flows have higher
β_2 values than plumes with laminar stack flows. The differences
in a laminar cross-flow are much greater than those with a
turbulent approach flow. Although the stack profile <u>shape</u>
is accounted for in (4-11) with α, this does not completely
account for the differences in entrainment when stack flows
vary widely.

It is clear that not enough plume rise data was taken in this
study to form a comprehensive model for β_2. However, the results in
Table 4-1 allowed the author, in the case of plumes which were signifi-
cantly affected by stack downwash, to choose an appropriate value of β_2
and predict the rise that likely <u>would have</u> occurred in the absence of
stack wake effects. In this way, the effect of stack downwash could
be quantified.

<u>Final Rise</u>

All plume rise predictions using (4-11) are only valid during
the plume rise phases prior to plume break-up and domination by

atmospheric turbulence. Thereafter, plumes in turbulent shear flows are observed to level off, or achieve final rise. It is possible to define a downwind position, x_{final} at which final rise, Δh_{final} occurs. Choosing x_{final} from a measured trajectory is a somewhat arbitrary decision due to the continuous nature of rise. However, this did not cause great difficulty in this study because the plumes tested were observed to achieve a well-defined final rise in most cases.

A study was conducted, which involved the measuring of three plume trajectories in the present model boundary layer. A laminar stack flow condition was present, and only one buoyancy flux $F = 2.24 \times 10^4$ cm^4/s^3 was used. The stack gas density was constant at $\rho_s/\rho_a = 784$. By varying the windspeed, a fairly wide range of final rise heights and positions were tested. The results are shown in Figure 4-4, with smoothed curves through the measured rise values.

It was postulated that x_{final} might depend on the buoyancy length, $L_B = F/U_s^3$, since this is an important parameter in predicting buoyant rise. Choosing the simplest possible criteria, $x_{final} \propto L_B$, good agreement in final rise position is observed for the three trajectories in Figure 4-4 using

$$x_{final} = 2200\ L_B \qquad\qquad (4\text{-}15)$$

This result was in agreement with studies by Winkel (1979) who investigated final rise for eight other plumes, which involved variations in ρ_s/ρ_a as well as α and ϕ_M. Equation (4-15) was also found to be accurate for the model B plume at $U_s = 0.45$ m/sec as shown in Figure 4-1. Thus, (4-11) combines with (4-15) to produce a complete plume rise model in neutral stability when downwash is not present.

Momentum Flux Ratio ϕ_M as a Downwash Parameter

The stack-atmospheric momentum flux ratio,

$$\phi_M = \frac{\alpha \, \rho_s w_s^2}{\rho_a U_s^2} \tag{4-16}$$

has already been used as a plume modelling parameter to ensure close simulation of the gross interaction between the stack jet and approach flow in the initial momentum rise phase. Stack downwash is also expected to be closely related to ϕ_M, because the downwashing pressure defect in the stack wake is increased by approach flow momentum through $(P_{base} - P_\infty) = \frac{1}{2} C_{Pb} \rho_a U_s^2$. Also, increased stack momentum, $\alpha \rho_s w_s^2$, will tend to lift the plume out of the influence of the stack wake and prevent downwash. Because C_{Pb} was modelled correctly in the present study (see Chapter III), modelling ϕ_M implies modelling stack downwash effects.

Relating downwash to ϕ_M is a more general approach than that commonly found in most investigations. For example, Fay, Escudier, and Hoult (1969) used the simple velocity ratio, $R = w_s/U_s$ to predict stack downwash effects. They found strong stack wake effects when $R < 1.2$. Using this as a rough guide, downwash might be expected to begin to be important in about the region $1 < \phi_M < 2$.

Near Stack Behaviour of Downwashed Plumes

Two sets of near-stack vertical concentration profiles were taken at varying values of ϕ_M. These are relevant because significant concentrations below the stack height at small downwind distances $(x < 2d_o)$ can only be caused by stack downwash; plume spread is insignificant at these distances.

The first set of profiles is shown in Figure 4-5. In these
tests, taken at one diameter from the downwind stack edge, the constant
conditions $\alpha = 2$ and $\rho_s/\rho_a = 0.569$ were tested. Thus, only variations
in w_s and U_s were tested. In Figure 4-5, it is seen that the amount
of downwash increased smoothly with decreasing ϕ_M. Downwash was very
severe at $\phi_M = 0.21$ with measurable concentrations five stack diameter
below stack height. Downwash was insignificant at both $\phi_M = 15$ and
$\phi_M = 3.4$ with no significant concentration measured below one diameter
below stack height. This would indicate that when ϕ_M increases beyond
a certain value, downwash virtually disappears and the value of ϕ_M is
not important.

The second set of profiles is shown in Figure 4-6. In these
tests, taken at less than half a diameter downwind from the trailing
stack edge, α was varied along with w_s and U_s. Again, decreasing ϕ_M
increases stack downwash, even for plumes with different stack-exit
velocity profile shapes. Also, downwash effects are seen to be insigni-
ficant above $\phi_M = 2.57$. It appears that a small concentration will
always be measurable just below the stack level. This is probably due
to the downwashing of the slower-moving stack gas near the inner
wall of the stack.

Prediction of Downwash Effect on Plume Rise

Two plume trajectories were measured which displayed the
effects of stack downwash.

In Figure 4-2, the data at $\phi_M = 1.59$ in the laminar cross-
flow study shows a significant drop in plume rise from the prediction
(shown as a dashed line) using (4-11). Using $\beta_2 = 0.468$ and β_1 from

(4-14), the other two plume trajectories in Figure 4-2 were accurately predicted by (4-11), as seen by the close fit to the data. Except for the stack wake effect, there was no apparent reason why entrainment processes should have differed for the lower plume. However, $\beta_2 = 1.0$ was required to fit the lower plume data, as seen by the solid line through the data. This was a moderate downwash condition, where the rise was suppressed, but could still be modelled with (4-11).

In Figure 4-1, the model B plume at $U_s = 0.9$ m/s ($\phi_M = 0.643$) is clearly a case of severe stack downwash. The plume was observed to achieve its maximum rise of about $\Delta h = 1$ cm directly above the stack. Thereafter the plume was entrained into the stack wake and stayed within about 1 cm of stack height.

The predicted rise of this plume, using (4-11) and (4-15) is shown for both $\beta_2 = 1.4$ and $\beta_2 = 0.87$. The former was the appropriate β_2 value for non-downwashed plumes in the model shear flow, as seen from the upper plume at $U_s = 0.45$ m/s. However, for low-rising plumes, shear effects may not be as significant, and $\beta_2 = 0.87$ is the appropriate value from Table 4-1 for rise in a non-sheared turbulent flow. The difference between these two predictions is seen to be small in this case.

Much more data than that presented in this study would be required to perform a rigorous correlation of downwash effects with ϕ_M. However, from the above results, downwash effects can be divided into three categories:

(1) <u>No Downwash</u>

For conditions of about $\phi_M > 2.0$, stack wake effects are minimal, and rise may be predicted from (4-11) and (4-15).

In laminar approach flows, final rise does not occur and
(4-15) is not applicable.

(2) Rise Partially Suppressed by Downwash.

For conditions of about $1.0 < \phi_M < 2.0$, rise may be predicted
by (4-11) using increased β_2 values. The following form is
suggested to calculate the increase in β_2, which is based on
the assumption of no effect at $\phi_M = 2.0$ and the data in
Figure 4-2.

$$\beta_2 \text{ (with downwash)} = \beta_2 (6 - 2.5 \phi_M)$$

$$\text{for } 1.0 < \phi_M < 2.0$$

This is only a rough estimate, but has the correct trend
with ϕ_M.

(3) Rise Completely Suppressed by Downwash

For conditions of about $\phi_M < 1.0$, stack wake effects will be
severe, and a reasonable rise estimate is $\Delta h = 0$.

With the above downwash categories, and the rise models (4-11)
and (4-15), rise may be accurately predicted for plumes with both
momentum and buoyancy in neutrally stable atmospheres.

Buoyancy Flux F = 0.92185 x 10^4 cm^4/sec^3
Kinetic Energy Factor α = 1.27

x = 2200 L$_B$

Momentum   Windspeed
Ratio ϕ_M U$_s$ (m/s)

● 2.570   0.45

○ 0.643   0.90

Computed Rise
$\beta_1 = 0.87$ $\beta_2 = 1.4$

$\beta_1 = 1.50$ $\beta_2 = 0.87$

$\beta_1 = 1.50$ $\beta_2 = 1.4$

x = 2200 L$_B$

Stack Height 22.86

45

40

35

30

25

20

Z   Model Height Above Ground (cm)

0   100   200   300

X   Model Downwind Distance (cm)
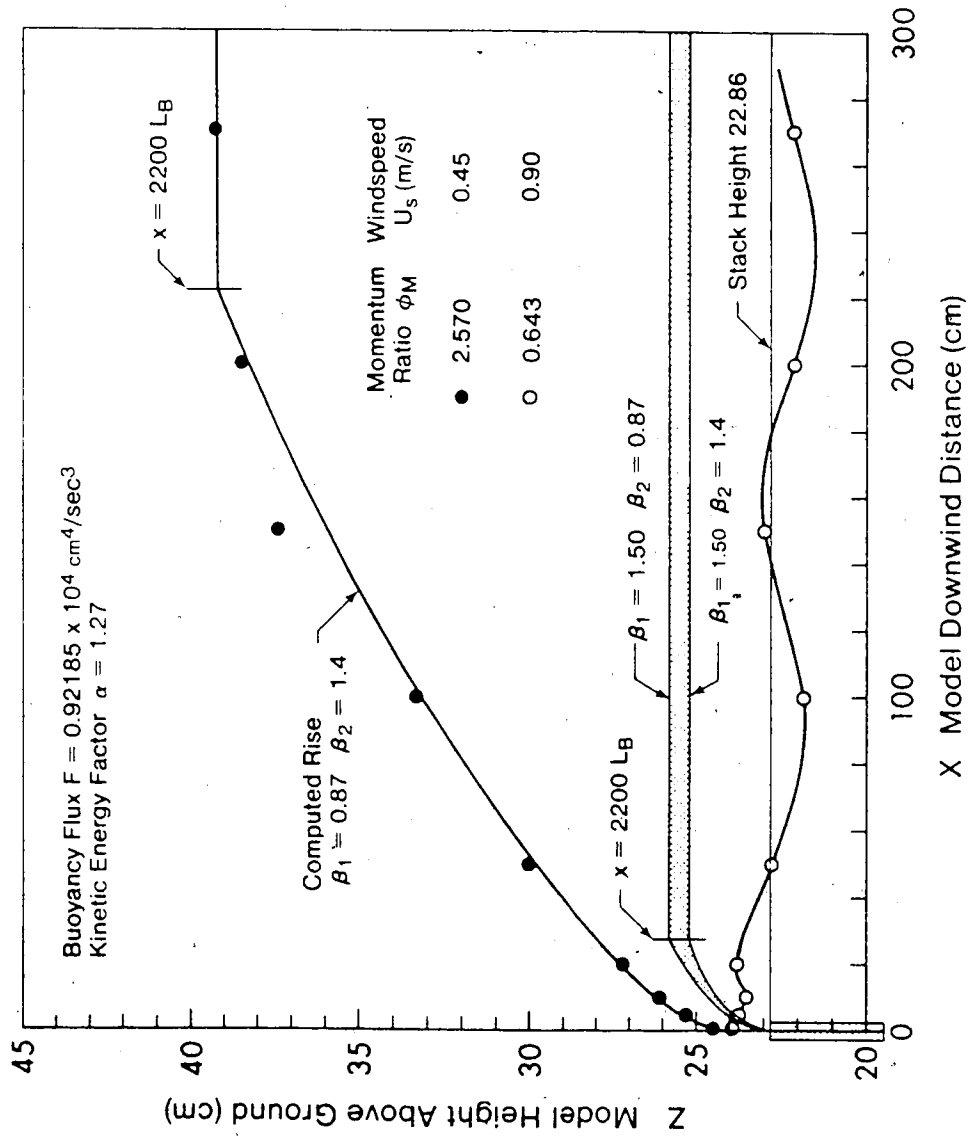
FIGURE 4-1:   MEASURED AND PREDICTED PLUME TRAJECTORIES FOR
MODEL B PLUMES
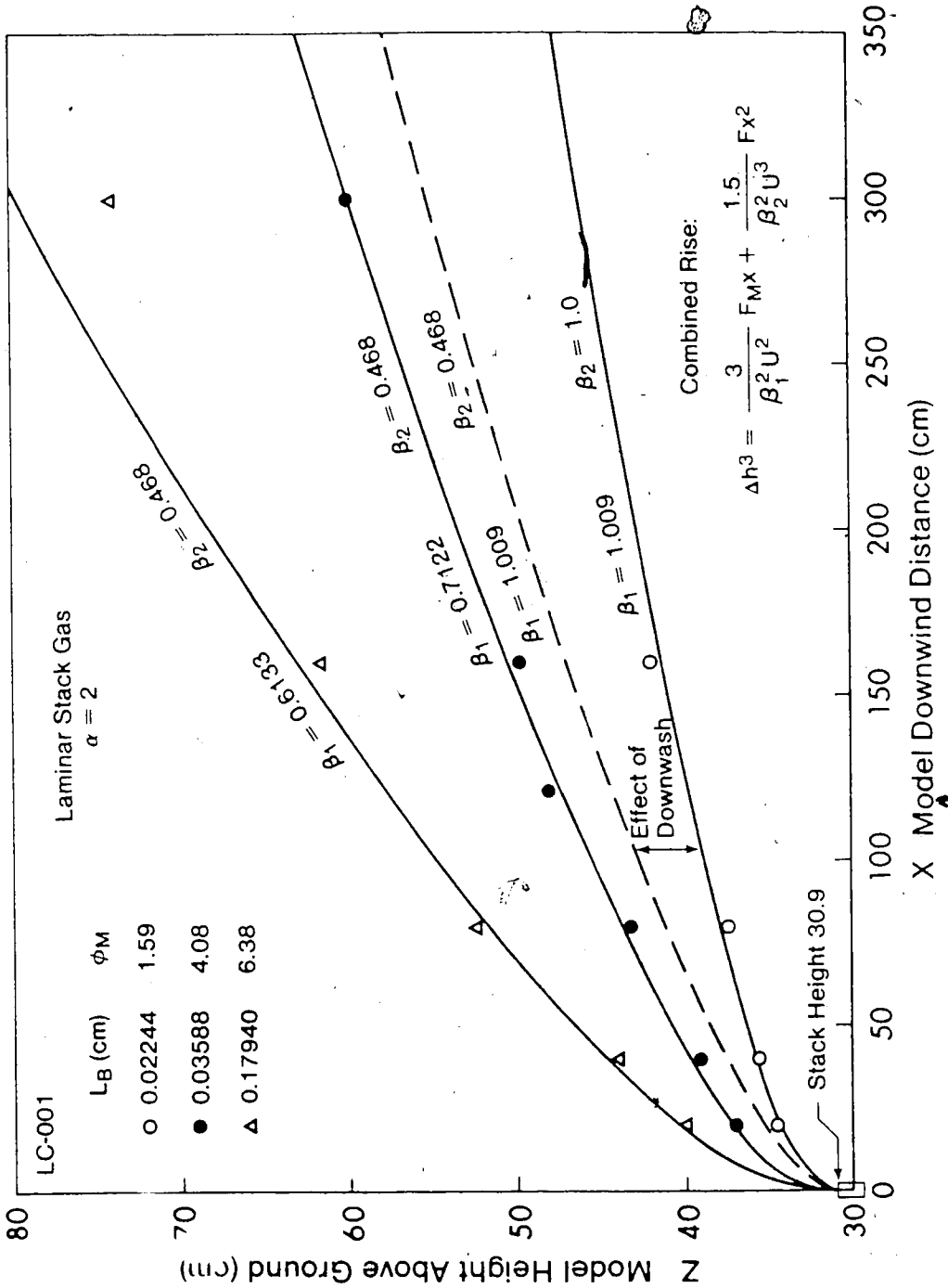
FIGURE 4-2: MEASURED AND PREDICTED PLUME TRAJECTORIES FROM THE LAMINAR CROSS-FLOW STUDY

60

Combined Rise:

$$\Delta h^3 = \underbrace{\frac{3}{\beta_1^2 U^2} F_M x}_{\substack{\text{Momentum} \\ \text{Rise}}} + \underbrace{\frac{1.5}{\beta_2^2 U^3} F x^2}_{\substack{\text{Buoyant} \\ \text{Rise}}}$$

Wind Speed U_s (m/s)	0.45	
Buoyancy Flux F (cm⁴/s³)	9219	
Momentum Ratio, ϕ_M	2.57	
Kinetic Energy Factor, α	1.27	
Stack Gas	Turbulent	

Combined Rise
$\beta_1 = 0.87$
$\beta_2 = 1.4$

Momentum Rise
$\beta_1 = 0.87$

Buoyant Rise
$\beta_2 = 1.4$

Final Rise

$x = 2200\ L_B$

$\frac{\Delta h}{L_B}$ Dimensionless Plume Rise

$\frac{x}{L_B}$ Dimensionless Downwind Distance

10^3 10^2 10^1

5 10^1 10^2 10^3 5×10^3
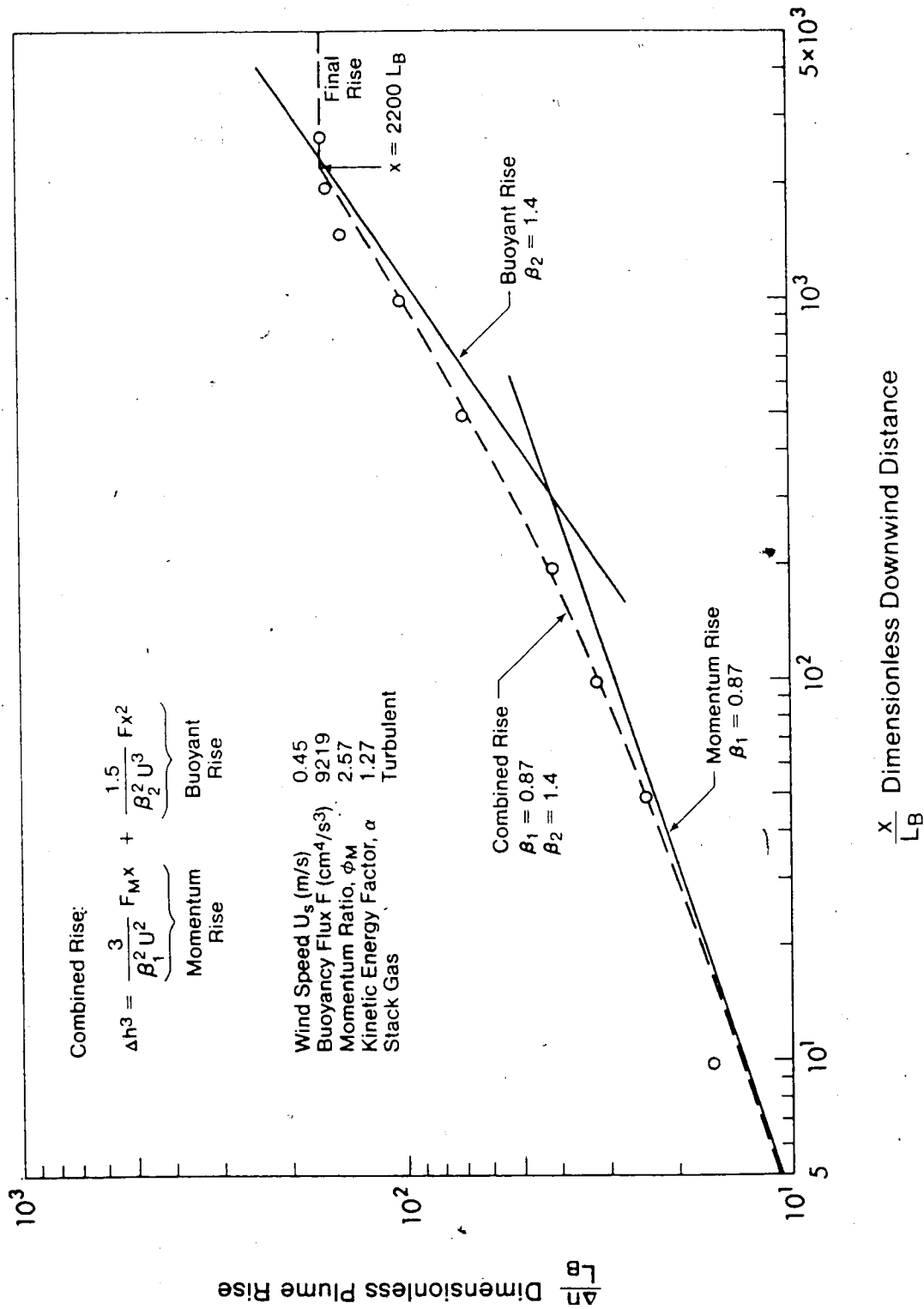
FIGURE 4-3: MODEL B PLUME RISE AT $U_s = 0.45$ m/s FITTED WITH THE COMBINED RISE FORMULATION
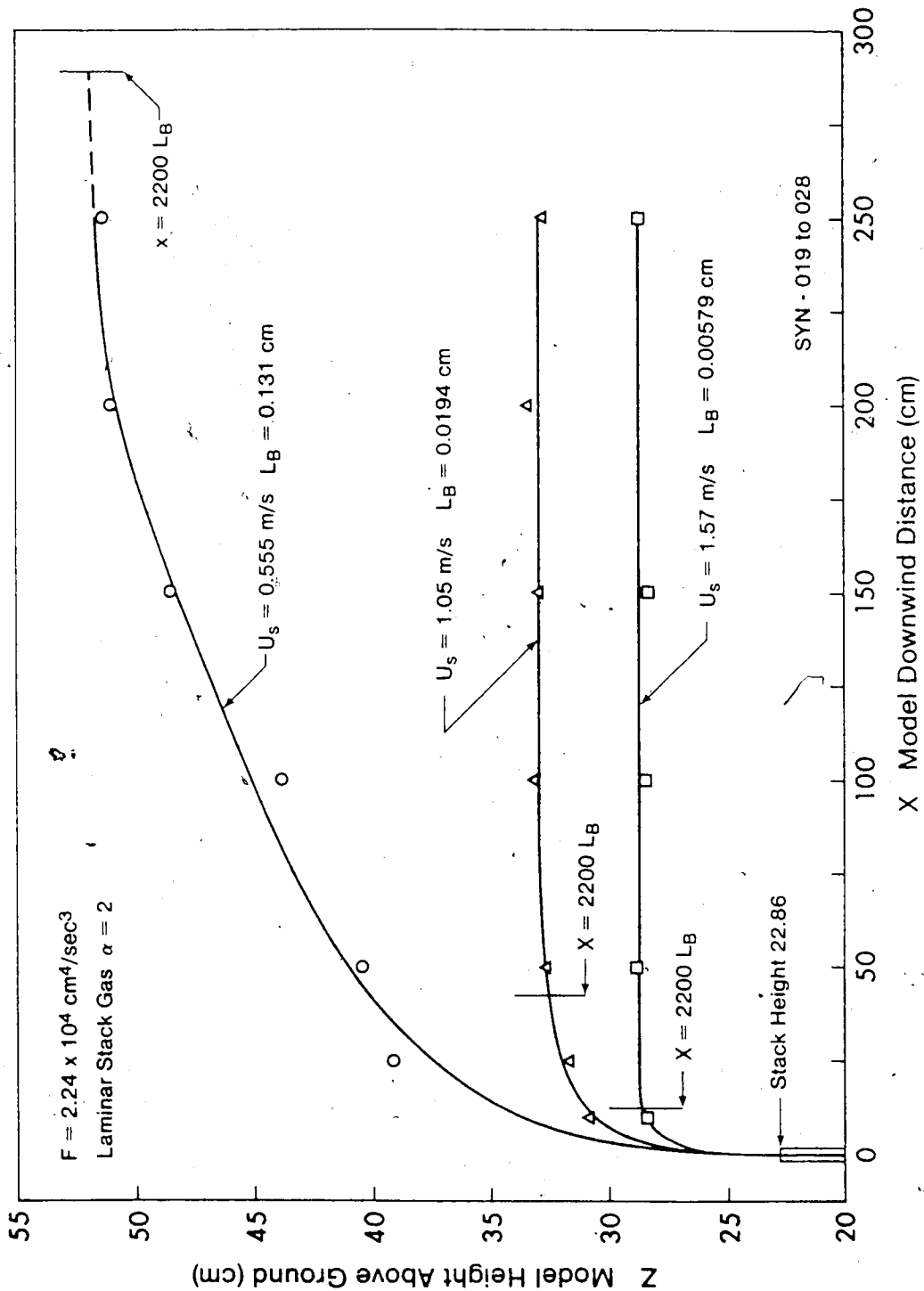
FIGURE 4-4: FINAL RISE OBSERVATIONS IN THE WIND TUNNEL

62

Plume Centerline

Profiles Below From Lower Plume Edge

Stack

d_o

d_o

2 cm

$\alpha = 2.0$ $\dfrac{\rho_s}{\rho_a} = 0.569$ $C_s = 0.5$

$\phi_M = \alpha \left(\dfrac{\rho_s}{\rho_a}\right)\left(\dfrac{W_s}{U_s}\right)^2$

U_s (m/s)		ϕ_M	Run
○	0.529	14.80	ME 008
◇	1.10	3.44	ME 007
△	1.11	0.834	ME 009
□	1.12	0.205	ME 010

C/C_s × 1000 Model Concentration Ratio

Model Distance Below Stack Top, cm

Distance Below Stack Top, diameters
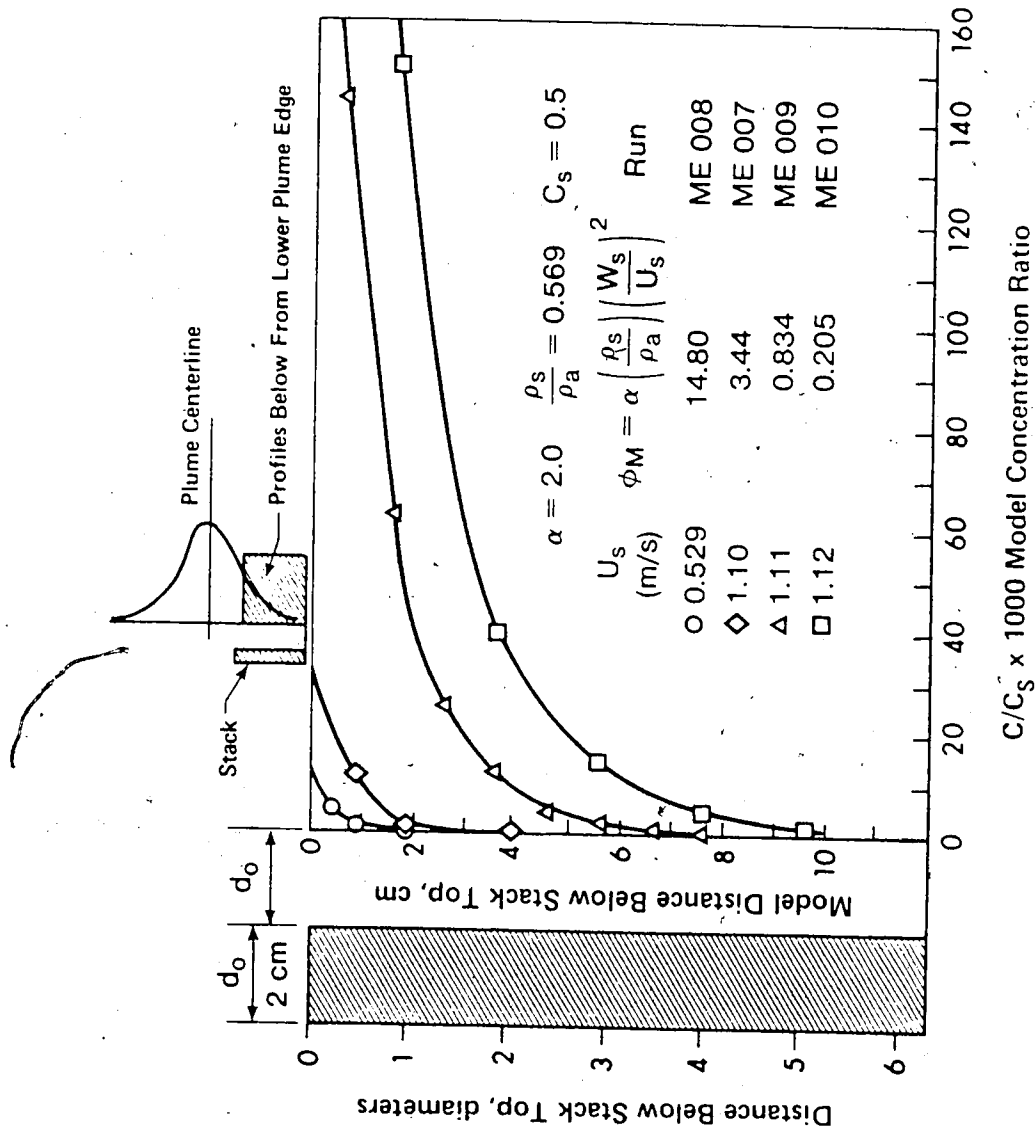
FIGURE 4-5: NEAR-STACK VERTICAL CONCENTRATION PROFILES AT $x = 1.5\ d_o$ FOR PLUMES UNDER THE INFLUENCE OF STACK DOWNWASH

Distance Above Stack Top (diameters)

1   0   -1   -2   -3

x = 1 cm

d_o = 1.27 cm

Stack

0   10   20   30   40   50

$\left[\dfrac{C}{C_{Stack}}\right]$ × 1000   Normalized Concentration

Run	$\phi_M = \alpha \dfrac{\rho_s \dot{w}_s^2}{\rho_a U_s^2}$	α
○ SYN - 150	0.643	1.27
△ SYN - 174	1.010	2.00
□ SYN - 149	2.570	1.27
▽ SYN - 173	4.050	2.00
● SYN - 194	4.110	1.27
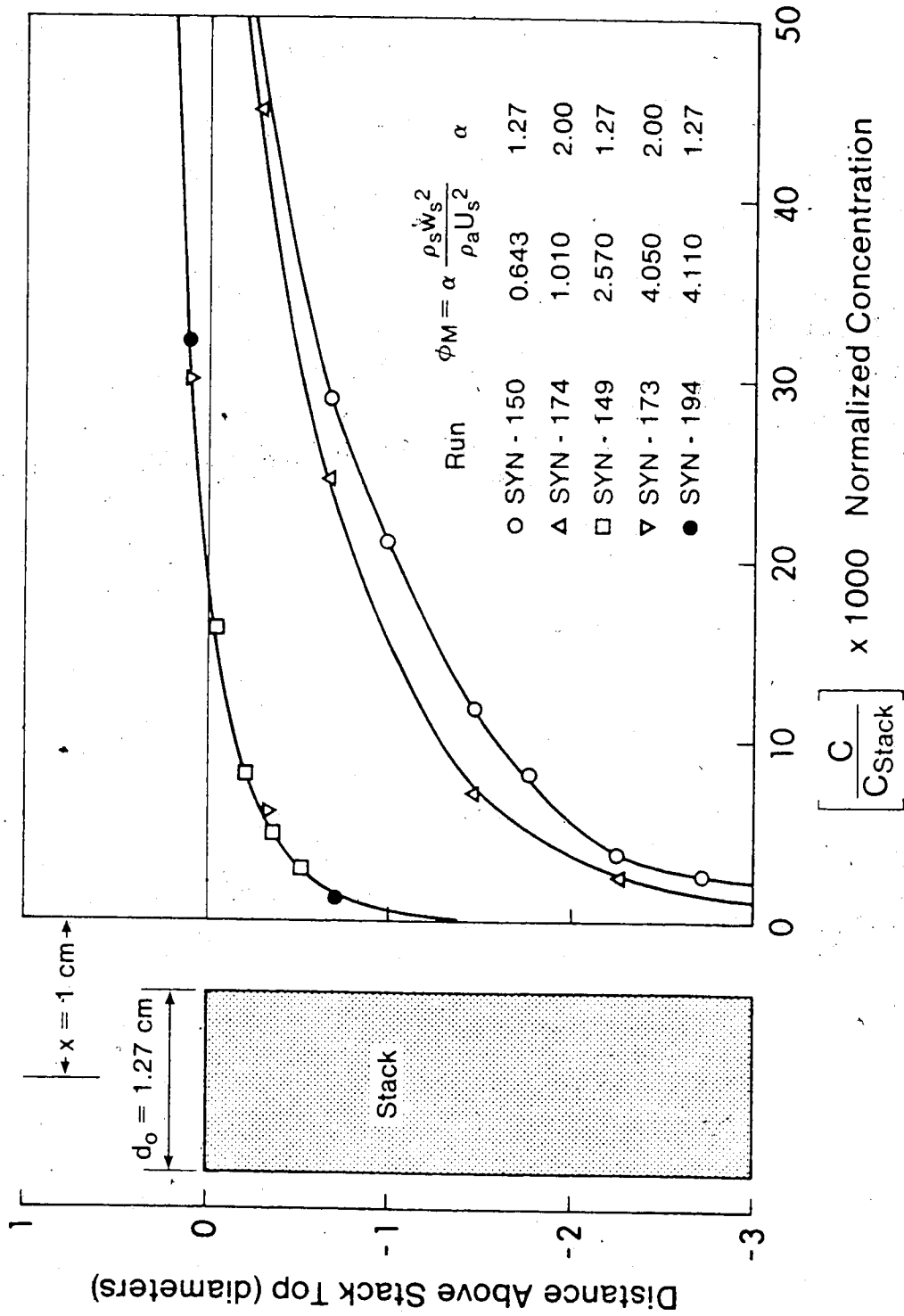
FIGURE 4-6: NEAR-STACK VERTICAL CONCENTRATION PROFILES AT
$x = 0.8\, d_o$ FOR PLUMES UNDER THE INFLUENCE OF
STACK DOWNWASH

CHAPTER V

FLOW RECIRCULATION BEHIND DIKES

Introduction

It was seen in Chapter III that the Reynolds number is signifi-
cant in determining the proper modelling of stack wake suction and plume
downwash. In this chapter we focus our attention on the wake flows
behind much larger two-dimensional flow obstacles: the dikes which
surround tailings ponds typically occurring on oil sands strip-mining
sites.

Dikes are similar to stack cylinders in that the large mismatch
in Reynolds number between the wind tunnel model and full scale is again
found to be a significant potential source of error. However, unlike
cylinder flow, the flow around such arbitrarily-shaped obstacles as
dikes is more difficult to predict. It was found that these
flows require modification to account for Reynolds number effects before
the dikes can be used in a wind tunnel dispersion model without serious
modelling error.

Previous Investigations of Recirculation

The results of several previous studies of recirculating flows
are helpful in demonstrating the following:

(a) The amount of sensitivity of recirculating flows to Reynolds
number for different obstacle shapes.

(b) Problems with quantifying the size and influence of a recircu-
lation zone.

(c) Factors other than Reynolds number that may require modelling

for proper simulation of a dike wake.

For sharp-edged objects, the wake flow is quite insensitive to Reynolds number because separation always occurs at the leading sharp edge, thus essentially fixing the size of the resulting recirculation zone. The collected data in Table 5-1 for measured recirculation lengths L_c/H behind thin sharp-edged walls supports this claim. L_c is the distance from the wall to the point of reattachment of the recirculating zone on the downstream surface, and H is the height of the wall. It is seen in Table 5-1 that the decreasing trend of L_c/H down the table does not appear to be correlated with changes in Re_H.

At the other extreme, gently curved obstacles will also be Reynolds number insensitive because separation and recirculation will not normally occur. However, many commonly-occurring flow obstacles which are rounded but not sharp-edged exhibit dramatic sensitivity to Reynolds number, as discussed in Chapter III for circular cylinders. The dikes tested in this study also fall into this latter category, requiring careful investigation of the effect of Reynolds number.

In attempting to measure the reattachment length L_c behind an obstacle, problems with flow fluctuation are often encountered. Instantaneously observed reattachment lengths may vary considerably around a mean value, as found by Wilson, Winkel, and Neiman (1979) in a flow visualization study of recirculation zones behind model walls and dikes in a water channel. Figure 5-1 shows the results of two such tests where the fluctuating reattachment zone was found by injecting small puffs of dye near the floor surface and observing whether the puffs were carried upstream or downstream. The two positions beyond which the puffs always

TABLE 5-1:   FLOW REATTACHMENT LENGTH BEHIND TWO-DIMENSIONAL WALLS
IMMERSED IN A BOUNDARY LAYER

Investigator	$Re_H = \dfrac{U_H H}{\nu}$	$\dfrac{\delta}{H}$	$\dfrac{L_c}{H}$
Arie and Rouse (1956)	3×10^4	0	16.8
Good and Joubert (1968)	1.76×10^5	0.75	13.3
Chang (1966)	4.7×10^4	6	12.8
Plate and Lin (1964)	2×10^4	6	12
Wilson, Winkel and Neiman (1979)	7.3×10^3	5	9.5
Present study	6.3×10^4	8.6	9.05

moved upstream or downstream defined the boundaries of the zone. From Figure 5-1 this zone was typically 30-40% the length of the mean cavity length L_c. The implication of this is that simple flow visualization techniques for measuring L_c by observing how far downstream recirculation occurs may overpredict L_c by perhaps as much as 20%. A far downstream fluctuation of L_c will always leave dye behind when it recedes, and this may obscure the true mean position. These results led the author to exercise caution when comparing measured reattachment lengths from different experimental techniques, and pointed to the need for a technique to measure the true mean length.

Recirculating flows may also be sensitive to approach flow turbulence; greater turbulence levels being expected to induce earlier reattachment. The parameter δ/H for a recirculation study, where δ is the boundary layer thickness, can serve as a measure of this effect since turbulence intensity decays with height in a boundary layer to small values at height δ. Thus, if δ/H is large, the recirculating flow will experience high turbulence levels and should have a smaller value of L_c/H. This general trend is seen to occur for the data shown in Table 5-1, indicating the need to properly model the parameter δ/H and the corresponding boundary layer turbulence levels for the recirculation tests on model dikes in the present study.

Wind Tunnel Recirculation Tests

Tests were conducted in the wind tunnel boundary layer and plant site model described in Chapter II. Three dike sizes, referred to throughout this study as large, medium, and small, were tested, with dimensions given in Table 5-2. The dikes were always mounted with their crests

TABLE 5-2: MODEL DIKES TESTED

Dike	H(cm)	W(cm)	W_c (cm)	S	Construction
Small	2.86	18.7	1.9	0.33	Wood
Medium	5.72	35.4	1.9	0.33	Wood
Large	11.75	70.5	1.9	0.34	Sheet Metal

DIKE CROSS-SECTION
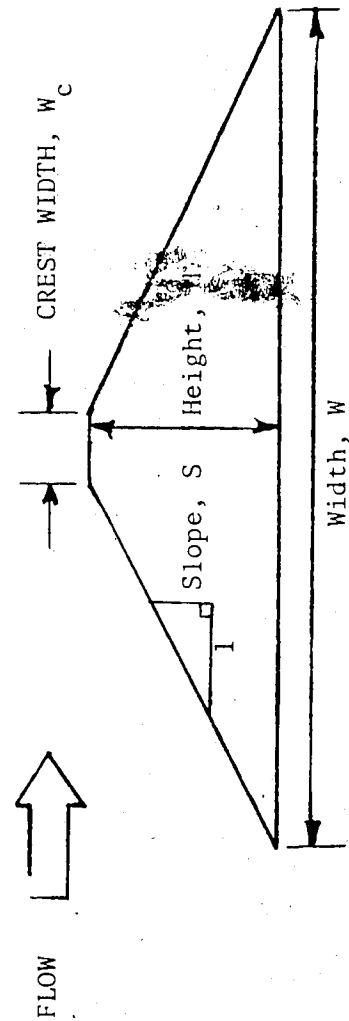
perpendicular to the flow in the "upstream" dike position shown in Figure 2- 2. A 10.4 cm high sharp-edged wall was also tested for recirculation.

The dikes were always tested with the same base surface level on both sides, which implies a low water level in the tailings pond.

Flow Reattachment Detector

Because of fluctuation of the reattachment point shown in Figure 5-1, a technique was developed to measure the true mean reattachment length of a recirculating flow. This consisted of a probe mounted on the floor surface downwind of the obstacle, and an external measurement and monitoring system, shown schematically in Figure 5-2. Its principle of operation was to inject helium tracer gas from a central source tube perpendicularly onto the surface and to allow the local surface flow to carry the tracer to either one or both of two helium detector probes positioned 1 cm upwind and downwind of the source. The two detector probes were simply tubes into which samples were simultaneously aspirated and fed into the sample and reference sides of the helium detector bridge described in Chapter II. The mean direction of surface air flow (upwind or downwind) was indicated by the probe which gave the largest reading over a suitably long averaging time. Actually, the two detector readings were instantaneously subtracted so that the polarity of the net reading yielded the flow direction. When the detector was located so that the net reading was zero, this position was taken as the mean point of reattachment for the recirculation zone. Example readings for two flow conditions are given in Figure 5-2 for measurement locations A and B. In the first example with Re_H = 1990, the mean point of

reattachment must lie between A and B because the surface air flow was upwind at A and downwind at B, as shown in the figure. In the second example with Re_H = 14200, the recirculation zone was much smaller, with downwind flow at both A and B.

By moving the probe and observing the readings as above, the reattachment length L_c could be measured for a given dike and approach velocity. For greater sensitivity in reading, the helium detector output was usually given a DC offset and measured on a voltage to frequency averaging digital voltmeter for 100 sec. samples.

The detector system had one operating disadvantage in that it could normally only be used on a horizontal surface. On an inclined surface such as a dike face, the buoyant helium tracer gas tended to migrate uphill and biased the reading significantly. This was not a serious problem because at most Reynolds numbers the mean reattachment point extended beyond the downwind edge of the dike base.

Experimental Results

Using the flow reattachment detector, reattachment lengths were measured for the three dikes over a range of Reynolds numbers from lower than typical model values to as high as the tunnel would safely permit. The results are plotted in Figure 5-3 for two different choices for Reynolds number, along with two measurements in a water channel from Wilson, Winkel, and Neiman (1979).

The first choice for a correlation parameter, $Re_H = \dfrac{U_H H}{\nu}$, was made using the dike and tunnel parameters that were varied during the tests. It is seen from Figure 5-3 that this yields only a fair correlation of the data. This seemed to indicate that the proper Reynolds number to correlate reattachment lengths should not depend on the obstacle

itself, but only on the approach flow. The necessary information on the dike height would then be contained only in L_c/H. The second choice, $Re_\theta = \dfrac{U_\delta \theta}{\nu}$ used the momentum thickness of the approach flow boundary layer $\theta = 13.14$ cm, found from integration of the wind tunnel vertical velocity profile given in Chapter 2. The boundary layer thickness $\delta = 94$ cm was used to calculate U_δ from the power-law fit to the velocity profile, starting with the measured values of U_H in each case. In Figure 5-3 it is seen that Re_θ correlates the data much better than Re_H, although it is impossible to say whether some other approach flow parameters than θ and U_δ would provide the best correlation in general, because only one boundary layer was tested.

Two explanations are offered for the 20-30% increase in L_c/H for the water channel data and the large dike data over the curve in Figure 5-3 for the two smaller dikes.

One possible explanation involves the effect of approach flow turbulence, which tends to retard reattachment. This is analogous to the arguments used to explain the variations in the data of Table 5-1. Clearly, δ/H increases as L_c/H decreases for the data in Figure 5-3 and this may be due to a decrease in turbulence as higher dikes encounter lower levels of boundary layer turbulence.

The second explanation involves the effect of tunnel area block-age by the dikes. Any obstacle in a fixed-area tunnel reduces the effec-tive flow area and causes an acceleration past the obstacle with a corresponding static pressure drop. When the flow decelerates past the obstacle the pressure returns to the higher ambient levels. These condi-tions of deceleration against an adverse pressure gradient are exactly those that enhance separation and retard reattachment. This effect was

measured by Good and Joubert (1968) who found that rear separation bubbles behind walls in turbulent boundary layers were affected by pressure gradients induced by tunnel blockage. Interestingly, for fixed area tunnels where δ is close to the tunnel height, such as in the present study and the water channel study, δ/H and tunnel blockage are inversely proportional to each other. Therefore, both turbulence levels and blockage varied with δ/H, so it was not possible to assign the effects on reattachment to one or the other, although tunnel blockage is probably the more likely explanation.

Figure 5-4 shows the correlation of L_c/H with tunnel area blockage as taken from the data in Figure 5-3 at $Re_\theta = 9600$. From this it may be concluded that recirculation will not be affected by tunnel blockages up to about 5%, but may increase significantly when the blockage is greater.

Implications of Reynolds Number Mismatch

Figure 5-3 shows that the wake flows behind the dikes in the present study are very sensitive to Reynolds number, as well as second-order effects such as tunnel blockage. Recirculation zones appear to shrink to negligible size when Reynolds numbers increase to about $Re_\theta \sim 2 \times 10^5$, one to two orders of magnitude above model values, which were typically from $Re_\theta = 10^3$ to 10^4. Because the corresponding full scale values are of about order 10^7, it follows that the present dike model, if used, would greatly exaggerate the size and influence of the dike recirculation zone. Full scale measurements by Eliseev (1973) support this, indicating that for full scale hills about 10° steeper than the present model dikes, $L_c/H = 2$ for $Re_H = 10^7$. This means that

full scale dikes would be expected to have L_c/H less than 2 at the same Reynolds number.

Because it was the purpose of this study to gauge the effect of dike recirculation zones on air pollution dispersion, this modelling error was considered very serious and could not be tolerated. Model Reynolds number could not be altered due to stack plume modelling considerations, so a remedy was sought by modifying the dike flows as they existed.

Dike Deflector Vane

A thin metal deflector vane was mounted along the entire length of the model dike crests to provide flow in the model close to that of full scale conditions. Since elimination of the large recirculation zones was the goal, the vane was designed to force the flow down the leeward side of the dikes as shown below.

DIKE AND VANE CROSS-SECTION

FLOW

DEFLECTOR VANE (18 gauge sheet metal)

2.5 cm

5.1 cm

2.8 cm

DIKE CREST

1

3
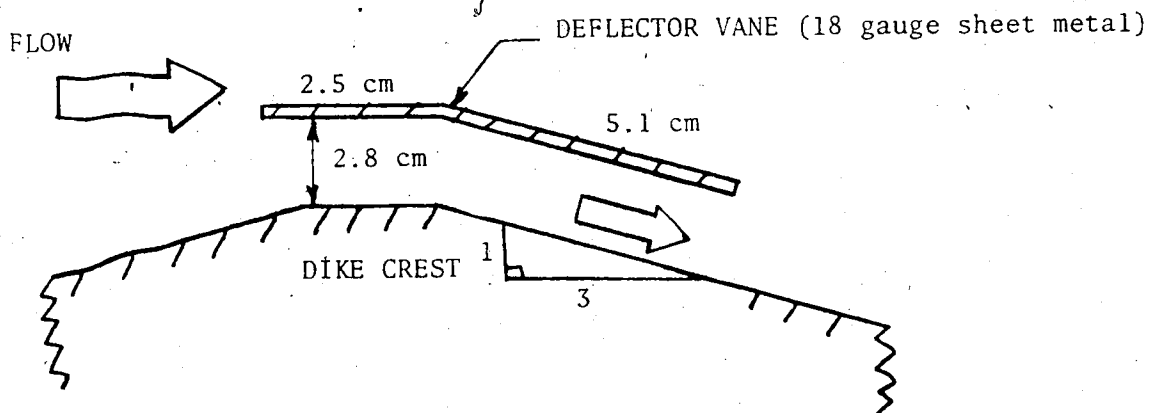
Flow visualization studies were undertaken in the wind tunnel to qualitatively evaluate and optimize the performance of the vane. These were done using titanium tetrachloride smoke released upstream of the dikes. Only the large and medium dikes were tested (or used again in this study), and the same vane was used for both dikes. After finding the optimum spacing between the dike crest and vane, the vane was observed to almost completely eliminate recirculation zones behind both dikes at all model Reynolds numbers. Some typical results are given in Figure 5-5 where recirculation zones were sketched from flow visualization. At an intermediate Reynolds number between those in the top two sketches where flow recirculation zones were both large, the bottom sketch with the vane in use shows recirculation isolated to two small areas: one near the dike base, and one immediately behind the vane. These zones diminished with increasing Reynolds number and were never observed to be larger than those shown in Figure 5-5.

Use of the helium flow reattachment detector confirmed the success of the vane. Tests showed that net upwind surface flow could not be measured at a distance 5 cm downwind of the large dike base at any tunnel speed. Also, at distances of 2.5 cm behind the medium dike base and 1.3 cm behind the large dike base, recirculation was measurable only when Reynolds number was reduced to $Re_\theta < 4 \times 10^3$.

Comparison of Dike Model to Full Scale

All of the above tests for dike models considered only the size of the recirculation zone as an initial gauge of the validity of the model. To further verify that the vane was operating correctly, the effects of the model dikes on downstream mean and turbulent flow

patterns were measured and compared to the expected full scale effects. In the absence of full scale data, the substitute used was to operate the tunnel at a high Reynolds number, $Re_\theta = 1.3 \times 10^5$, with the vane removed. Figure 5-3 shows that the recirculation zone behind the dikes has already decreased to negligible size at this Reynolds number, indicating a proper simulation of full scale conditions. This data will be referred to below as the "full scale condition". The typical model condition tested for comparison was operated with $Re_\theta = 1.1 \times 10^4$ ($U_H = 0.72$ m/s) using the dike with and without the vane.

With a linearized single hot-film anemometer, rtical profiles of mean velocity U and turbulent intensity $i_u = \sqrt{\overline{u^2}} / U$ were taken at a location x = 7H(82.25 cm) downstream of the large dike, as shown in Figure 2- 2. The equipment set-up for turbulence measurement is shown in Figure 2- 4.

In Figure 5-6 the results are presented for mean velocity profiles at the "full scale" condition, with and without the dike present. The normalizing mean velocity U_{ref} was taken as the velocity at Z = 5H for each case, well above the immediate flow effects of the dike. It is seen from Figure 5-6 that at "full scale" conditions, the dike produces very little disturbance of the mean velocity profile at x = 7H. A good model would therefore be expected to exhibit similar behaviour.

Figure 5-7 shows the normalized mean velocity profiles for the two model dikes with and without the vane, compared to model-speed no-dike case. It is apparent that the model dike with the vane produces a close match in velocity profile to the no-dike case while the model dike without the vane yields a very poor match. This can also be seen by examining power fits to the above profiles as given in Table 5-3.

TABLE 5-3: VELOCITY PROFILE POWER LAW FITS BEHIND DIKES AT X = 7H

$$\frac{U}{U_{ref}} = \left[\frac{Z}{Z_{ref}}\right]^{n}$$

Condition	Dike	Height Range (cm)	n
"Full Scale" $Re_{\theta} = 1.3 \times 10^5$	Large (no vane)	0-10 10-50	0.094 0.240
	No Dike	0-10 10-50	0.102 0.230
Model $Re_{\theta} = 1.1 \times 10^4$	Large (no vane)	0-20 20-40	- 0.33
	Large (with vane)	0-15 15-40	0.205 0.300
	No Dike	0-20 20-80	0.182 0.309

The model dike with vane and the model no-dike case match closely in power law as is the case in "full scale", while the model dike case without the vane does not yield to a power law fit at all, being strongly linear in velocity with height up to about two dike heights.

In Figure 5-8 the vertical turbulence profiles for the "full scale" and two model cases are plotted for comparison. The turbulent disturbance parameter used is:

$$\frac{\Delta i_u}{i_u} = \frac{i_u(\text{with dike}) - i_u(\text{without dike})}{i_u(\text{without dike})}$$

This parameter is the fractional increase in intensity due to the dike wake, or in other words, the amount of turbulence added to the flow by the dike. One would expect this ratio to be closely matched to full scale values by a good model. Figure 5-8 shows that the model dike with vane does produce a close match to the "full scale" case while the model dike without the vane adds far too much turbulence to the lower levels of the flow, as would be expected from the measured recirculation zones produced by this model.

Summary

The mismatch in Reynolds number between model and full scale gives model dikes with grossly exaggerated recirculation zones. The use of a deflector vane mounted on the model dike crests corrects this problem, producing a dike flow which is a close match to expected full scale in downstream mean velocity and turbulence profiles. The model dike with vane can be used to accurately simulate the effects of dikes on atmospheric disperson.
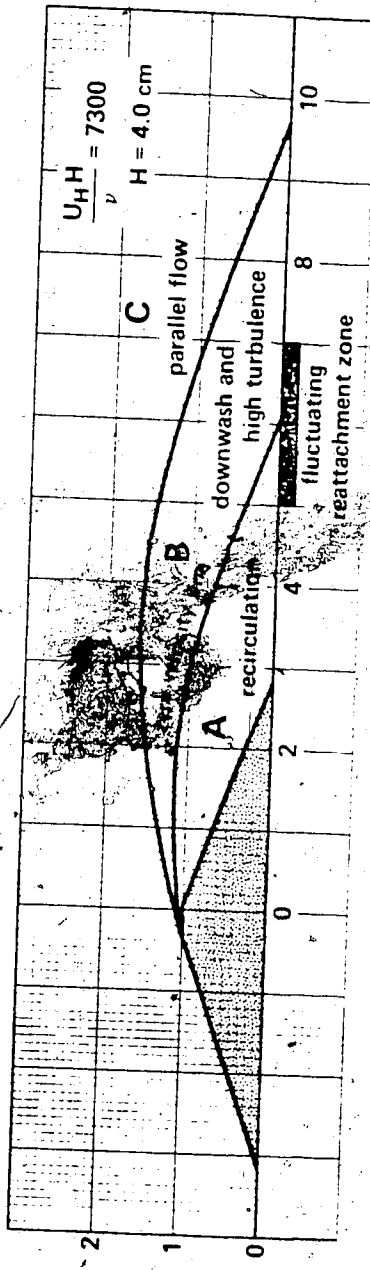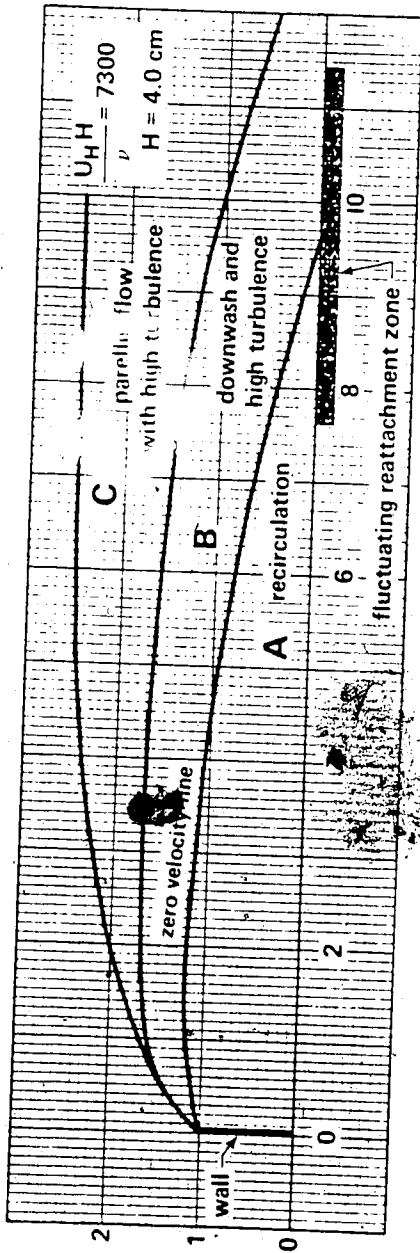
FIGURE 5-1: FLOW SEPARATION REGIONS OBSERVED IN A WATER CHANNEL [FROM WILSON, WINKEL AND NEIMAN (1979)]
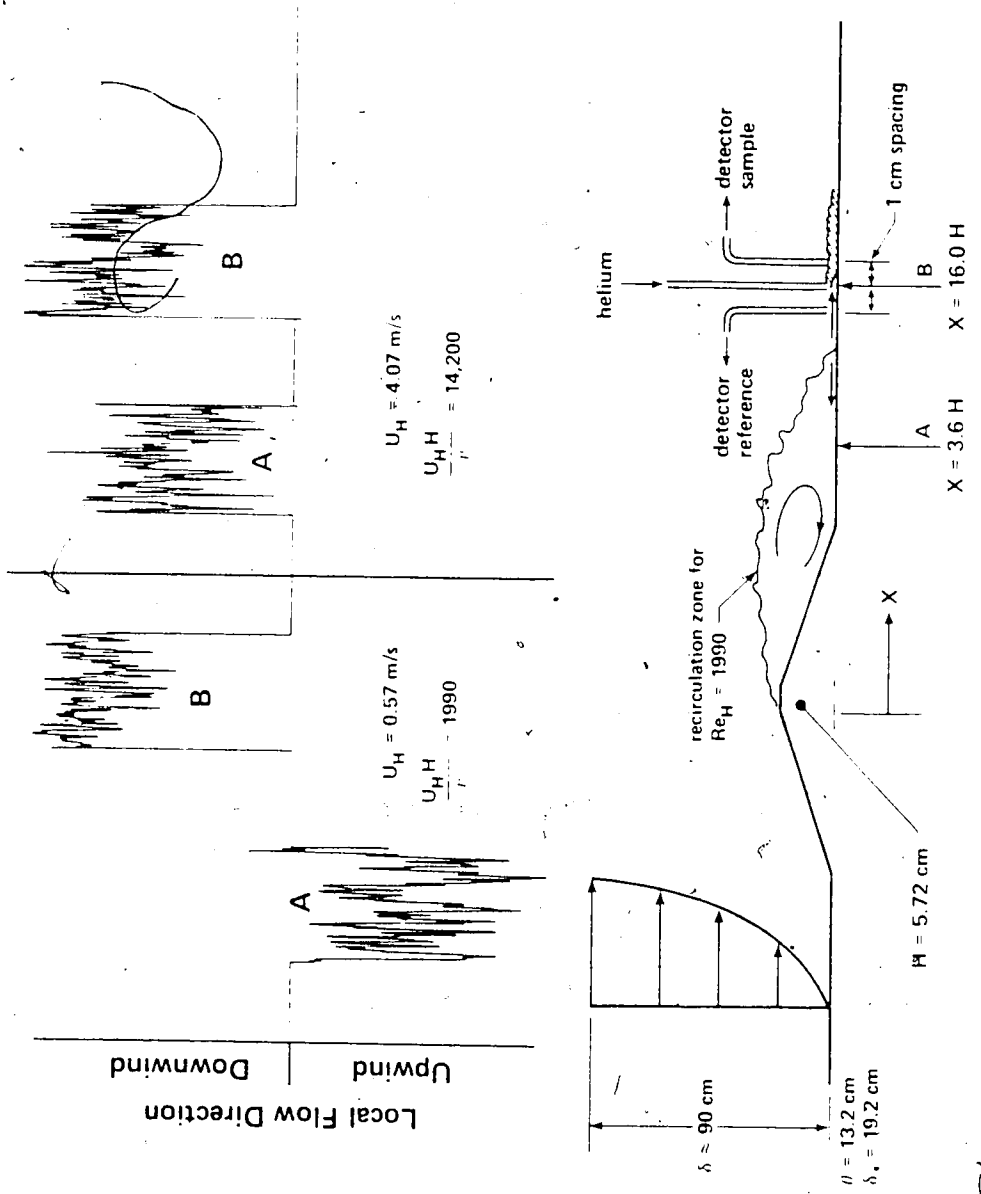
FIGURE 5-2: MEASUREMENT OF REATTACHMENT LENGTH WITH THE HELIUM FLOW DIRECTION DETECTOR [FROM WILSON, WINKEL AND NEIMAN (1979)]
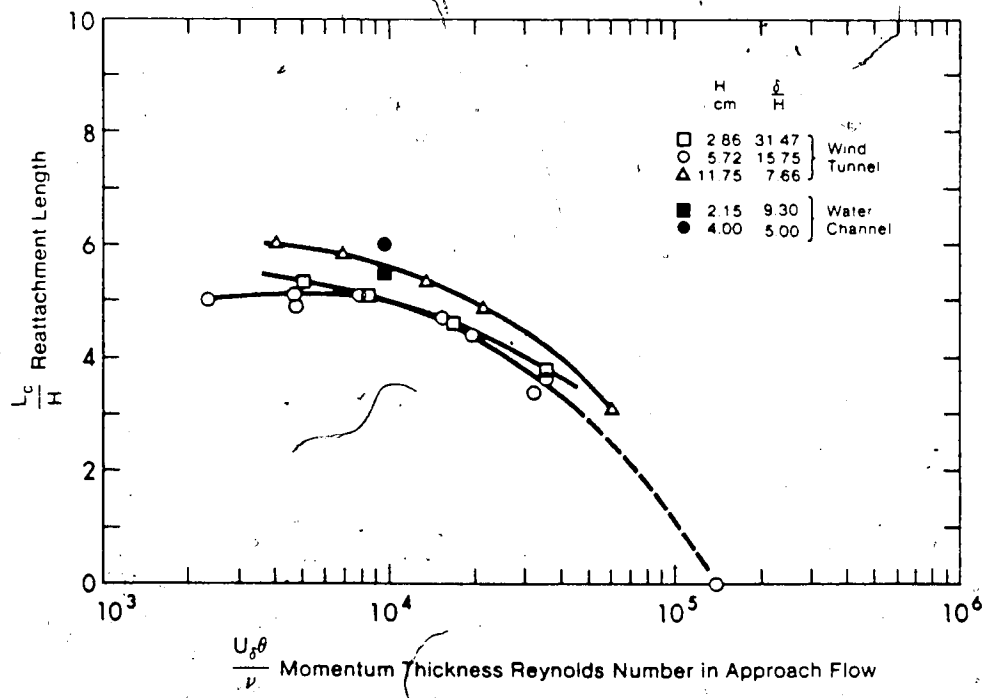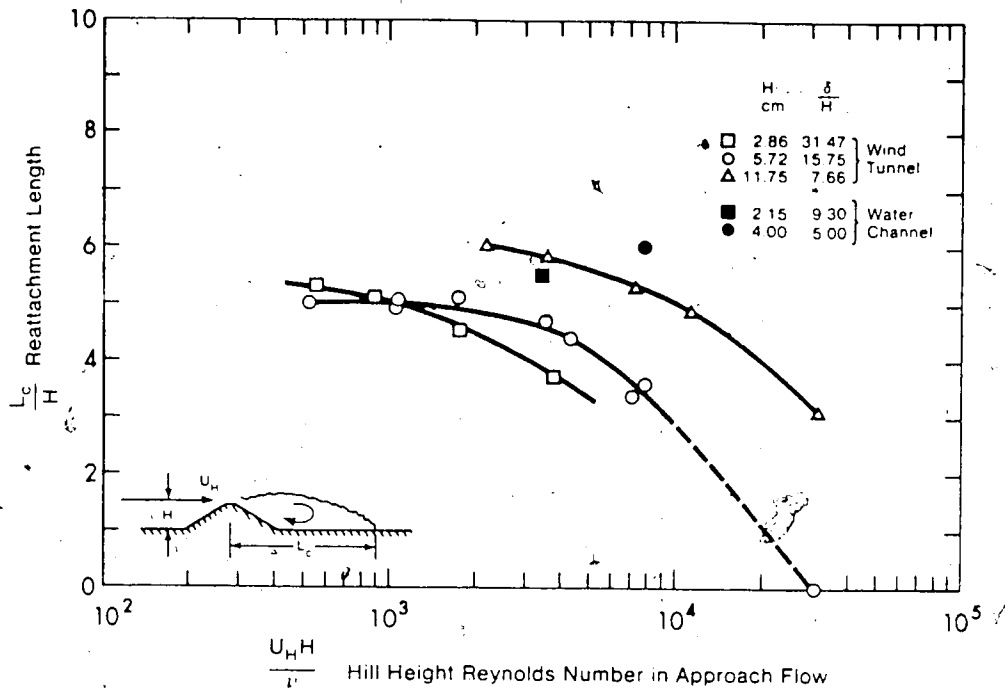
FIGURE 5-3: REYNOLDS NUMBER EFFECTS ON FLOW REATTACHMENT BEHIND MODEL DIKES [FROM WILSON, WINKEL AND NEIMAN (1979)]

81
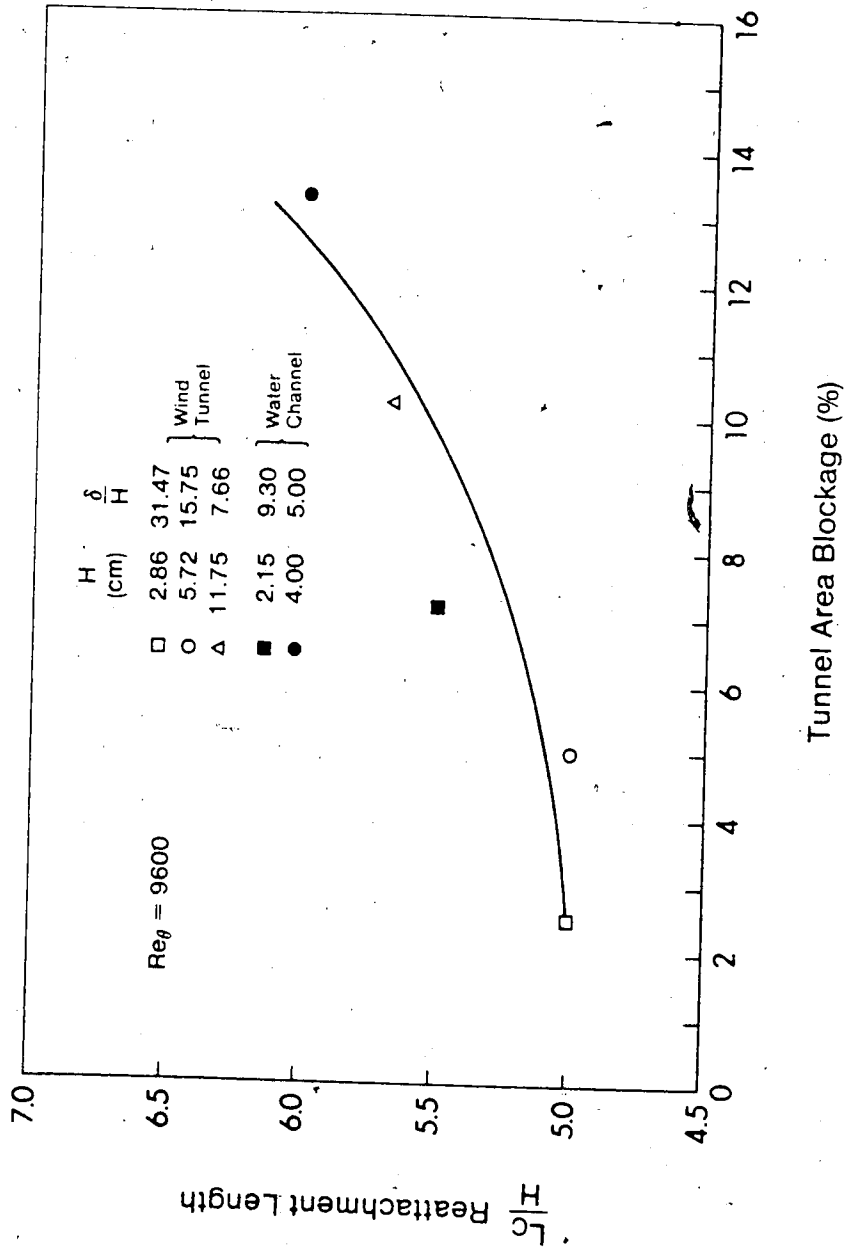
FIGURE 5-4: TUNNEL BLOCKAGE EFFECTS ON REATTACHMENT LENGTHS BEHIND MODEL DIKES

$Re_\theta = 2.7 \times 10^3$

$Re_\theta = 6.7 \times 10^3$

$Re_\theta = 5.4 \times 10^3$
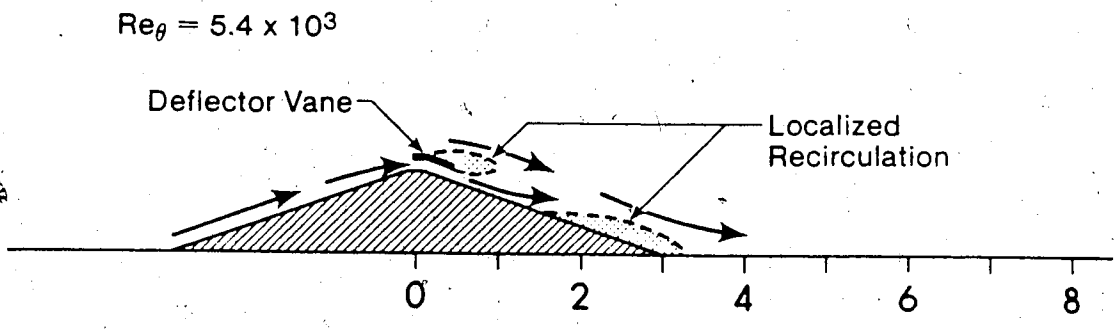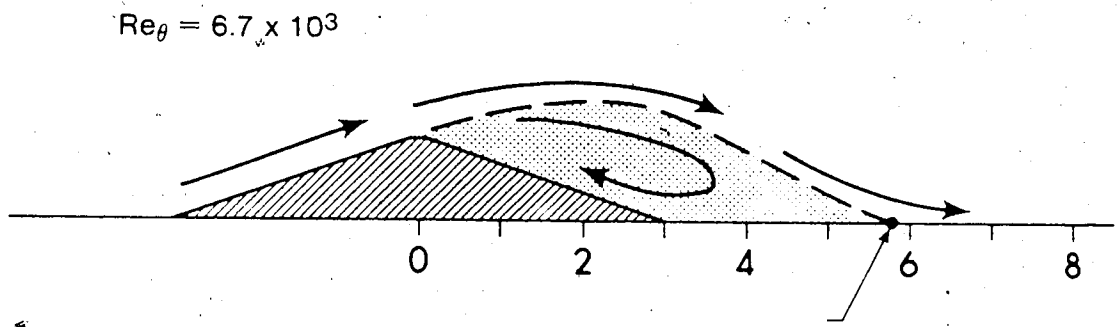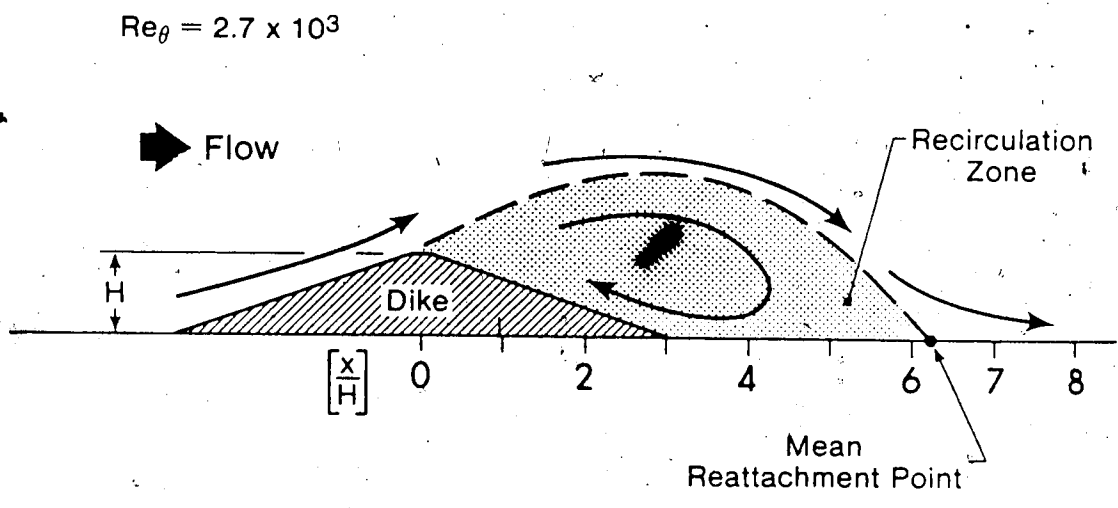
FIGURE 5-5: EFFECT OF THE DIKE DEFLECTOR VANE ON DIKE WAKE
FLOW FROM FLOW VISUALIZATION IN THE WIND TUNNEL

$Re_\theta = 1.3 \times 10^5$
$H = 11.75$ cm
$X = 7H$
$U_{ref} = U @ z = 5H$

Z Model Height Above Ground (cm)

No Dike
Run LT-016
$U_{ref} = 13.29$ m/s

Dike Height

Dike, No Vane
Run LT-015
$U_{ref} = 13.11$ m/s

$\dfrac{U}{U_{ref}}$ Normalized Mean Velocity
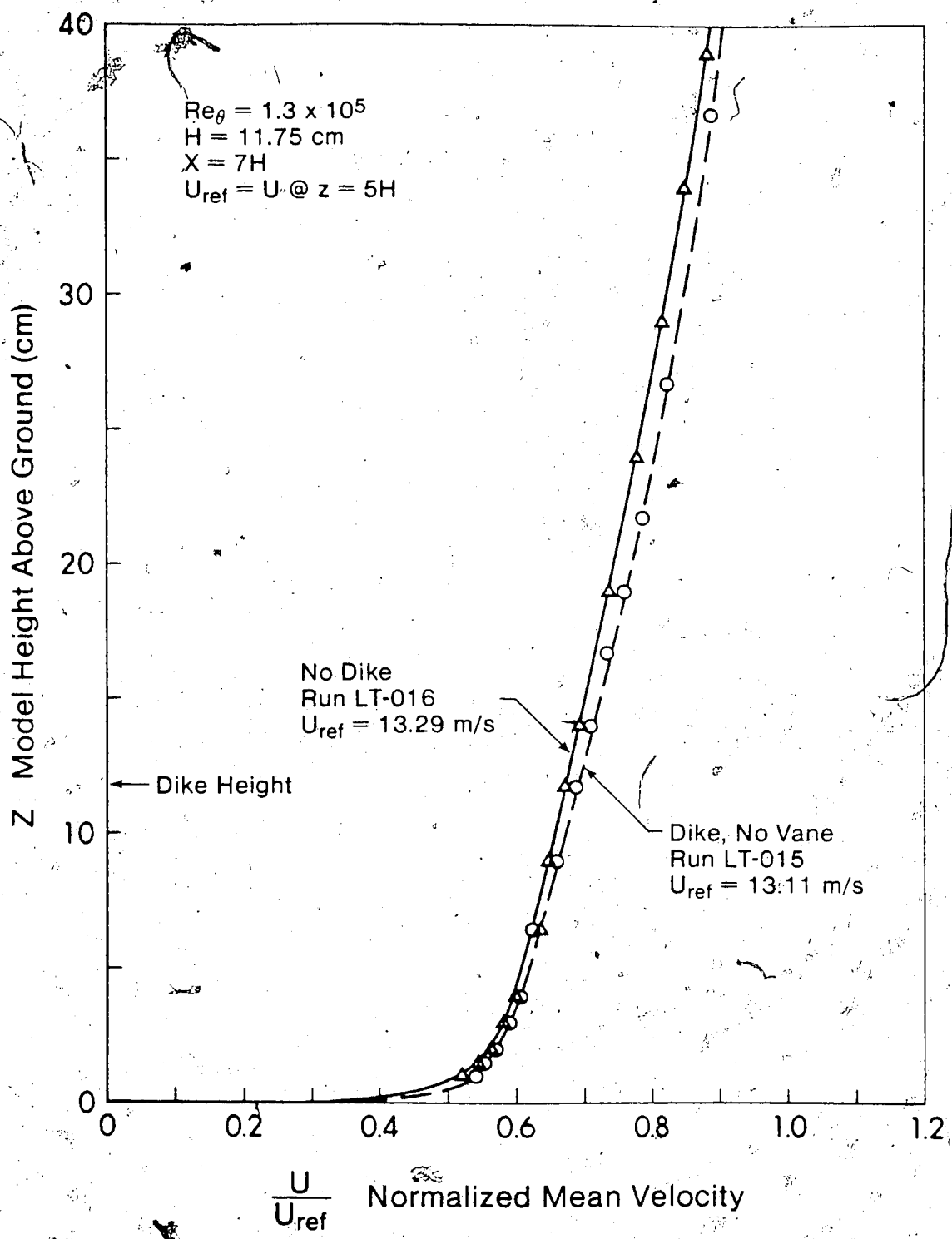
FIGURE 5-6: VERTICAL MEAN VELOCITY PROFILES BEHIND A MODEL DIKE
AT "FULL SCALE" CONDITIONS
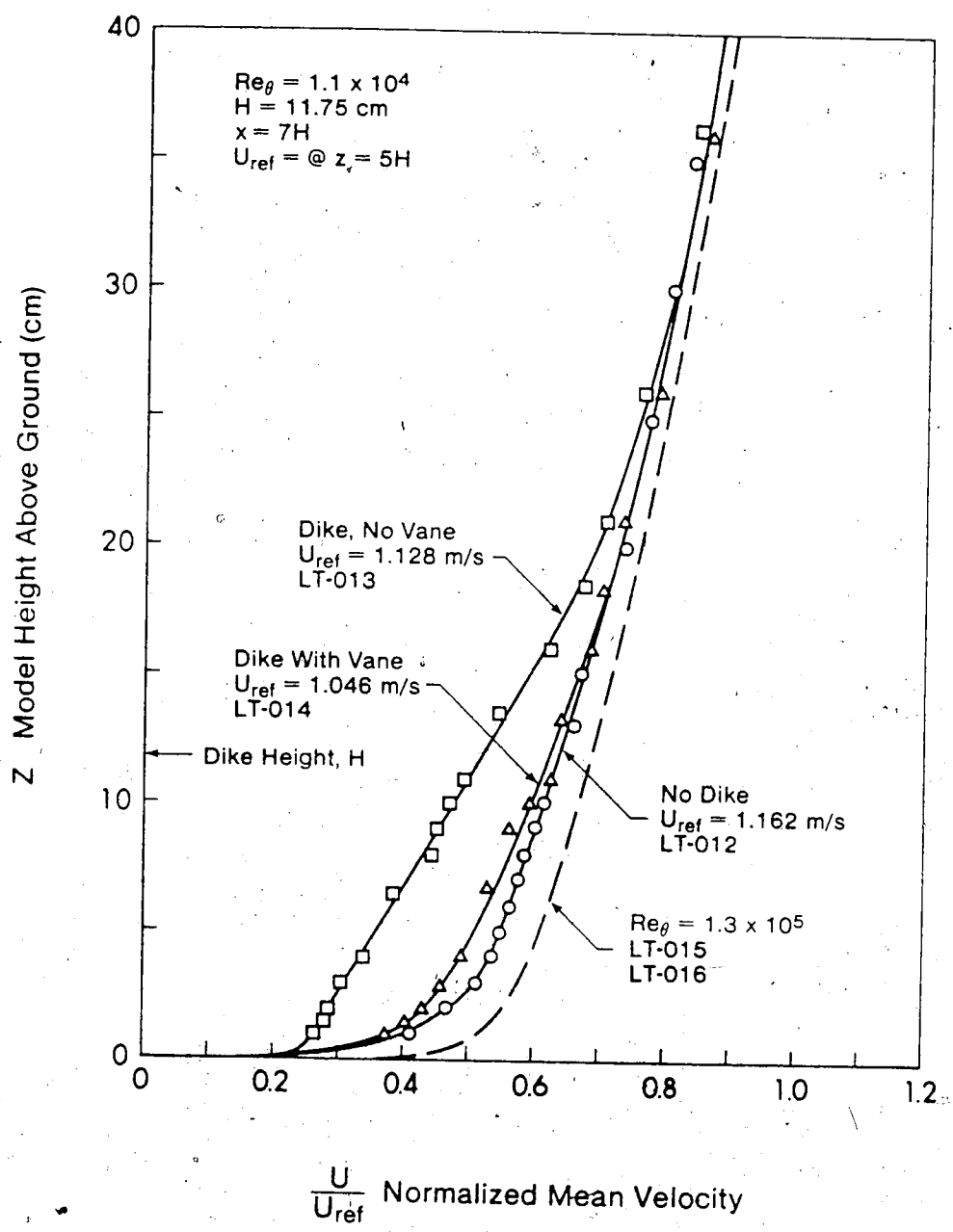
FIGURE 5-7: VERTICAL MEAN VELOCITY PROFILES BEHIND MODEL DIKES AT TYPICAL MODEL CONDITIONS
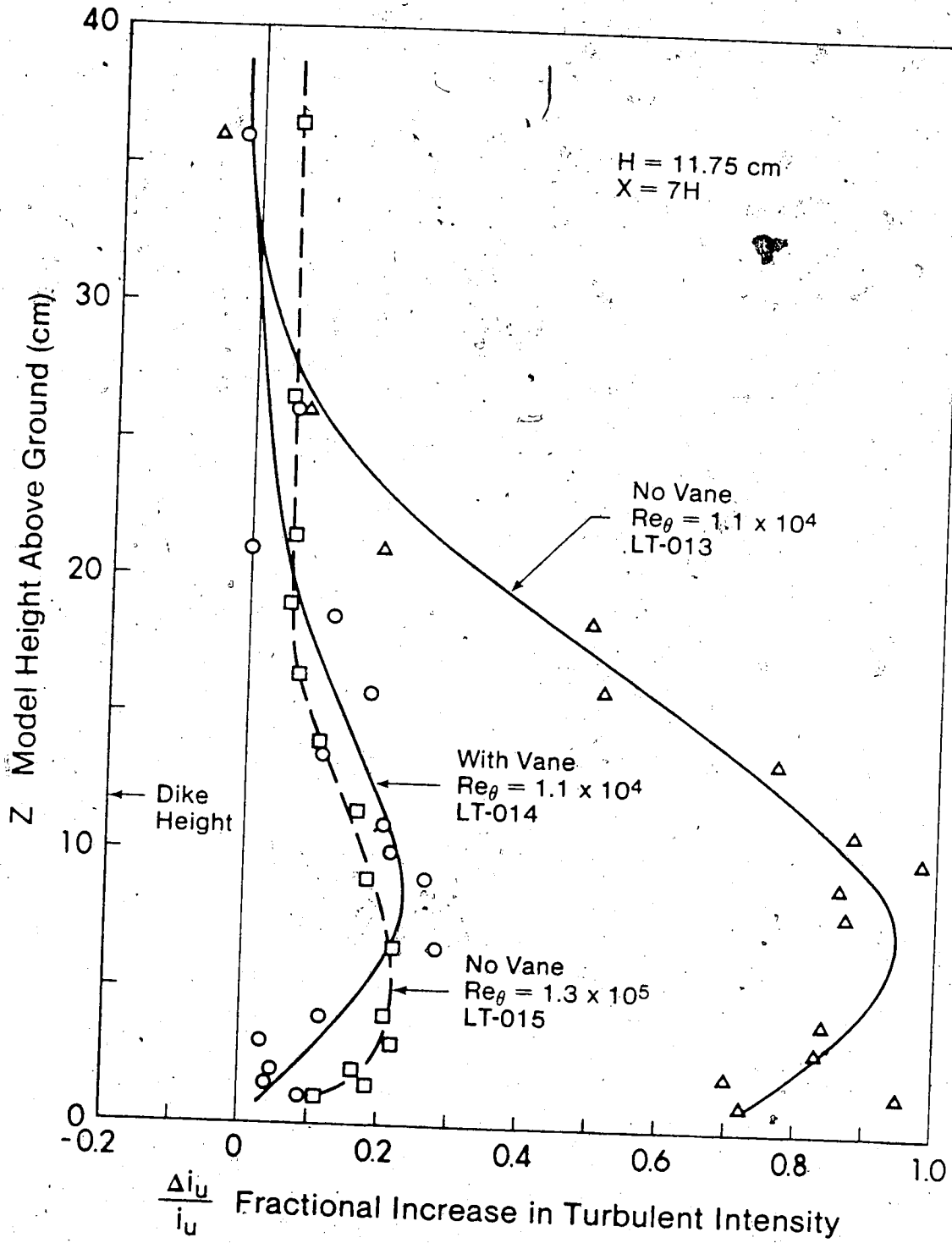
FIGURE 5-8:   VERTICAL PROFILES OF DIKE DISTURBANCE ON TURBULENT INTENSITY BEHIND MODEL DIKES

CHAPTER VI

INTERACTION OF DIKES WITH STACK PLUMES

Introduction

In this chapter the interaction between dike wakes and the disperson of stack plumes will be investigated by examining the effects of dikes on ground-level concentrations (GLC). Increases in GLC due to any factor are of prime interest to the stack designer because of the emphasis on maximum-allowable GLC levels in air pollution legislation. A simple semi-empirical theory will be developed for estimating dike effects on GLC values.

Experimental Procedure

Profiles of GLC were taken along a straight line downwind of the model stack shown in Figure 2-2. Various dike sizes and configurations, including dikes placed upstream and downstream of the stack were tested, as summarized in Table 6-1. The dikes were always oriented perpendicular to the flow and tested with the dike flow deflector vane described in Chapter V. Plume models A and B from Table 2-1 were used, where model A had a laminar stack gas and model B had a turbulent stack gas.

All GLC readings were obtained with a moveable sample tube mounted 0.4 cm (3.2 m full scale) above ground level. Four consecutive samples were taken at each downwind position, for 100 seconds each.

During each sample, the average windspeed U_s was measured with a Kurz Model 435 anemometer mounted at stack height beside the stack at

TABLE 6-1: SUMMARY OF GROUND LEVEL CONCENTRATION MEASUREMENTS WITH PREDICTED MAXIMUM VALUES

Plume Model	Dike Height (cm)	Dike Position (152 cm from stack)	U_s (m/s)	x_{max} (cm)	$\left[\dfrac{\text{Max. GLC (with dike)}}{\text{Max. GLC (flat terrain)}}\right]^*$
A	Flat terrain	—	0.50	600	1
	5.72	Upstream	0.50	600	1.00
	5.72	Downstream	0.50	560	1.01
	11.75	Upstream	0.50	470	1.20
	11.75	Downstream	0.50	490	1.20
	Flat terrain	—	1.0	310	1
	5.72	Upstream	1.0	310	1.00
	5.72	Downstream	1.0	310	1.03
	11.75	Upstream	1.0	250	1.20
	11.75	Downstream	1.0	300	1.12
B	Flat terrain	—	0.45	600	1
	5.72	Downstream	0.45	560	1.01
	Flat terrain	—	0.90	310	1
	11.75	Upstream	0.90	250	1.20

*From predicted values by (6-8)

x = 0, y = 30 cm. From these readings, a correction was made to each 100 second measurement for small deviations in mean flow velocity about the desired test value (see Appendix A). This correction was at most about 10%, for cumulative 400 second averages.

Limitations of the Study

The results of this study were limited by two factors:

First, the tunnel test section downwind of the stack was not long enough to locate maximum GLC values for all the plumes tested. This was particularly true of the two low-speed cases for plume models A and B, where measured concentrations rose to only about half of the maximum GLC at the end of the test section, as shown in Figure 6-1. For the high speed cases of these models, the position, x_{max}, of maximum GLC was found to be near the end of the test section.

As will be shown later, the lack of far downstream data only allowed the use of a simple model for dike effects.

The second limitation of the study involved the fact that the data for plume model A was inherently less useful than the data for plume model B. This was because during all model A runs, a cloth filter was installed across the end of the tunnel test section to help to steady the tunnel velocity. Unfortunately, the filter was later found to alter mean flow patterns in the tunnel so that the plume gradually drifted toward one side of the tunnel, as it passed through the test section.

Because GLC measurements were taken along the tunnel center-line (assuming no lateral shift) they were lower than the values along the plume axis. This was investigated by finding the shifted maximum GLC line by measuring lateral profiles and taking one GLC

profile down this line for each of the two velocities with flat terrain. By comparison with the corresponding flat terrain profiles down the tunnel centerline, there was no appreciable difference at U_s = 0.5 m/sec, but a significant (20-50%) difference, increasing with x, for the profiles at U_s = 1.0 m/sec. The measured ratios of GLC between the maximum and tunnel centerline values from this test were used to correct all 1 m/sec model A data.

The result of the above was that while model B data could be used to explore all aspects of absolute-value prediction of GLC with and without dike effects, the model A data was uncertain in an absolute sense and was limited only to the examination of dike effects relative to the flat terrain case.

Gaussian Model for Plume Dispersion

The Gaussian plume model was found to be very useful in predicting GLC values. Numerous investigations, such as the full scale studies of Weil and Jepsen (1977) and laboratory measurements by Wilson (1977), have shown that the statistical normal or Gaussian distribution is a close model to measured concentration distributions produced by turbulent diffusion. Applied to the case of a smokestack in an atmospheric boundary layer, the Gaussian solution for plume mass concentration χ is:

$$\chi(x,y,z,h) = \frac{\overset{\bullet}{m}}{2\pi U \sigma_y \sigma_z} \exp\left[-\frac{1}{2}\left(\frac{y}{\sigma_y}\right)^2\right] \left\{ \exp\left[-\frac{1}{2}\left(\frac{z-h}{\sigma_z^2}\right)^2\right] + \exp\left[-\frac{1}{2}\left(\frac{z+h}{\sigma_z}\right)^2\right] \right\} \cdot \quad (6\text{-}1)$$
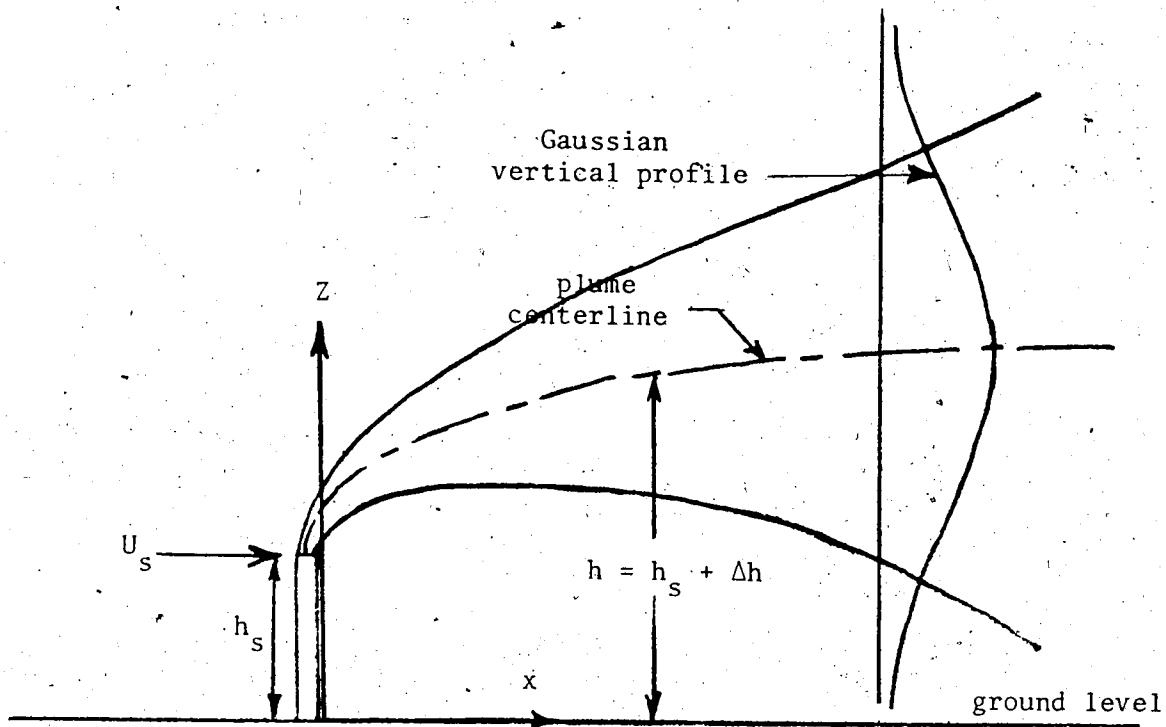
In the model, $\dot{m}$ is the mass flow rate of contaminant from the stack and σ_y and σ_z are the standard deviations of y and z direction concentration profiles, the "plume spreads".

Beneath the plume centerline at ground level $(z=y=0)$, $(6-1)$ reduces to:

$$\chi_o = \frac{\dot{m}}{\pi\sigma_y\sigma_z U} \; \exp\left[\frac{-h^2}{2\sigma_z^2}\right] \tag{6-2}$$

Using $\dot{m} = \chi_s Q$ where Q is the total stack volume flow rate, and specializing to the case of isothermal, isobaric conditions between stack and atmosphere, such as exist for the wind tunnel model, $(6-2)$ may be expressed as a ratio of volume concentrations:

$$\frac{C_o}{C_s} = \frac{Q}{\pi\sigma_y\sigma_z U} \; \exp\left[\frac{-h^2}{2\sigma_z^2}\right] \tag{6-3}$$

To predict GLC, the plume height h and the plume spreads σ_y and σ_z must be specified with downwind distance.

In this study, the measured average value of windspeed U_s was used with (6-3). Turner (1970) suggests that the integrated mean value U in the plume layer should be used, which is not much different than U_s here.

Plume Spread

Lateral and vertical plume spreads for the flat terrain cases of plume model B were obtained by fitting Gaussian distributions to measured lateral and vertical concentration profiles. For the vertical profiles, the fits were based only on the data below the plume center-line at h. Vertical plume spreads defined in this way should be more relevant for GLC prediction than full-profile fits. An example of a fitted vertical profile is shown in Figure 6-2. It can be seen that the lower half of the profile was well-fitted by σ_z(lower) = 10.5 cm at the expense of a slightly poorer fit for the top half. The fit shown based on the entire profile, with σ_z = 9.4 cm, was noticeably different in this case, although for most profiles, it was found that the choice of σ_z fitted to lower-half or full profiles made very little difference to GLC prediction.

Because it was necessary to interpolate and extrapolate spread values for GLC prediction, a smoothed functional form was required. Full scale dispersion studies such as the Brookhaven study, Singer and Smith (1966), have shown that for a given atmospheric condition, spreads of a non-buoyant contaminant in a given direction are well fitted by a single power law, $\sigma = ax^b$. To reduce measured plume spreads, σ (total),

which contain the effects of buoyancy-generated spread to their corres-
ponding values in non-buoyant form, σ(non-buoyant), Winkel (1979)
suggests the use of the equation

$$\sigma^2(total) = \sigma^2(non\text{-}buoyant) + \sigma^2(correction) \qquad (6\text{-}4)$$

where the latter term, representing buoyancy-induced spread, may be
estimated by the following:

$$\sigma^2(correction) = C_1 \beta_2^2 \, \Delta h^2 \qquad (6\text{-}5)$$

In this correction term, β_2 and Δh are those values which would apply
to the rise of the plume in a laminar cross-flow, which in turn is re-
lated to buoyancy-induced spread. The constant C_1 was found by Winkel
(1979) to be about 1/9. From rise measurements of plume model B in a
laminar cross-flow, $\beta_2 = 0.87$, and this value was used for buoyancy
corrections throughout the study.

Using (6-4) and (6-5), the measured σ_y and σ_z(lower) values
for plume model B were buoyancy corrected to σ(non-buoyant) form. In
Figures 6-3 and 6-4, power law fits to this data are plotted and compared
to 800:1 reduced Brookhaven C (neutral stability) power laws.

To obtain plume spread values for any downwind position, the
fitted power laws from plume model B were corrected back to model condi-
tions using (6-4) and (6-5). Thus, the magnitude of the buoyancy
correction was not very important; the advantage of using the correction
was to obtain a universal functional form for spread.

Predicting GLC for the Flat Terrain Case

Using (6-3), profiles of C_o/C_s were predicted for the two tested

windspeeds for plume model B, as plotted in Figure 6-5. Rise values used in the calculations were obtained from (4-11) to match the actual measured rise. For U_s = 0.45m/s, the combined-rise model shown in Figure 4-1 was used, with β_2 = 1.4. The final rise was set at Δh_{final} = 16.37 cm at x_{final} = $2200L_B$. For U_s = 1m/sec, Δh = 0 was used for all x due to stack downwash.

Several important conclusions may be drawn from Figure 6-5:

(1) The difference in GLC prediction between using σ_z from whole-profile fits or σ_z''(lower) is negligible. Predicted values from whole-profile Gaussian fits are very close to those using σ_z(lower) = 0.271 $x^{0.70}$.

(2) The Gaussian model for plume dispersion appears to be valid under a wide range of conditions, from the case with severe downwash to those with large amounts of plume rise. The vertical and lateral measured plume profiles used to obtain plume rise and spread were well represented by Gaussian distributions, as seen in Figure 6-2: The good agreement of the measured GLC profiles in Figure 6-5 to the Gaussian predictions also supports the use of the Gaussian model because the plume rise and spread values used in the predictions were not derived in any way from ground level data.

Figure 6-5 also displays some inadequacies of the Gaussian model for GLC prediction. For example, there is a kink in the predicted curve for U_s = 0.45 m/s near x = 225 cm, and the curve is seen to rise more sharply than the data beyond that point. The scatter in the data, which was typically about ± 0.01 for (C_o/C_s) x 1000, can not explain this discrepancy. Actually, the change in character of the prediction was caused by the final rise model, where x_{final}=$2200L_B$

(223 cm). Final rise was observed for this plume, as seen in Figure 4-1, but the data in Figure 6-5 behaved as if the plume did not level off. Using the Gaussian model, plume centerline changes were assumed to be instantly reflected in values of GLC, however, the data was accurate enough to display the error in this assumption. There is probably a time delay for the edges of a plume to respond to centerline changes.

Predicted GLC curves for the plume model A flat terrain cases were also required. Because no rise data was available, and because the plume model A data was already limited to the investigation of relative effects of dikes, the predictions for these cases were fitted to the data, as shown in Figure 6-6, by the choice of an appropriate entrainment constant, β_2. The advantage of this was that when the flat terrain predictions were later corrected for dike effects and compared to data, the closeness of fit gave a direct indication of the accuracy of the dike correction. The closeness of GLC predictions to plume model A data are not a verification of the absolute accuracy of the Gaussian model, although the rise values used to obtain the fit for the flat terrain cases were very realistic: for the 1 m/sec case, z = 0 (all x) was used, and for the 0.5 m/sec case, (4-11) was used with final rise at x = 2200L$_B$ and β_2 = 1.22 (compared to β_2 = 1.4 for the turbulent stack gas in model B).

Correcting for Dike Effects

A model to correct for dike effects on GLC was obtained by taking the ratio between the expressions for predicted GLC, with and without a dike, using (6-3):

$$\frac{C_o(dike)}{C_o} = \frac{\sigma_y}{\sigma_y(dike)} \cdot \frac{\sigma_z}{\sigma_z(dike)} \cdot \exp\left[\frac{-h^2(dike)}{2\,\sigma_z^{\,2}(dike)} + \frac{h^2}{2\,\sigma_z^{\,2}}\right] \qquad (6\text{-}6)$$

In (6-6), the parameters C_o, σ_y, σ_z, and h are for flat terrain. Defining some "dike disturbance" parameters,

$$\eta = \frac{\sigma_z}{\sigma_z(dike)}$$

$$\varepsilon = \frac{\sigma_y}{\sigma_y(dike)}$$

$$\gamma = \frac{h(dike)}{h}$$

(6-6) becomes:

$$\frac{C_o(dike)}{C_o} = \varepsilon\eta \exp\left[\frac{-h^2}{2\sigma_z^{\,2}}\left(\gamma^2\eta^2 - 1\right)\right] \qquad (6\text{-}7)$$

With suitable models for η, ε, and γ, (6-7) would account for all possible dike disturbance effects in GLC prediction using the Gaussian model. However, in comparing the model to data, it was practical to allow only one of these parameters to vary, setting the others equal to unity (assuming no effect of dike) or equal to the varied parameter (assuming equal dike effect). A number of possibilities were examined, as summarized below:

(1) $\gamma = 1$, $\varepsilon = \eta$

Assigning dike effects equally to σ_y and σ_z while keeping plume

rise constant seemed physically reasonable but did not produce a workable correction. Equation (6-7) was unable to predict a large enough correction effect in many cases regardless of the η values chosen.

(2) $\epsilon = 1$, $\eta = 1$

Assigning dike effects to plume rise alone while keeping plume spread constant always produced a proper correction if γ was varied, because (6-7) is unbounded in $C_o(dike)/C_o$ as γ decreases from $\gamma = 1$. However, this model had the disadvantage of being physically unrealistic, considering that a constant height non-buoyant plume which would not be subject to correction could still be affected by a dike.

(3) $\epsilon = 1$, $\gamma = 1$

Assigning dike effects to σ_z alone while keeping σ_y and h constant was found to be both workable and physically reasonable. Extra turbulence induced by a dike wake would be expected to increase vertical spread and cause larger GLC values, which was consistent with the model and with measurements. Lateral plume spread would also be expected to be increased by dike-induced turbulence, which causes some loss of realism in the model, however, this did not cause it to be untenable as in (2) above.

With the use of $\epsilon = 1$ and $\gamma = 1$, (6-7) is:

$$\frac{C_o(dike)}{C_o} = \eta \exp \left[\frac{-h^2}{2\sigma_z^2} \left(\eta^2 - 1 \right) \right] \qquad (6-8)$$

A sketch of this function for a typical value of $\left[h^2/2\sigma_z^2 \right] = 1.1$ is shown below:

$$\frac{C_0(\text{dike})}{C_0}$$
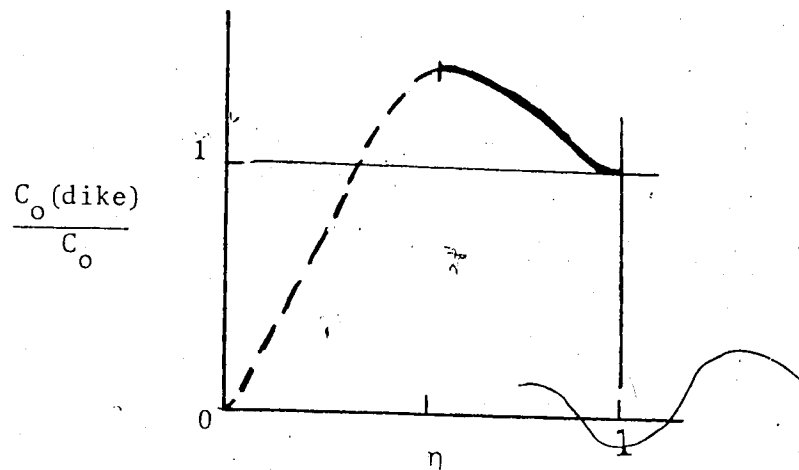
Only that part of the function (shown as a solid line) where $C_0(\text{dike})/C_0$ increases with decreasing η was physically realistic and used for the correction; the other part (shown as a dashed line) was extraneous. Note that there is a maximum correction possible by this model for a given $\left[h^2/2\sigma_z^2\right]$ value. Measured values of $C_0(\text{dike})/C_0$ were never found to exceed this maximum.

Using smoothed curves through all the measured GLC profiles, values of $C_0(\text{dike})/C_0$ were obtained at about nine regularly-spaced downwind positions for each case. Then, using (6-8), η was varied downwards from $\eta = 1$ until a match was obtained in $C_0(\text{dike})/C_0$ for each position. The final values of η required to match experimental measurements are shown as data points in Figure 6-7.

It was expected that η would be equal to unity (no dike effect) upstream of the dikes, and that its value would decrease downwind of the dikes and then return to unity at a certain number of dike heights downwind of the dikes where the dike wake turbulence had decayed to ambient levels. This behaviour was observed (with a great deal of scatter) for the medium (45.8 m full scale) dike data in Figure 6-7, with the

effect of the dike dying away at about 80 dike heights downstream. For the large (94 m full scale) dike the limitation of test section length did not allow this return to $\eta = 1$ far downstream to be observed, although the measured η values were consistent in form to those of the medium dike. The η values for the large dike indicated a much increased dike disturbance effect over the medium dike values.

The low values of $\eta \approx 0.7$ observed for two of the large dike cases in Figure 6-7 occurred as Equation 6-8 was approaching a maximum in $C_o(\text{dike})/C_o$. In this region, the correction is very insensitive to changes in η, and ignoring these deviations in the recommended line for η shown in Figure 6-7 does not produce large errors in predicting the dike correction.

A Model for Vertical Spread Ratio, η

Owing to the fairly rough and incomplete nature of the data for η, only a simple model was proposed to correlate the data and allow for the prediction of GLC with dikes. Straight line segments were used, which divided the model into five regions in $x_d = [x-x(\text{dike})]/H$ as given below and shown in Figure 6-7.

$$\eta = 1 \qquad\qquad x_d < -2.5$$

$$\eta = x_d \left[\frac{\eta_{low} - 1}{22.5} \right] + 1 + \frac{2.5}{22.5}\left(\eta_{low} - 1\right) \qquad -2.5 < x_d < 20$$

$$\eta = \eta_{low} \qquad\qquad 20 < x_d < 60$$

$$\eta = x_d \left[\frac{1 - \eta_{low}}{20} \right] + 4\eta_{low} - 3 \qquad 60 < x_d < 80$$

$$\eta = 1 \qquad\qquad x_d > 80$$

(6-9)

The minimum value of η, which defines the magnitude of the correction, is given by

$$\eta_{low} = 1 - 1.1 \left[\frac{H}{h_s}\right]^3 \qquad (6\text{-}10)$$

It is clear that from the data in Figure 6-7 that $(1 - \eta_{low})$ increases non-linearly with dike height, and it is also expected that the ratio of the dike height to the stack height would be of importance in a general correlation. Because only two dike heights and one stack height were tested, (6-10) is only a preliminary estimate in lieu of further data.

In (6-9), the extension of dike effects slightly upwind of the dike crest (2.5 dike heights) was to account for local streamline compression effects on GLC which were observed to increase GLC values directly above the dikes. This phenomenon was also observed by Wilson (1977) for flow over gentle hills.

Predicted GLC With Dikes

Equations (6-8), (6-9) and (6-10) were used to predict GLC values for all the cases tested in the study (see Table 6-1). These predictions are shown along with the measured values in Figures 6-8 through 6-12. In each case, the predicted curve for the flat terrain case is also shown.

A number of conclusions may be drawn from these predictions: (1) The correction model was successful, producing about the right amount of increase in GLC above the flat terrain prediction for all cases (considering that the data was used to obtain the model for η this is not too surprising). For the plume model A cases, this can be directly

seen from the good closeness of fit between the data and the predicted

curves with correction. For the 1 m/sec case of plume Model B shown

in Figure 6-12; the apparent overprediction in the dike correction was

due to the fact that the flat terrain prediction also overpredicted the

flat terrain data by about the same amount, as shown in Figure 6-5.

In Figure 6-12, a smoothed curve from data taken with all condi-

tions the same except the plant site model reversed is seen to follow

the data for U_s = 0.9 m/sec very closely. This indicates that the dike

was by far the dominant terrain feature and that results from this study

may be generalized to any typical plant site.

(2) Dike effects on GLC are definitely not linear with dike height.

The large dike is seen in Figures 6-8 through 6-12 to produce increases

in GLC over the flat terrain case about an order of magnitude greater

than those for the medium dike, which was about half the size. This

is accounted for in the model in Equation 6-10 where $(1 - \eta_{low})$ is

proportional to H^3.

Maximum Values of Ground Level Concentrations (GLC)

For all the cases tested, the GLC predictions from the Gaussian

plume model (6-8), with dike corrections (6-9) and (6-10) were carried

out as far downwind as necessary to determine the position, x_{max}, and

magnitude of the maximum value of GLC. These results are given in

Table 6-1 where the magnitude results are expressed as the ratio of

maximum GLC with the dike to the maximum GLC for the flat terrain case.

In Table 6-1 it is seen that the effect of the large dike was

to increase the maximum GLC value by about 20% in all cases, and also

cause that value to be reached about 20% closer to the stack compared

to the flat terrain case. The medium (45.8m full scale) dike was found

to have only at most a 3% effect on maximum GLC, with a negligible

effect on x_{max}.
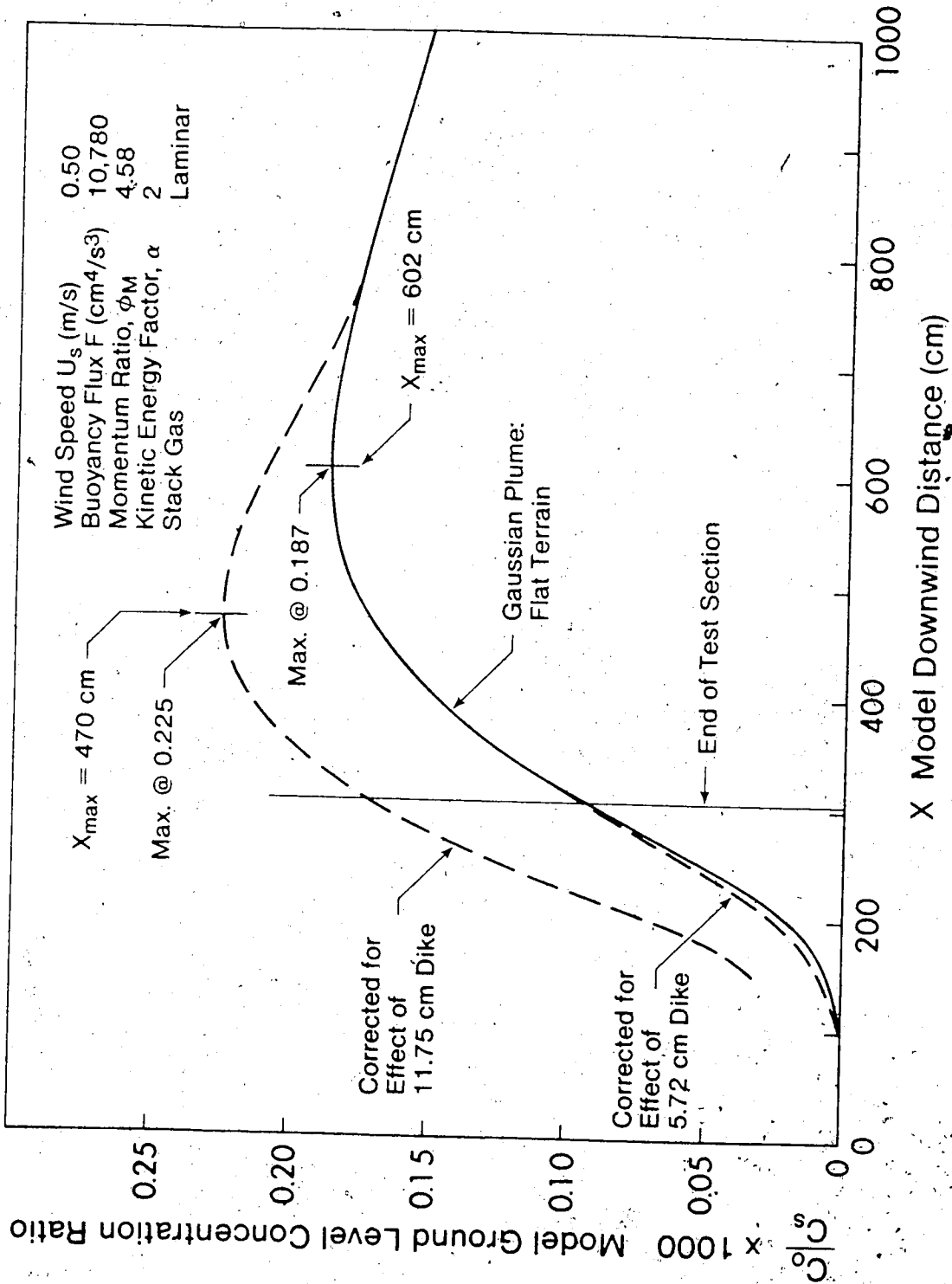
FIGURE 6-1: PREDICTED GLC FOR PLUME MODEL A WITH FLAT TERRAIN AND UPWIND DIKES

Wind Speed U_S (m/s)   0.45
Buoyancy Flux F (cm^4/s^3)   9219
Momentum Ratio, ϕ_M 2.57
Kinetic Energy Factor, α 1.27
Stack Gas   Turbulent

x = 150 cm

Gaussian Fit to
Entire Profile
σ_z = 9.4 cm

Gaussian Fit to Lower
Half of Profile
σ_z (lower) = 10.5 cm

Z   MODEL HEIGHT ABOVE GROUND (CM)

C   MODEL CONCENTRATION (PPTH)
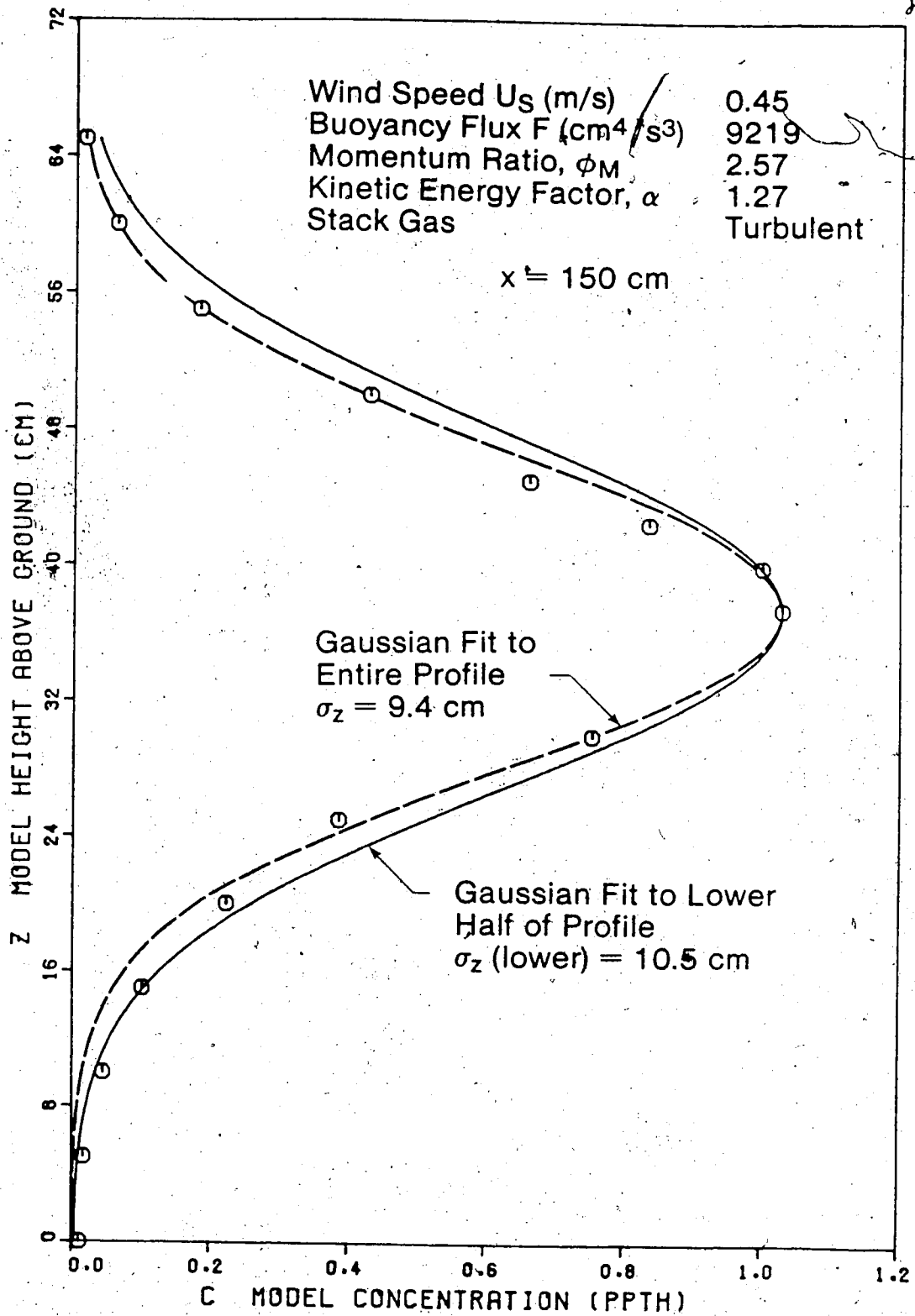
FIGURE 6-2:   GAUSSIAN FITS TO A VERTICAL CONCENTRATION PROFILE
FROM PLUME MODEL B AT x = 150 cm
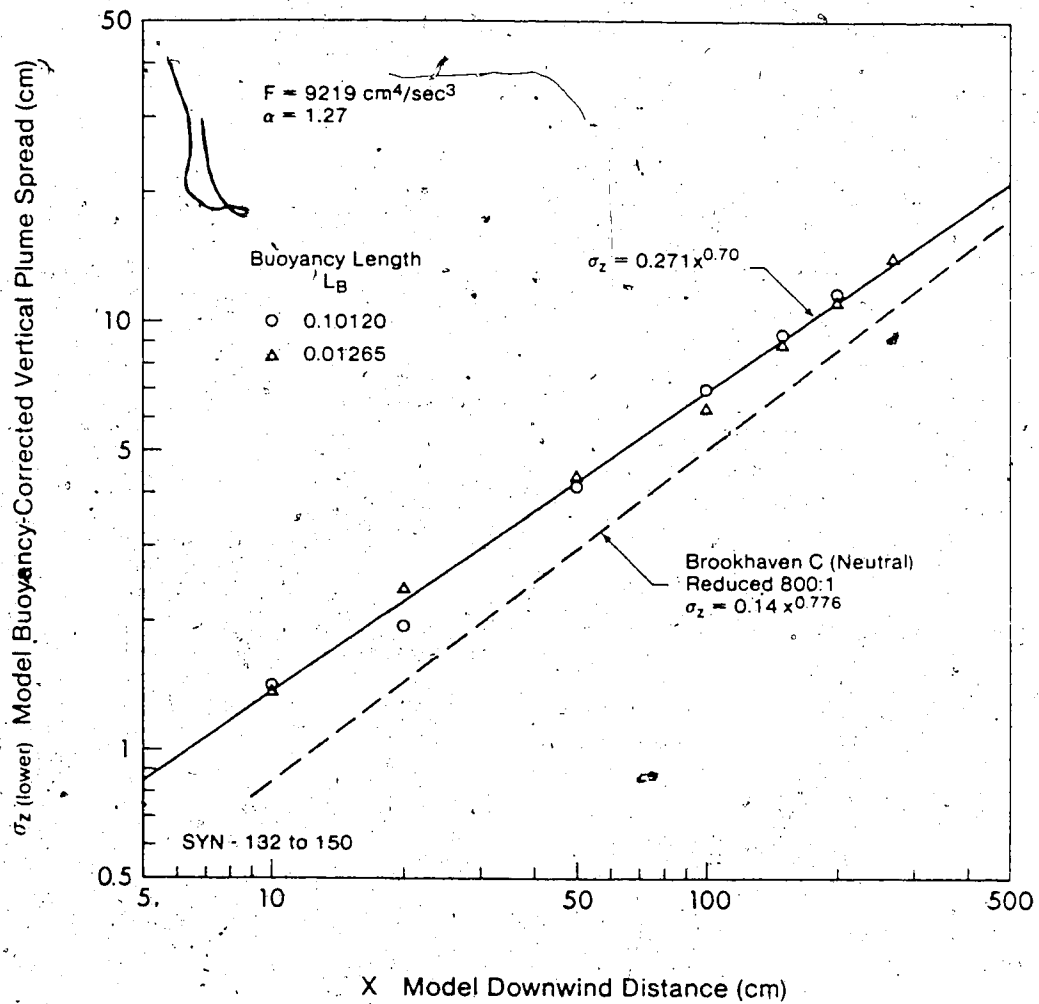
FIGURE 6-3:   BUOYANCY-CORRECTED VERTICAL SPREADS FROM BEST-FIT
TO LOWER HALF OF CONCENTRATION PROFILES FOR PLUME
MODEL B

FIGURE 6-4: BUOYANCY-CORRECTED LATERAL SPREADS FOR PLUME MODEL B

Wind Speed U_S (m/s) 0.45
Buoyancy Flux F (cm^4/s^3) 9219
Momentum Ratio, ϕ_M 2.57
Kinetic Energy Factor, α 1.27
Stack Gas Turbulent

Flat Terrain – No Dike

Gaussian Plume
Flat Terrain
Using σ_z (lower)

100 sec. samples
400 sec. (3 hr.) averages

Gaussian Plume
Flat Terrain
Using σ_z
From Whole Profile Fits

$\frac{C}{C_s}$ × 1000, Model Ground Level to Stack Concentration Ratio

X, Model Scale Downwind Distance from Stack, cm

X, Full Scale Downwind Distance from Stack, meters

Wind Speed U_S (m/s) 0.90
Buoyancy Flux F (cm^4/s^3) 9219
Momentum Ratio, ϕ_M 0.643
Kinetic Energy Factor, α 1.27
Stack Gas Turbulent

Flat Terrain – No Dike

Gaussian Plume:
Flat Terrain
Using σ_z (lower)

100 sec samples
400 sec. (3 hr.) averages

Gaussian Plume:
Flat Terrain
Using σ_z from
Whole-Profile Fits

$\frac{C}{C_s}$ × 1000, Model Ground Level to Stack Concentration Ratio

X, Model Scale Downwind Distance from Stack, cm

X, Full Scale Downwind Distance from Stack, meters

FIGURE 6-5: PREDICTED AND MEASURED GLC FOR PLUME MODEL B WITH FLAT TERRAIN

Upper panel:

Flat Terrain — No Dike

Wind Speed U_S (m/s)   0.50
Buoyancy Flux F (cm⁴/s³)   10,780
Momentum Ratio, ϕ_M 4.58
Kinetic Energy Factor, α 2
Stack Gas   Laminar

Gaussian Plume:
Flat Terrain

$\frac{C}{C_s}$ x 1000, Model Ground Level to Stack Concentration Ratio

X, Model Scale Downwind Distance from Stack, cm

X, Full Scale Downwind Distance from Stack, meters

Lower panel:

Flat Terrain — No Dike

Wind Speed U_S (m/s)   1.0
Buoyancy Flux F (cm⁴/s³)   10,780
Momentum Ratio, ϕ_M 1.14
Kinetic Energy Factor, α 2
Stack Gas   Laminar

Gaussian Plume:
Flat Terrain

$\frac{C}{C_s}$ x 1000, Model Ground Level to Stack Concentration Ratio

X, Model Scale Downwind Distance from Stack, cm

X, Full Scale Downwind Distance from Stack, meters
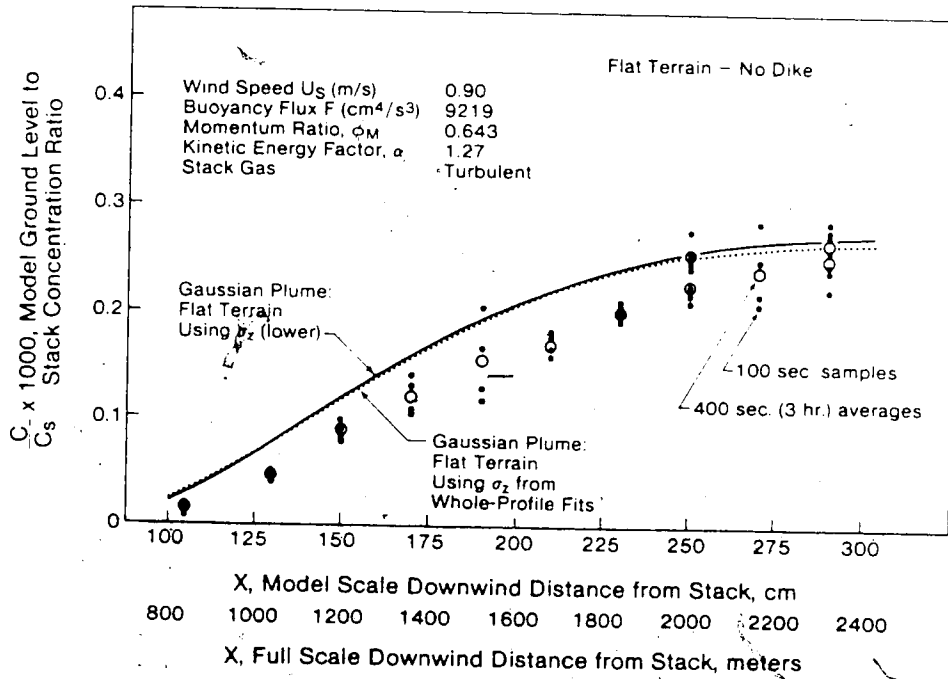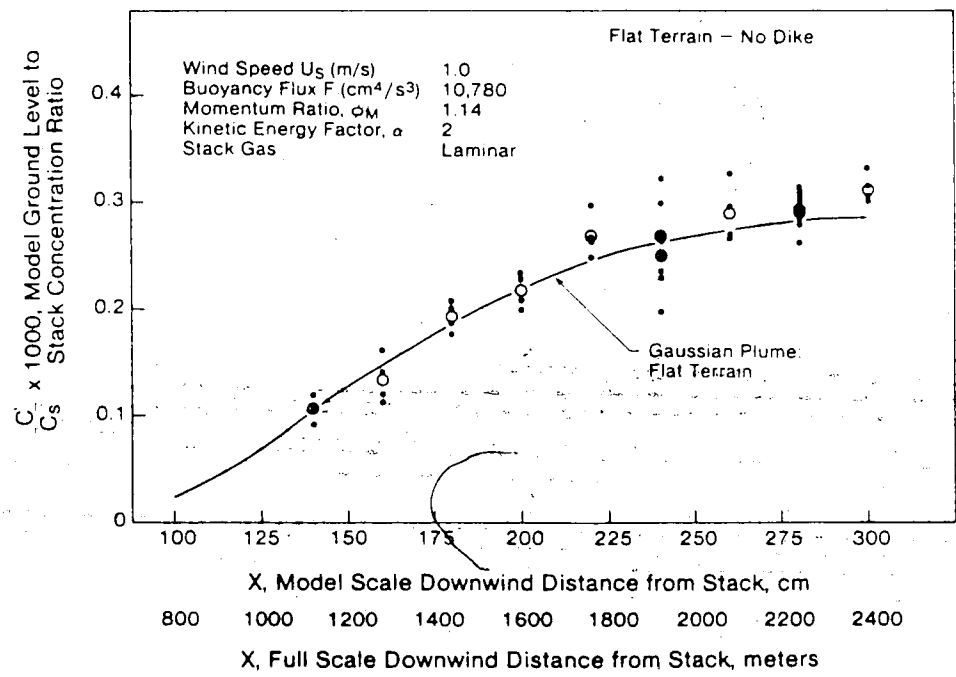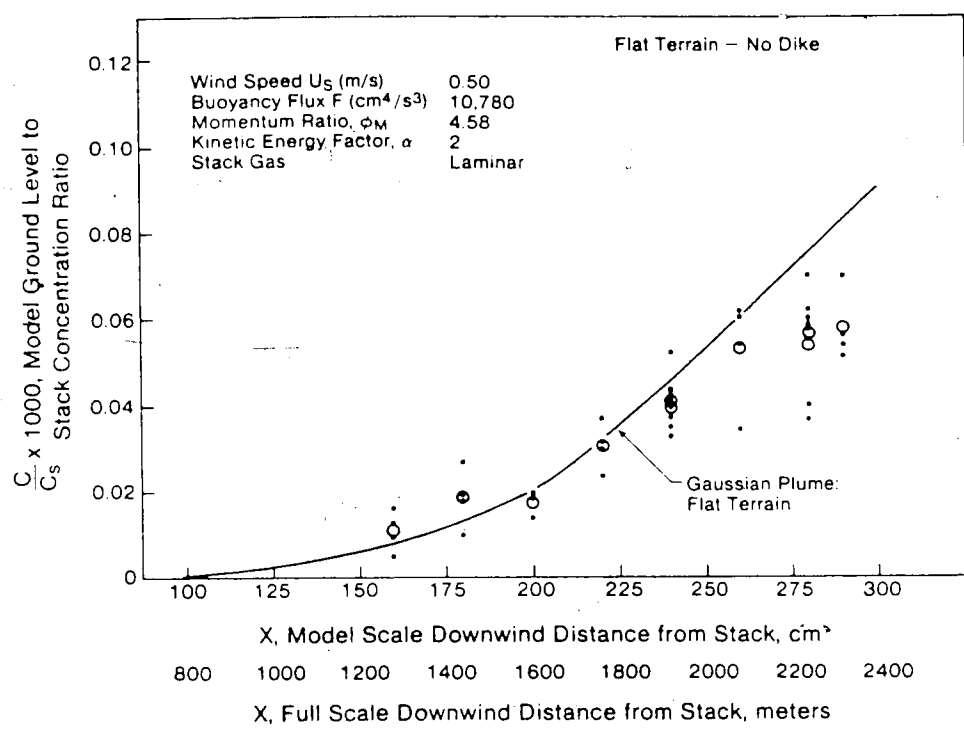
FIGURE 6-6:   PREDICTED AND MEASURED GLC FOR PLUME MODEL A WITH FLAT TERRAIN
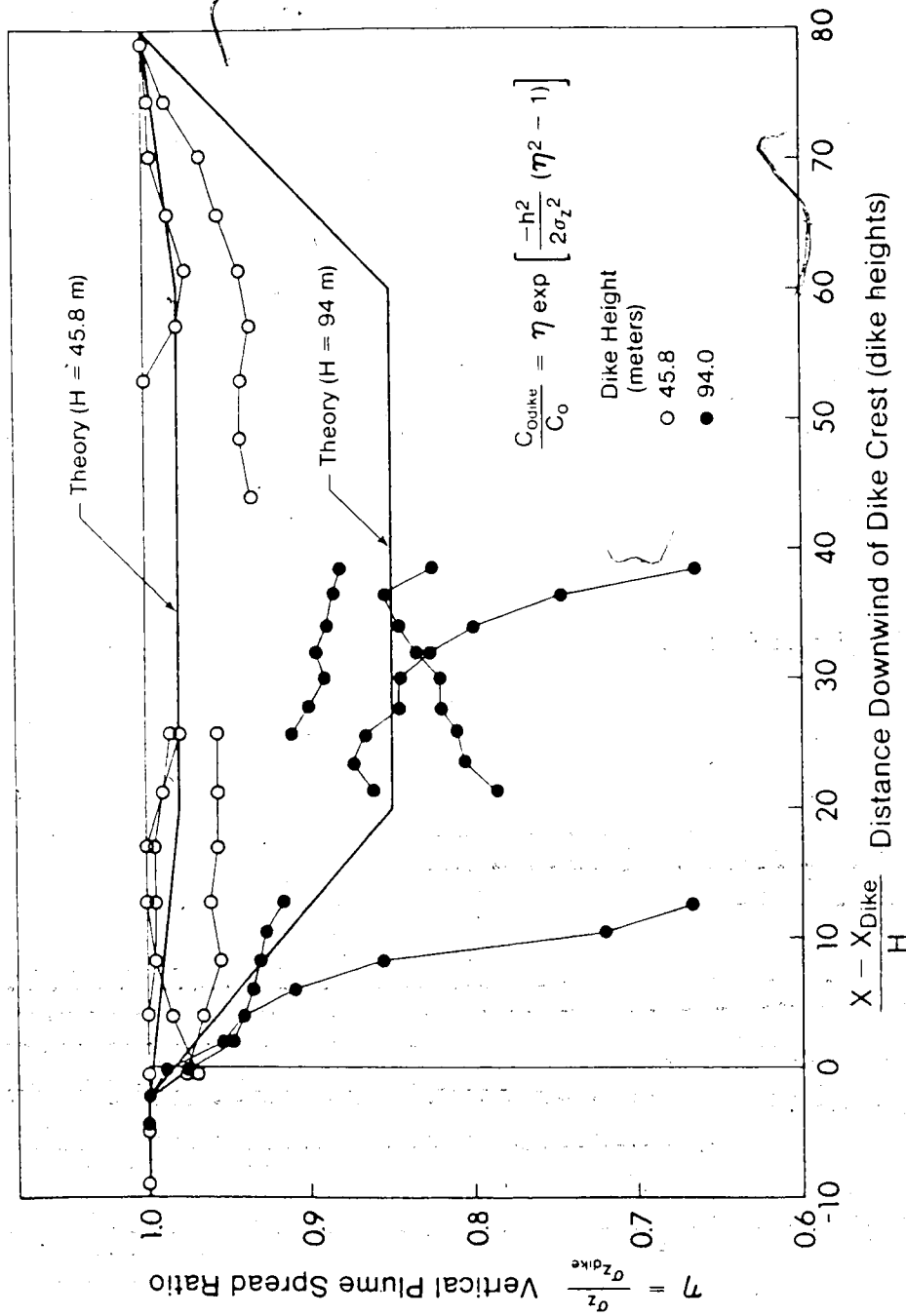
FIGURE 6-7: DIKE DISTURBANCE PARAMETER η FROM MEASURED GLC
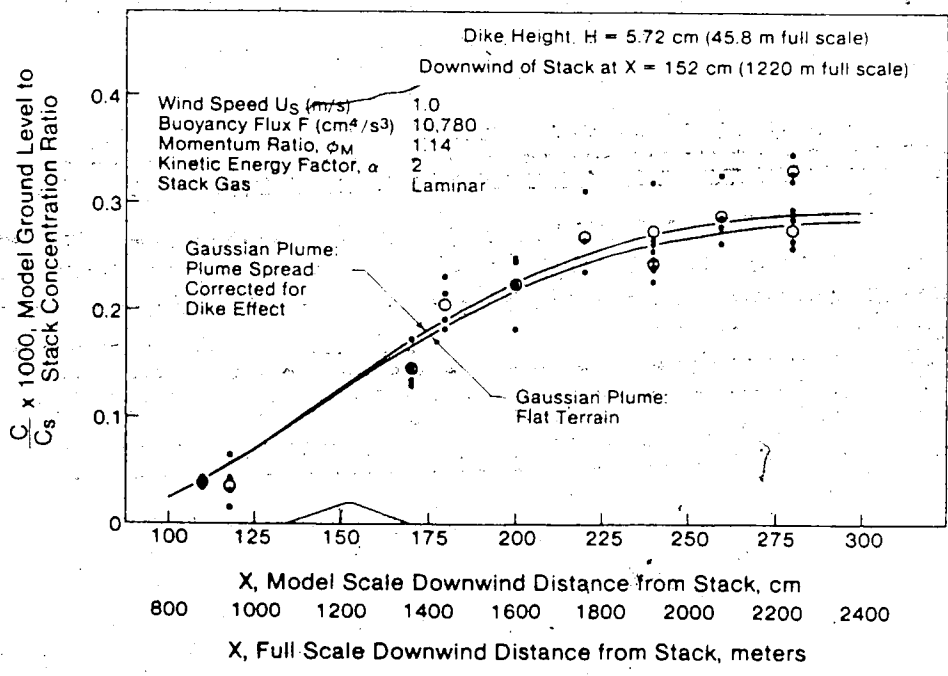FOR PLUME MODELS A AND B

Dike Height H = 5.72 cm (45.8 m full scale)
Upwind of Stack at X = -152 cm (-1220 m full scale)

Gaussian Plume:
Plume Spread
Corrected for
Dike Effect

Gaussian Plume:
Flat Terrain

Wind Speed U_S (m/s)   1.0
Buoyancy Flux F (cm⁴/s³) 10,780
Momentum Ratio, ϕ_M 1.14
Kinetic Energy Factor, α 2
Stack Gas   Laminar

X, Model Scale Downwind Distance from Stack, cm

X, Full Scale Downwind Distance from Stack, meters

Dike Height H = 5.72 cm (45.8 m full scale)
Downwind of Stack at X = 152 cm (1220 m full scale)

Wind Speed U_S (m/s)   1.0
Buoyancy Flux F (cm⁴/s³) 10,780
Momentum Ratio, ϕ_M 1.14
Kinetic Energy Factor, α 2
Stack Gas   Laminar

Gaussian Plume:
Plume Spread
Corrected for
Dike Effect

Gaussian Plume:
Flat Terrain

X, Model Scale Downwind Distance from Stack, cm

X, Full Scale Downwind Distance from Stack, meters

FIGURE 6-8:   PREDICTED AND MEASURED GLC FOR PLUME MODEL A AT
U_s = 1.0 m/s WITH THE MEDIUM DIKE UPWIND AND DOWNWIND

FIGURE 6-9: PREDICTED AND MEASURED GLC FOR PLUME MODEL A AT
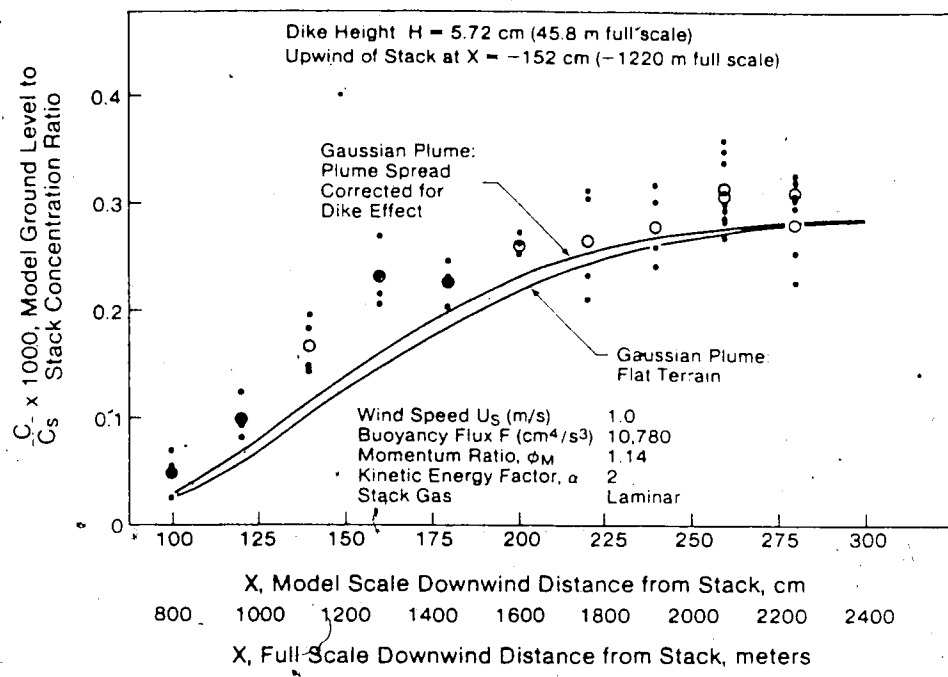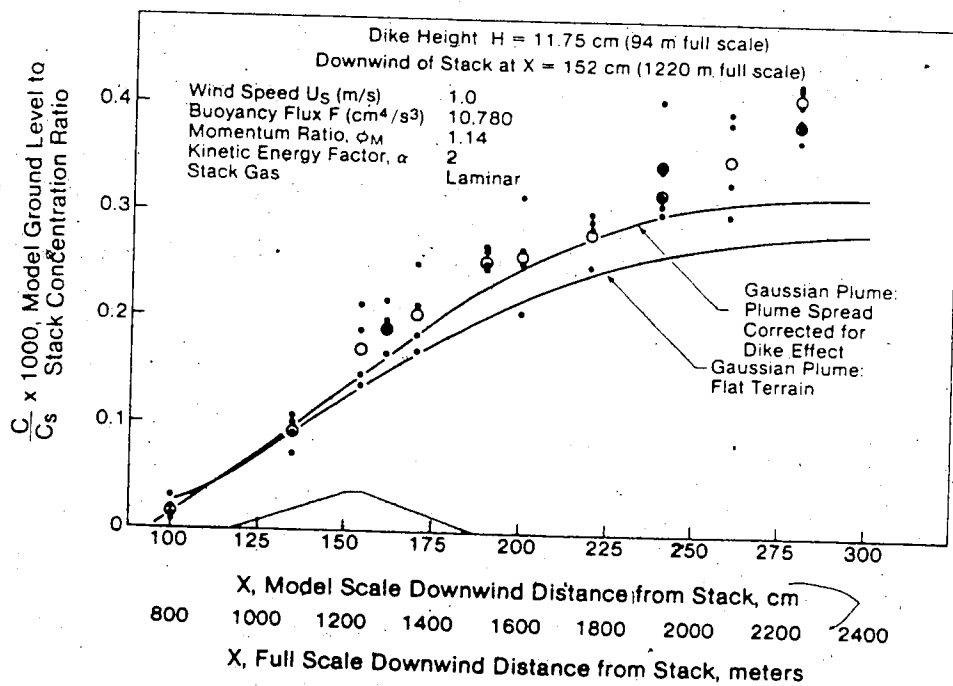$U_s \doteq 1.0$ m/s WITH THE LARGE DIKE UPWIND AND DOWNWIND

FIGURE 6-10: PREDICTED AND MEASURED GLC FOR PLUME MODEL A AT
U_s = 0.5 m/s WITH THE MEDIUM DIKE UPWIND AND DOWNWIND
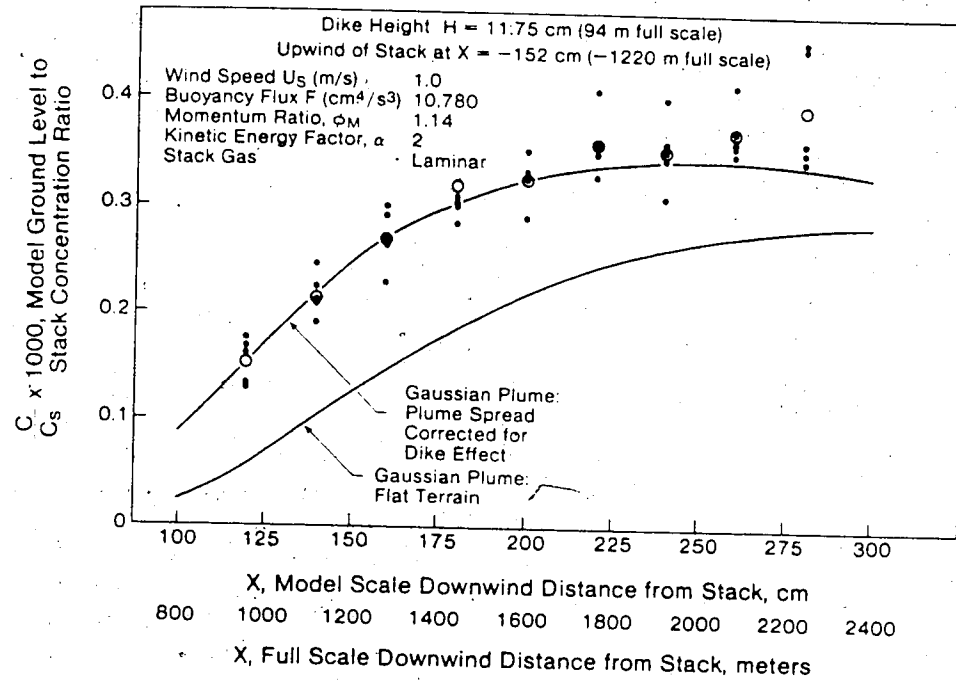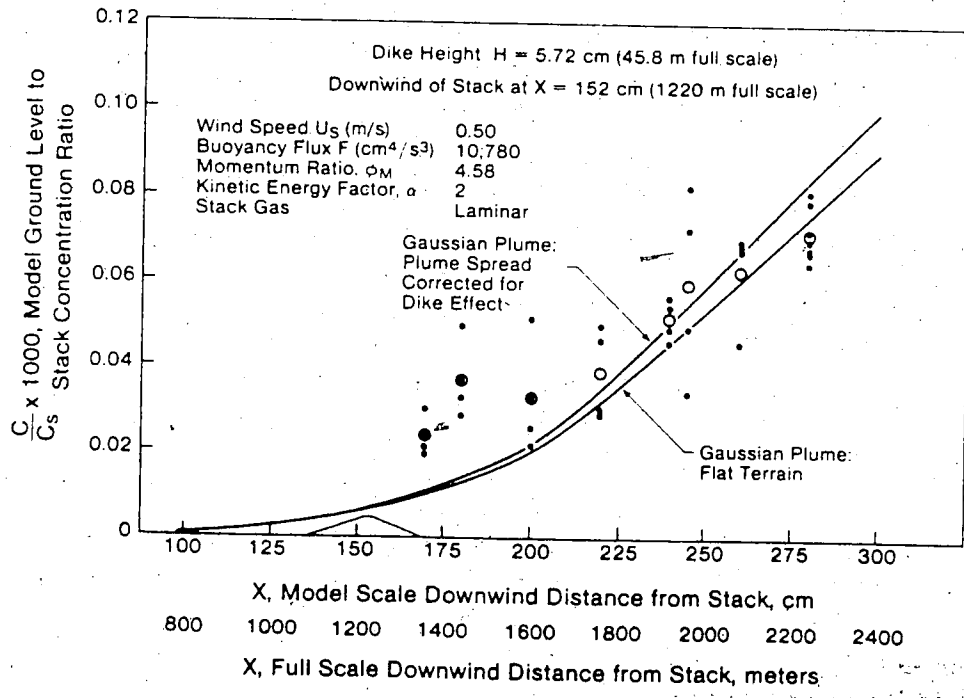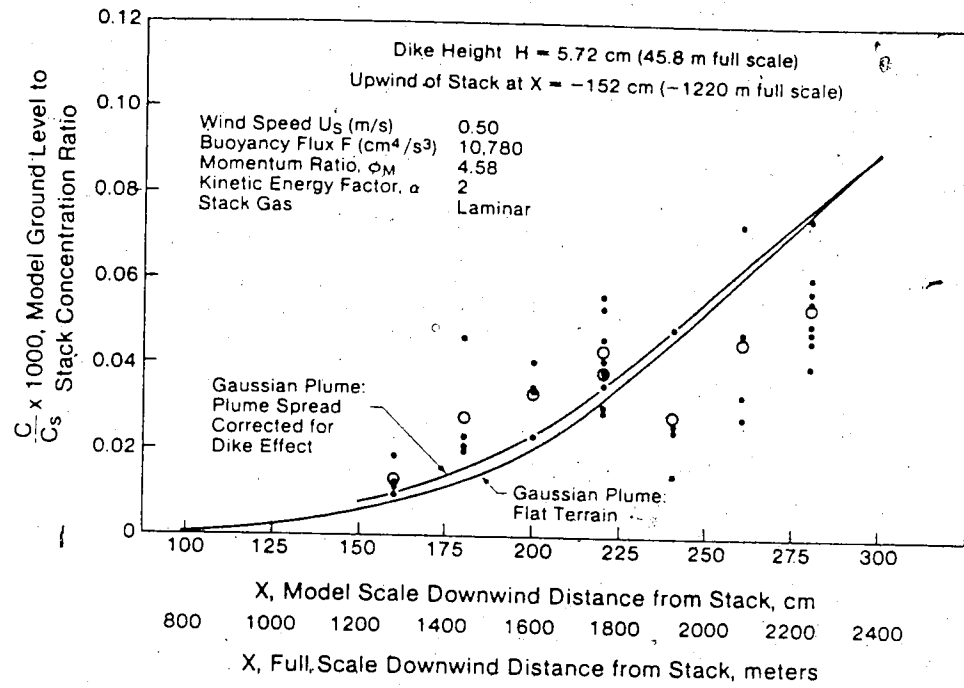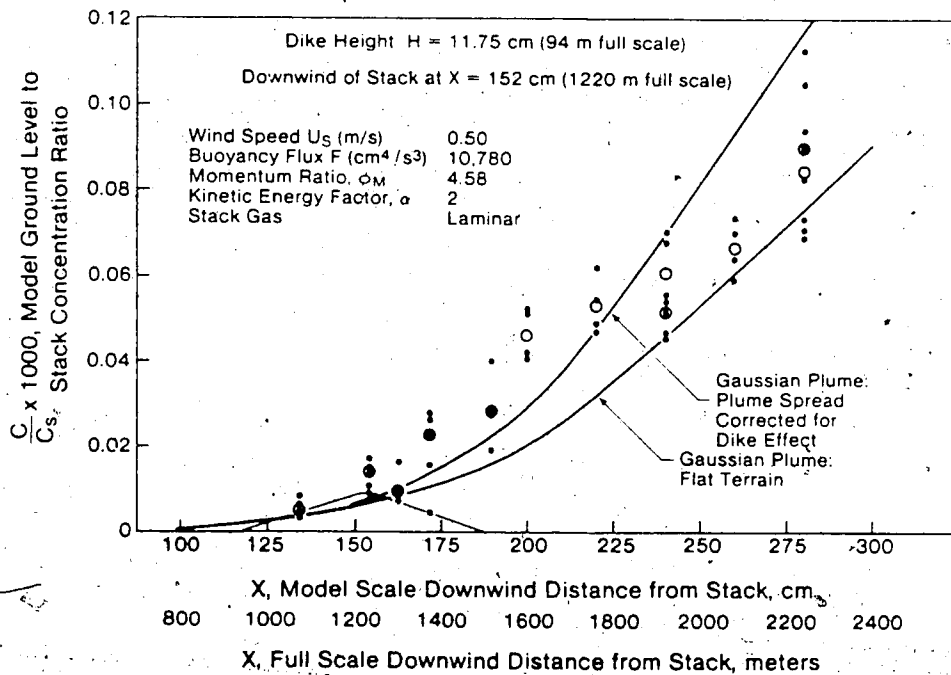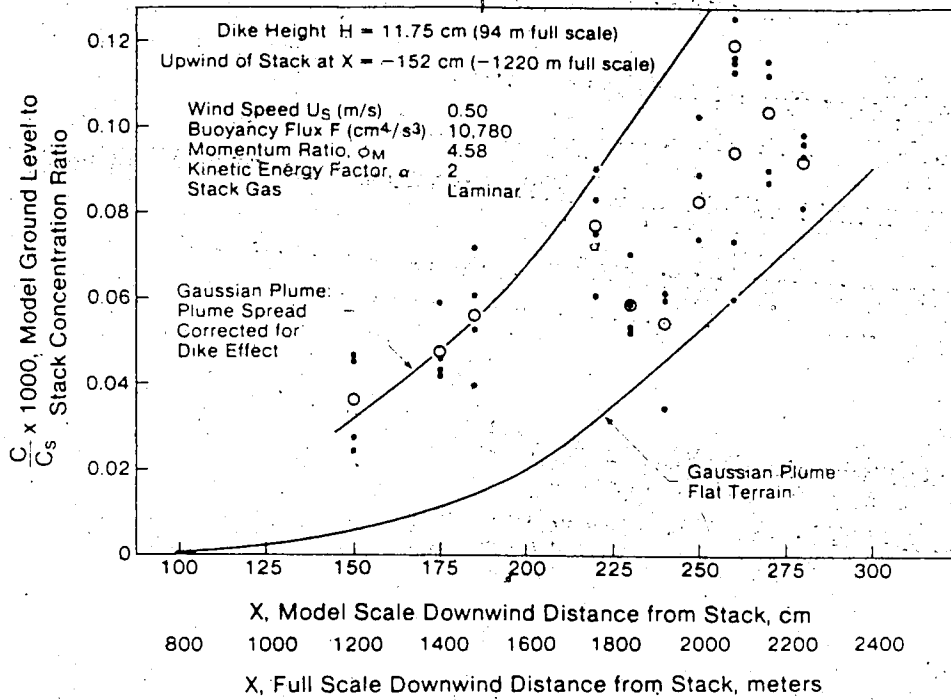
FIGURE 6-11:   PREDICTED AND MEASURED GLC FOR PLUME MODEL A AT
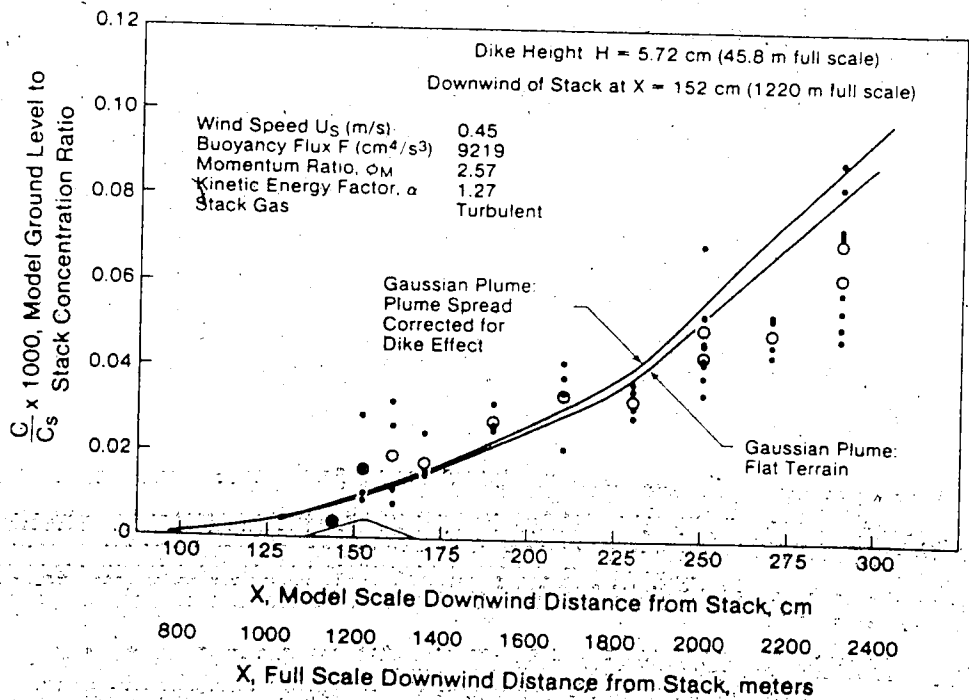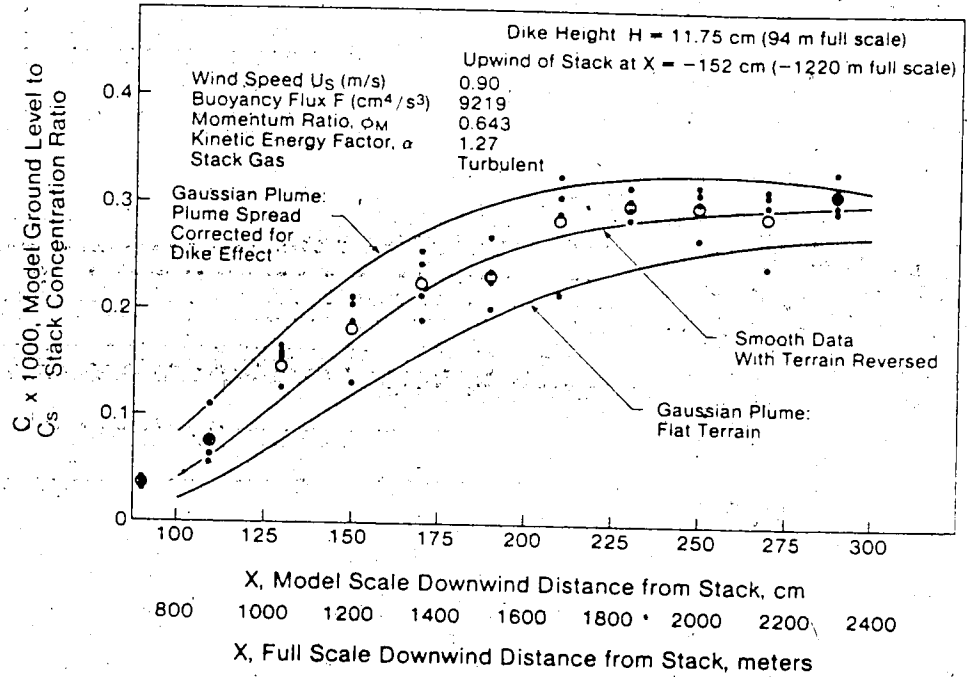 $U_s = 0.5$ m/s WITH THE LARGE DIKE UPWIND AND DOWNWIND

FIGURE 6-12: PREDICTED AND MEASURED GLC FOR PLUME MODEL B WITH DIKES UPWIND AND DOWNWIND

CHAPTER VII

SUMMARY AND RECOMMENDATIONS

A wind tunnel model was used to examine the behaviour of stack plumes on an oil sands surface-mining site. As a result of the current modelling practises, the mean flow Reynolds number in the wind tunnel was about 25,000 times smaller than that in the full scale atmospheric flow. This required a careful investigation of Reynolds number effect on several flow situations in the model before the model could be used with confidence. The results of these investigations are applicable to many physical modelling situations where Reynolds number mismatches occur.

Reynolds Number Effects on Cylinder Flows

The wakes behind the model stacks appear to exert realistic downeffects on the model plumes in spite of Reynolds number mismatch. This was due to the close similarity in cylinder base pressure coefficients at $-C_{Pb} \simeq 0.86$ between the model stack flows in the subcritical regime and the full scale stack flows in the transcritical regime. Great care must be taken in modelling of the stack wake effect, because if the full scale stack flows are in the supercritical regime, where base pressure coefficients $-C_{Pb}$ are much smaller, the model stacks will likely exaggerate stack downwash.

Plume Rise and Stack Downwash

A plume rise model for neutrally stable atmospheres, (4-11),

114

was developed and included the effects of both plume buoyancy and momentum. This model was found to compare very well with measured plume trajectories. It appears that momentum rise (the 1/3 law) and buoyancy rise (the 2/3 law) add as the sum of cubes. Therefore, either one is equally as useful a means of producing plume rise as the other. Also, for the majority of the plume trajectory, one type of rise is dominant, making it reasonable to consider momentum jet entrainment and buoyant plume entrainment as separate phenomena.

Values of the momentum rise entrainment constant β_1 to match measured plume rise were predictable from a simple semi-empirical model, (4-14). This model is recommended for use in general stack design calculations.

The buoyancy rise entrainment constant β_2 varied with atmospheric and stack flow conditions in agreement with physical arguments regarding entrainment. It was possible to identify constant β_2 values for various flow conditions, although the validity of such a procedure is somewhat questionable. Apparently, there is no universally applicable constant value of β_2, as suggested by Briggs (1975) ($\beta_2 = 0.6$). Developing a comprehensive model for β_2 to include all relevant entrainment effects is a topic for future study.

Plumes in turbulent cross-flows were observed to achieve final rise. The simple criteria, $x_{final} = 2200 \, L_B$, was found to predict this phenomenon for plumes under a wide variety of conditions. The constant of proportionality might have to be adjusted slightly for use with boundary layers other than the one tested.

The momentum flux ratio ϕ_M was found to be strongly correlated with the degree of severity of the stack downwash effect. To avoid

downwash, the designer should ensure that $\phi_M > 2$. At lower values, plume rise will be suppressed, but still predictable by (4-11) down to about $\phi_M = 1$, using adjusted β_2 values. Below $\phi_M = 1$, little or no plume rise is expected.

Reynolds Number Effects on Dike Flows

Flows past tailings pond dikes were found to be severely affected by the Reynolds number mismatch in the model. Model dikes had a greatly exaggerated wake size and influence on downwind flow turbulence. This type of modelling error is expected for all types of terrain features where separation points are not fixed by sharp edges. The use of a flow deflector vane mounted on the dike crest improved the model substantially, creating mean flow and turbulence profiles downwind of the dikes which were close to the expected full scale profiles.

Dike Effects on Ground Level Concentration (GLC)

The Gaussian model for plume dispersion was found to be adequate in fitting both measured plume concentration profiles and predicting GLC values. More complex dispersion models do not seem to be necessary, as the Gaussian model could predict all the important plume behaviour, such as ground reflection, and the shape of ground level concentration profiles.

The presence of dikes upwind and downwind of a stack was found to increase measured GLC values in general. This could be accounted for in the Gaussian model by the use of increased σ_z values. Increases in σ_z are not the only dike disturbance effect, but the fact that this was the one model, of the attempted corrections that gave reasonable results suggests that the dominant effect of dikes may be

on σ_z.

Dike effects on GLC were found to be very non-linear with dike height, as provided for by the dependence of η on H^3 in (6-10), and the non-linearity of the Gaussian model itself, in (6-8). Thus, large dikes produced disproportionately larger disturbances to GLC than smaller dikes.

The maximum value of GLC for a plume was found to be fairly insensitive to dike disturbances, even when large increases in GLC due to dikes were present prior to x_{max}. For dikes of about half the stack height in the present model, increases in $C_{O_{max}}$ were only about 20%. This means that predicting $C_{O_{max}}$ assuming flat terrain would in most cases be adequate for stack design.

Several specific recommendations are made from the results of the present study:

(1) In plume modelling, models should be as large as conveniently possible to minimize Reynolds number mismatch.

(2) When modelling stack downwash, smooth model stacks may probably be used if the full scale stack flows are transcritical. However, full-scale base pressure measurements on stacks would be very helpful in determining if the flows were correctly modelled, especially because of the stack end effect. Further investigation in this area is recommended.

(3) Stack designers should consider momentum as well as buoyancy as a means of producing plume rise, particularly because increasing ϕ_M will minimize stack downwash.

(4) When modelling flow over smooth terrain obstacles such as dikes, external flow modification is recommended as a means of avoiding the

unrealistically large recirculation zones that typically exist at low Reynolds number.

(5) The Gaussian plume model is recommended for use in predicting ground level concentrations from stacks. The far downstream variation in ground level concentrations should be investigated to determine if the Gaussian model will remain valid after a buoyant plume has achieved final rise.

REFERENCES

REFERENCES

Arie, M. and H. Rouse (1956), "Experiments on Two Dimensional Flow Over a Normal Wall", J. Fluid Mech. 1, part 2, pp 129-141.

Briggs, Gary A. (1969), Plume Rise, USAEC Critical Review Series, TID - 25075, Clearinghouse for Federal Scientific and Technical Information.

Briggs, Gary A. (1970), "Some Recent Analyses of Plume Rise Observations", Int. Air Poll. Conference, Wash. D.C., Dec. 1970.

Briggs, Gary A. (1972), "Discussion of Chimney Plumes in Neutral and Stable Surroundings", Atmos. Environ. 6, pp 507-510.

Briggs, Gary A. (1975), "Plume Rise Predictions", Environmental Research Laboratories, Air Resources, Atmospheric Turbulence and Diffusion Laboratory, Oak Ridge, Tennessee, June 1975, ATDL Contribution File No. 75/15.

Bringfelt, B. (1969), "A Study of Buoyant Chimney Plumes in Neutral and Stable Atmospheres", Atmos. Environ. 3, pp 609-623, plus author's reply to discussion of plume rise measurements at industrial chimneys, pp 317-319.

Bursnall, W.J. and L.K. Loftin (1951), "Experimental Investigation of Localized Regions of Laminar Boundary Layer Separation", Nat. Adv. Comm. Aero., Wash., Technical Note 2338.

Chang, S.C. (1966), "Velocity Distributions in the Separated Flow Behind a Wedge Shaped Model Hill", Colorado State University Fluid Dynamics and Diffusion Laboratory Technical Report CER 65SCC66.

Counihan, J. (1969), "An Improved Method of Simulating an Atmospheric Boundary Layer in a Wind Tunnel", Atmos. Environ. 3, pp 197-214.

Counihan, J. (1975), "Adiabatic Atmospheric Boundary Layers: A Review and Analysis of Data from the Period 1880-1972", Atmos. Environ. 9, pp 871-905.

Csanady, G.T. (1961), "Some Observations on Smoke Plumes", Int. Jour. Air Water Pollut. 4, pp 47-51.

Eliseev, V.S. (1973), "Stereophotogrammetric Investigation of the Air Flow in the Boundary Layer of the Atmosphere Above a Hill", from Berlyand, M. (ed.) Air Pollution and Atmospheric Diffusion, John Wiley & Sons, pp 95-108.

Fage, A. and V.M. Falkner (1931), "The Flow Around a Circular Cylinder", Aero. Res. Counc., London, Rep. and Mem. no. 1369.

Fay, J.A., Escudier, M. and D.P. Hoult (1969), "A Correlation of Field
    Observations of Plume Rise", Jour. Air Poll. Control Assn. 20,
    pp 391-397, 1970.

Flachsbart, O. (1929), from an article by H. Muttray, 1932, Handbook
    Experimental - Physik 4, part 2 (Leipzig), 316.

Good, M.C. and P.N. Joubert (1968), "The Form Drag of Two Dimensional
    Bluff Plates Immersed in Turbulent Boundary Layers", Jour.
    Fluid Mech. 31, part 3, pp 547-582.

Griffin, Owen M. (1977), "A Universal Strouhal Number for the 'locking-
    on' of Vortex Shedding to the Vibrations of Bluff Cylinders",
    Jour. Fluid Mech. 85, part 3, pp 591-606.

Hinze, J.O. (1975), Turbulence, 2nd Edition, McGraw Hill, p 643, p 729.

Isumov, N., Jandali, T., and A.G. Davenport (1976), "Model Studies
    and the Prediction of Full Scale Levels of Stack Gas Concentration",
    Jour. Air Poll. Control Assn 26, pp 956-964.

Ludwig, G.R. and G.T. Skinner (1976), "Wind Tunnel Modelling Study
    of the Dispersion of Sulphur Dioxide in Southern Allegheny
    County, Pennsylvania", U.S. EPA Report 903/9-75-019, pp 3-16.

Moussa, Z.M., Trischka, John W. and S. Eskinazi (1977), "The Near-
    Field in the Mixing of a Round Jet with a Cross-Stream",
    Jour. Fluid Mech. 80, part 1, pp 49-80.

Patrick, M.A. (1967), "Experimental Investigation of the Mixing and
    Penetration of a Round Turbulent Jet Injected Perpendicularly
    into a Transverse Stream", Trans. Inst. Chem. Engrs. (London)
    45, pp 16-31.

Plate, E.J. and C.M. Lin (1964), "The Velocity Field Downstream from
    a Two-Dimensional Model Hill", Part 1, Colorado State University,
    Fort Collins, Colo., Technical Report No. CER65EJP-CWL41.

Ricou, F.P. and D.B. Spalding (1961), "Measurements of Entrainments
    by Axisymmetrical Turbulent Jets", Jour. Fluid Mech. 11,
    pp 21-32.

Roshko, Anatol (1960), "Experiments on the Flow Past a Circular
    Cylinder at Very High Reynolds Number", Jour. Fluid Mech.
    10, pp 345-356.

Sachs, Peter (1972), Wind Forces in Engineering, 2nd Edition, Pergamon
    Press, 1978, p 70.

Singer, Irving A. and Maynard E. Smith (1966), "Atmospheric Dispersion
    at Brookhaven National Laboratory", Int. Jour. of Air and Water
    Pollution 10, Pergamon Press, pp 125-135.

Slawson, P.R. (1978), "Observations and Predictions of Natural
        Draft Cooling Tower Plumes at Paradise Stream Plant", Atmos.
        Environ. <u>12</u>, pp 1713-1724.

Taylor, G.I. (1945), "Dynamics of a Mass of Hot Gas Rising in the
        Air", USAEC Report MDDC-919 (LADC-276), Los Alamos Scientific
        Lab.

Weil, Jeffrey C. and Anders F. Jepsen (1977), "Evaluations of the
        Gaussian Plume Model at the Dickerson Power Plant", Atmos.
        Environ. <u>11</u>, pp 901-910.

Wilson, D.J. (1977), "Plume Diffusion over Downwind Two-Dimensional
        Hills: A Wind Tunnel Study", final report of Alberta Environ-
        ment Research Project #75-8, Department of Mechanical
        Engineering, University of Alberta, Edmonton, Alberta.

Wilson, D.J., Winkel, G., and O. Neiman (1979), "Reynolds Number
        Effects on Flow Recirculation Behind Two-Dimensional Obstacles
        in a Turbulent Boundary Layer", Proceedings of Fifth Interna-
        tional Wind Engineering Conference, July, 1979, Fort Collins,
        Colorado.

Winkel, Gordon (1979), M.Sc. Thesis, Department of Mechanical
        Engineering, University of Alberta, Edmonton, Alberta.

APPENDIX A

APPENDIX A

CORRECTION TO GLC MEASUREMENTS FOR MEAN
TUNNEL SPEED VARIATIONS

In the present study, the mean tunnel speed was found to vary

slowly around the desired constant value for a test by about $\pm 2\%$

(maximum) for successive 100 second averages. It was possible to correct

for this in the case of GLC measurements.

Ground level concentration readings are very sensitive to

changes in windspeed. This can be seen by examining the Gaussian model

for GLC

$$\frac{C_o}{C_s} = \frac{Q}{\pi U \sigma_y \sigma_z} \exp \left[\frac{-h^2}{2\sigma_z^2} \right] \qquad (6\text{-}3)$$

By the 2/3 law for buoyant plume rise, Δh is inversely proportional

to U. With this, (6-3) becomes

$$\frac{C_o}{C_s} \propto \frac{1}{U} \exp \left(-\frac{1}{U^2} \right)$$

This strong dependence of C_o on windspeed indicates the need to closely

control tunnel speed when taking GLC measurements. This led to the use

of the cloth filter stretched across the tunnel test section end for

plume model A measurements, as discussed in Chapter VI.

It is desirable to relate small changes in U to their resulting

effect on C_o. Defining a concentration parameter, $\psi = (\pi \sigma_y \sigma_z C_o)/(QC_s)$, (6-3) becomes

$$\psi = \frac{1}{U} \exp \left[-\frac{1}{2} \frac{h^2}{\sigma_z^2} \right] \qquad \text{(A-1)}$$

Taking the logarithm of (A-1),

$$\ln \psi = \ln \left(\frac{1}{U} \right) - \left[\frac{1}{2} \frac{h^2}{\sigma_z^2} \right] \qquad \text{(A-2)}$$

Using small disturbance theory, variations are assumed only in ψ and U. With $\Delta h \propto 1/U$, (A-2) is differentiated to obtain

$$\frac{d\psi}{\psi} = -\frac{dU}{U} \left[1 - \frac{(\Delta h)h}{\sigma_z^2} \right] \qquad \text{(A-3)}$$

Without the term involving Δh, (A-3) represents the relationship between ψ and U for a non-buoyant plume. For non-buoyant sources, the quantity CU/Q is preserved, and this differentiates to $d\psi/\psi = -dU/U$. The additional term, $(\Delta h)h/\sigma_z^2$, represents the modification to the non-buoyant relationship to account for plume rise.

Assuming the use of the Brookhaven C (neutral stability) power law equation for vertical spread, $\sigma_z \propto x^{0.78}$. Also, at a <u>fixed location</u>, $d\psi/\psi = dC_o/C_o$ and (A-3) may be rewritten as

$$\frac{dC_o}{C_o} = -\frac{dU}{U} \left[1 - \frac{K(\Delta h)h}{x^{1.56}} \right] \qquad \text{(A-4)}$$

where K is a dimensional constant. It was necessary to measure K

because the amount of variation measured in C_o and U were dependent

on the way measurements were taken, through sampling times used and

response characteristics of the equipment.

A study was undertaken using plume model A at $U_s = 0.5 \pm 0.1$ m/s.

Ground level concentration measurements were taken at a fixed location,

x = 260 cm, using 100 second samples. All procedures and equipment

were as described in Chapter II for GLC measurement.

A measurement of mean windspeed U_s was taken before and after

each 100 second sample using the Kurz Model 435 Anemometer with capa-

citor damped output (time constant $\tau = 100$ sec.). The average of these

two readings was used as an estimate of the average value of U_s

during each sample period. This is the same procedure used during all

GLC measurement in the present study.

From a large number of readings at x = 260 cm at windspeeds

between about $U_s = 0.4$ m/s and $U_s = 0.6$ m/s the constant K was ob-

tained as $K = 51 \text{ cm}^{-0.44}$. This value was used with (A-4) to correct

all GLC measurements in the present study. For example, for a GLC

sample nominally at $U_s = 0.5$ m/sec, the correction equation would be:

$$\frac{C_o(\text{measured}) - C_o(\text{standard})}{C_o(\text{standard})} = \frac{0.5 - U_s(\text{measured})}{0.5} \left[1 - \frac{K(\Delta h)h}{x^{1.56}} \right]$$

where C_o(standard), the corrected value of GLC, is the only unknown.

Plume rise values used in the calculation of K and in all

model A corrections were: for $U_s = 1$ m/s, $\Delta h = 2$ cm, and for $U_s = 0.5$ m/s,

as given below:

x(cm)	100	110	120	130	140	150	160	170	180 (and up)
Δh(cm)	9.9	10.4	11.0	11.6	12.1	12.5	12.9	13.4	13.6

When (A-4) was used to correct plume Model B data, $\Delta h = 0$ was used for $U_s = 0.9$ m/s and for $U_s = 0.45$ m/s, Δh was calculated using (4-11) and (4-15).

The magnitude of the GLC correction using (A-4) was typically less than 10% for $U_s = 0.45$ and 0.50 m/s, and typically less than 1% for $U_s = 0.90$ and 1.0 m/s.